Universität Rostock

Traditio et Innovatio

UNIVERSITY OF ROSTOCK

MASTER THESIS

Traffic flow as driven nonlinear dynamical system

Author:

BSc. Mārtiņš BRICS

Supervisor:

Priv.-Doz. Dr. Reinhard MAHNKE

Rostock, September 12, 2011

https://doi.org/10.18453/rosdok_id00000259

Adress: Universität Rostock
Institut für Physik
18051 Rostock
Tel: +49 381 498-6944
Fax: +49 381 498-6942
Website: http://www.physik.uni-rostock.de

Supervisor's E-Mail: reinhard.mahnke@uni-rostock.de
Author's E-Mail: martins.brics2@uni-rostock.de

Abstract

This thesis is about vehicular traffic flow in theory and experiment. Experimental part deals with data sets containing vehicular trajectories of a complex traffic situation. A lot of errors in empirical (experimental) data sets are corrected and data are analyzed and prepared for comparison with theoretical models. The data analysis shows the strong impact of lane changes and the strong dependence on the velocity difference to the car in front. Unfortunately data analyses also shows artificial structures within the data due to errors of NG-VIDEO software (errors of monitoring as well as smoothing position measurement data). This of course raise question about quality of data and do not allow to preform any noise analysis.

Partly based on empirical data analysis new modification of optimal velocity model (OVM) is proposed. The advantages of this model are explicit velocity dependence, smaller values for acceleration and deceleration, faster convergence to long-time solution and better match to fundamental diagrams from empirical data. However, comparison with field data from empirical data shows clear differences. The reason for that are both the model itself and the simplified traffic situation.

In this thesis also fluid dynamical model by Martin Hilliges and Wolfgang Weidlich is analyzed. The study is mainly focused on traffic jam formation and shape. Unfortunately as we are currently unable to calculate in reasonable time long-time solution, for cases when long time solution is wide traffic jam, no comparison to microscopic and empirical data is provided.

Contents

1. Introduction

In the 21^{st} century many branches of science merge together to investigate the common paradigm. The systems are so complex that only by applying tools from one field it is not longer possible to obtain useful results. Many years biologists, chemists and physicists tended to work separately but now-days it is quit common to work together in a same field as biophysics and system biology. Physics is the most fundamental science of all natural science that implies that theoretically it would be possible to describe correctly all systems only by applying fundamental principles of physics. But, there is a enormous limitation: such complex systems as biological organisms, atmosphere, many particle quantum systems includes a high number of freedom and in many cases solutions of regarding dynamical equations are highly instable. Therefore without knowing very precise initial conditions solutions does not make sense. Yes, but this is principal limitation, we simply cannot know them. An if we even theoretically speculate that it would be possible then it would not be possible to find numerical solutions due to limitations of computational techniques.

The possibility to investigate a highly complex system only from one science point of view is also restricted by requirement to know a lot of theoretical and empirical data. Only way how to tackle this problem is the collaboration of scientists from different scientific fields. The experimental chemists and biologists can work in laboratory and obtain highly valuable data. The computer scientists and physicists can build the models and verify them by comparing the experimental findings and simulation data. The same is true also for atmosphere dynamics, analytical and physical chemistry, etc.

If we look carefully there is something that goes through all these scientific fields, this is presences of many interacting particles. Therefore it causes the temptation to look whether it is possible to apply the concepts from classical many particle physics such different social systems and traffic movement on the roads. The first attempts to apply these principles in traffic systems goes deeply back in 20 century when in 1935 Greenshields [9] carried out early studies

of vehicular traffic, and in the 1950s, there was considerable publication activity in journals on operations research and engineering. Only 40 years later when the ratio of cars per capita was significantly increased the scientists started more systematic work towards traffic problems. Cities like Los Angeles and San Francisco suffer from heavy traffic congestion around the clock. In Germany alone, the financial damage from traffic due to accidents and environmental impact is estimated to be $100 billion each year. No-one anymore doubts that traffic problem should be tackled very seriously. There was some early pioneers like Whitman, Prigogine, Montroll, and Kühne, the primary research started in 1992 and 1993 with papers by Biham et.al. [5] (1992), Nagel and Schreckenberg [21] (1992), and Kerner and Konhäuser [17] (1993). These papers initiated an avalanche of publications in various international physics journals. Since then, it has been difficult to keep track of the scientific developments and literature and there are more than 100 different traffic models [11].

Without doubt, an efficient transportation system is essential for the functioning of modern societies. But the days when freeways were freeways are over. To concluding the understanding of underlying physical processes in traffic is not only important for logistic specialists and city developers but it has caused also interest from car manufacturer side because the capacity of expanding the market directly affects their income. So, better we will understand traffic phenomenon more effectively our societies will work. Additionally, it will also give some more fundamental understanding of many particle system that can be further applied to other important systems.

2. Empiric traffic data analysis

2.1. Introduction

Usually in physics to see how good is a theoretical model, predictions of such model have to be compared with experiments or observations as in astronomy. But what is an experiment in traffic physics? We have to take some cars with drivers (a lot of them), choose the segment of the road, instruct the drivers and then measure data what we want to see (from individual car trajectories and car parameters we should be able to calculate whatever we want). But there are almost no experiments in traffic physics (even if they are conducted, the experimental data are not openly accessible), because it is expensive and there are already a lot of cars on the streets whose data can be measured. In principle in traffic physics the situation is similar to astronomy, where all models have to be compared to observations.

The difference between traffic physics and astronomy is that the observations are usually not made by physicists (astronomers) but by traffic engineers and their main aim is not to check different models or provide qualitative data which are suitable for model analysis. Nowadays a lot of roads are monitored mainly with loop detectors and data about traffic flow is collected, but unfortunately usually only averaged information is stored. Averaged data of course are not really good for microscopic traffic models especially if our aim is to build a model with stochasticity, because only first moments of distributions can be effectively calculated. Fortunately traffic physicists realized this problem and to provide traffic physics with high-quality primary traffic and trajectory data in the early 2000's NGSIM program was created.

The Next Generation Simulation (NGSIM) program was initiated by the United States Department of Transportation (US DOT) Federal Highway Administration (FHWA) in the early 2000's. The program developed a core of open behavior algorithms in support of traffic simulation with a primary focus on microscopic modeling, and collected high-quality primary traffic and trajectory data intended to support the research and testing of the new algorithms. After end

of program, now (June 2011) on NGSIM homepage [1] there are 5 data sets available containing vehicle trajectories:

1. The Prototype Data Set
2. The I-80 Data Set
3. The US 101 Data Set
4. The Lankershim Data Set
5. The Peachtree Data Set.

Each data set contains 15 - 45 minutes of usable vehicle trajectory data recorded on $500\ \mathrm{m}$ - $600\ \mathrm{m}$ long road segment (prototype data set actually contains data from approximately $900\ \mathrm{m}$ long road segment, but quality of last $300\ \mathrm{m}$ is rather poor and is not recommended for data analysis). Prototype, I-80, US 101 data sets contains highway data and Lankershim and Peachtree data sets contains city road with traffic lights data. Vehicle trajectory data were transcribed from the video data using a customized software application, Next Generation Vehicle Interaction and Detection Environment for Operations (NG-VIDEO), developed for NGSIM and the videos were recorded by several cameras mounted on multistory building located near the observed road segment. Unfortunately as you will see in Sec. 2.4, these data sets contains a lot of errors and last changes in data sets where made in 2007. More over these changes resulted that now (at least until June 2011) for Prototype data set there is only $30\ \mathrm{min}$ and for US 101 data set there is only $15\ \mathrm{min}$ of trajectory data available instead of $45\ \mathrm{min}$ of data which was available before. From highway data sets only I-80 data set still contains $45\ \mathrm{min}$ as it should.

Prototype and I-80 data sets are from the same segment of Interstate 80 highway in Emeryville (San Francisco), California and we can call I-80 data set as improved version of Prototype data set (to reduce errors the section length was reduced from approximately $900\ \mathrm{m}$ to approximately $500\ \mathrm{m}$ and position were detected every $1/10\ \mathrm{s}$ instead of $1/15\ \mathrm{s}$). This unfortunately leads to fact that we loose off-ramp in I-80 data set (see Fig. 2.1). As US 101 data set contain only $15\ \mathrm{min}$ of trajectory data available and I-80 data set is an improved version of Prototype data set the main analysis of high way data will be focused on I-80 data (for better reasoning see Sec. 2.3).

2.2. I-80 Data Set

I-80 data set consists of 3 subsets (each approximately 15 minutes long) of data recorded on April 13, 2005 form 04:00 p.m. - 04:15 p.m., 05:00 p.m. - 05:15 p.m., 05:15 p.m. - 05:30 p.m. Lets call these subsets as D1, D2, D3. These data represent travel on the northbound direction of Interstate 80 in Emeryville, California. This data was collected using 7 video cameras mounted on a 30 – story building, Pacific Park Plaza (see Fig. 2.1). As we see form Fig. 2.1 study area consists of 6 lane highway with on-ramp (lane 7 in data).

Figure 2.1.: The aerial photograph of the I-80 study area in relation to the building from which the video cameras were mounted and the coverage area for each of the seven video cameras. The pictures taken from [2].

The data of each subset consists of recorded video, processed video (recognized cars are depicted with rectangles) and vehicle trajectory files. Vehicle trajectory data files have 18 columns and every row contains a single x, y, t data point for a vehicle (specified by vehicle identification number), with associated information.

Column 1 Vehicle identification number.

Column 2 Frame identification number.

Column 3 Total number of frames in which the vehicle appears in data set.

Column 4 Time elapsed time since Jan 1, 1970 in $\mathbf{ms}$ (milliseconds).

Column 5 x-coordinate of the front center of the vehicle with respect to the left-most edge of the section in the direction of travel in $\mathbf{feet}$.

Column 6 y-coordinate of the front center of the vehicle with respect to the entry edge of the section in the direction of travel in $\mathbf{feet}$.

Column 7 Global X Coordinate of the front center of the vehicle based on CA State Plane III in NAD83 in $\mathbf{feet}$.

Column 8 Global Y Coordinate of the front center of the vehicle based on CA State Plane III in NAD83 in $\mathbf{feet}$.

Column 9 Length of vehicle in $\mathbf{feet}$.

Column 10 Width of vehicle in $\mathbf{feet}$.

Column 11 Vehicle type: 1 - motorcycle, 2 - automobile, 3 - truck.

Column 12 Instantaneous velocity of vehicle in $\mathbf{feet/s}$.

Column 13 Instantaneous acceleration of vehicle in $\mathbf{feet/s^2}$.

Column 14 Current lane position of vehicle.

Column 15 Vehicle identification number of the lead vehicle in the same lane.

Column 16 Vehicle identification number of the vehicle following the subject vehicle in the same lane.

Column 17 Lead gap in $\mathbf{feet}$.

Column 18 Headway time in $\mathbf{s}$.

As we can see, data files contains some strange, not really useful informations like elapsed time since Jan 1, 1970 and global coordinates, but the good thing is that data files contain all necessary information for data analysis: x, y - coordinates of cars, vehicle identification number and length of vehicle. Unfortunately other useful data like velocity of cars and acceleration contains too big errors to be used directly (see Sec. 2.4).

2.3. Choice of data sets for further analysis

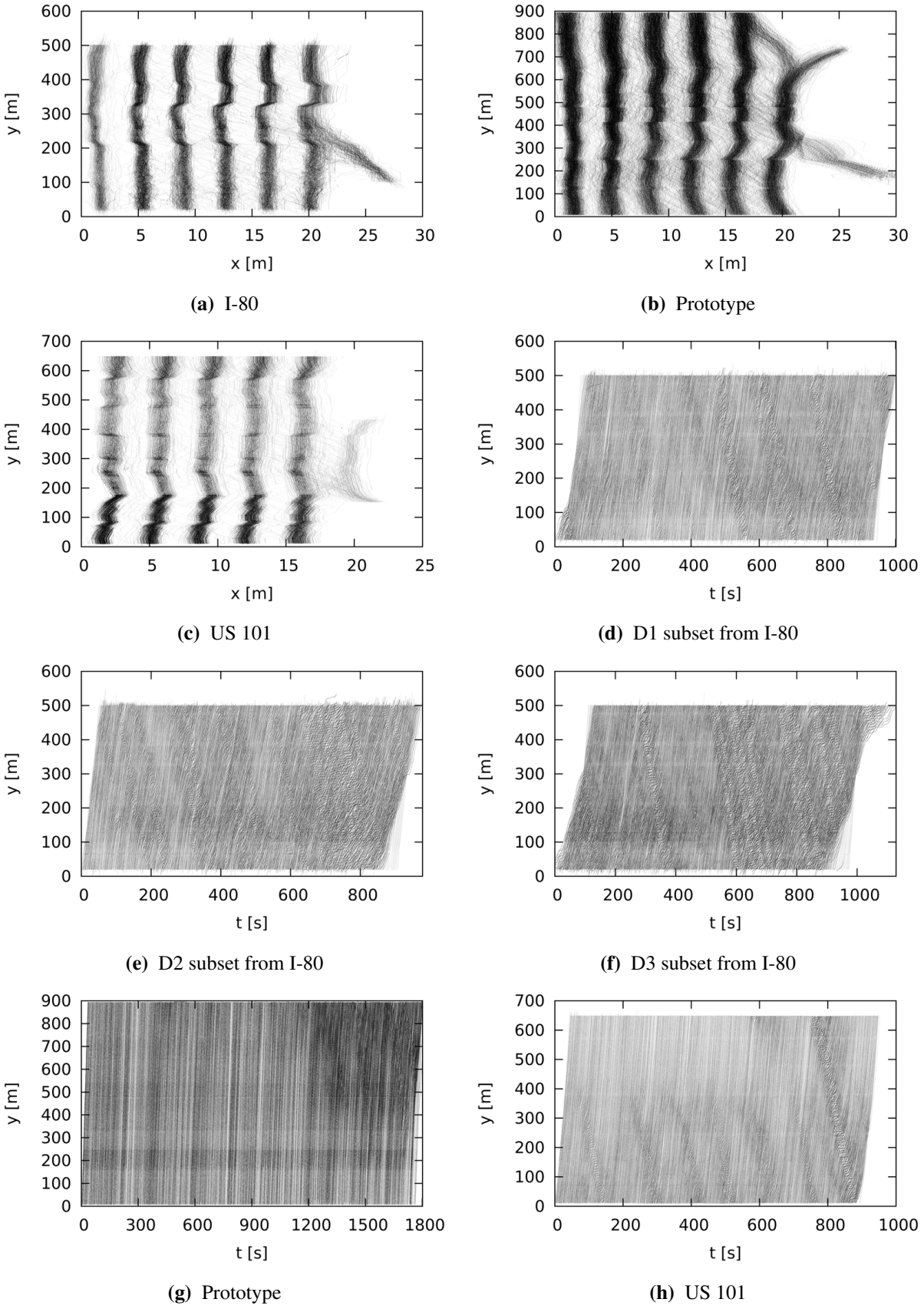

(a) I-80

(b) Prototype

(c) US 101

(d) D1 subset from I-80

(e) D2 subset from I-80

(f) D3 subset from I-80

(g) Prototype

(h) US 101

Figure 2.2.: Trajectories and space-time plots for all highway data sets.

Before we do further data analysis it is necessary to study properties of traffic flows in data sets to see whether same data sets have better data for analysis and whether it is worth the effort to analyze all data sets. This is quite important, because data sets which has only free flow are not very interesting for analysis, because all vehicles drives with almost the same speed.

Quite a lot of information about traffic flow and data quality can be found from car trajectory plots (y-coordinate vs x-coordinate) and from space-time plots (y-coordinate vs time) for all vehicles in data sets. These plots for all highway data sets can be found in Fig. 2.2. Dark lines in in trajectory plots (see Figs. 2.2a - 2.2c) represents lanes. So from trajectory plots we can see that I-80 data set has 6 lanes and on-ramp, Prototype data set has 6 lanes, on-ramp and off-ramp, US 101 data set has 5 lanes, on-ramp and off-ramp. The reason that these dark lines in trajectory plots are not straight lines, but zigzag are artifacts (errors) of NG-VIDEO software (not correctly adjusted x-coordinate wen changing between cameras). These artifacts are not so bad, because x-coordinate is only used for lane detection and they actually allows us to see camera ranges. The light lines between dark lines shows lane changes or are just errors of determination of x-coordinate. To determine which of these reason is mainly responsible for these lines we can look to trajectories of cars which did not change lines (see Figs. 2.3 and 2.4).

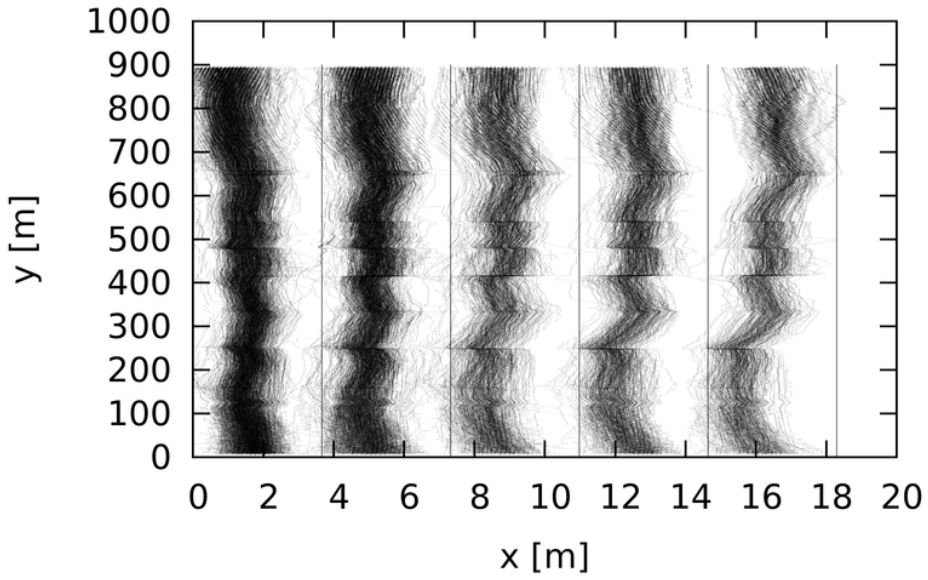

Figure 2.3.: Trajectories of cars from Prototype data set, without lane changes. Solid straight vertical lines represent lane ranges.

From trajectories of cars which did not change lanes we see, that unfortunately for Prototype data set a lot of these lines are errors of determination of x-coordinate, but for I-80 and US

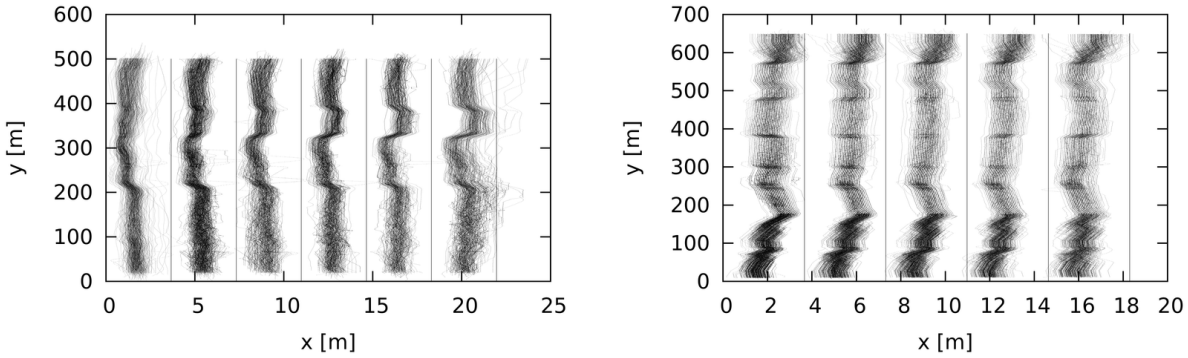

Figure 2.4.: Trajectories of cars from I-80 and US 101 data set, which did not change lanes. Left figure is from I-80 data set for which lane changing errors are already corrected (see Sec. 2.4.2) and right figure is from US 101 data set. Solid straight vertical lines represent lane ranges.

101 data sets we see that these really are mainly lane changes. Thus we have to conclude that Prototype data set has a lot more and larger errors for determination of x-coordinate, which unfortunately suggest that Prototype data set has also larger errors for y-coordinate.

The intensity of the dark lines is proportional to the number of cars in particular segment of the lane. For Prototype and I-80 data sets we see, that dark lines for all lanes except first one (for lane numbers see Fig. 2.1, where lanes are numbered from left to right) has almost the same intensity. This suggest that first lane may be high-speed lane (cars on this lane drive with larger velocities than on other lanes) and have other properties than other lanes, but to be sure it is necessary to look at flux and density plots of first lane. All lanes from US 101 data set has similar intensity, so it seems that there is no high-speed lane, but we see that for first $200\ \mathrm{m}$ dark lines are more darker which indicates, that vehicles in this section drive with much smaller speed than in the rest region. This indicates for different speed limits. Clearly there is not high-velocity lane in US 101 data set, because high-speed lane can not exist if there are low and changing speed limits.

From space-time plots (see Figs. 2.2d - 2.2h) we can see whether we have free or congested traffic flow. If we have a congestion then as velocity in congested flow is smaller than in free flow, in congested region slope for this trajectory is smaller. So congestions in space-time plots are regions with smaller slope and as congestions runs backwards, these regions have negative slope. These congestions one can see much better if we plot space-time plots for singe lanes, for example see Fig. 2.5f. From Fig. 2.2 we see that all subsets of I-80 and US 101 data set contains congested traffic and only Prototype data set has free traffic flow. It is useful if data set has congestions to plot space-time plots for every lane separately. We present these plots

in Fig. 2.5 and also in Figs. A.4 and A.5 in Appendix. From space-time plots for individual lanes we see that for all subsets of I-80 data set flow in lane 1 is always free even when there are congestions on all other lanes. This confirms that lane 1 has different traffic properties than other lanes and most likely is high-speed lane. Lane 2 and 4 has slightly more congestions than other lanes, and we see congestions in all other lanes except first one in all subsets of I-80 data set. We also see that in subset D3 traffic is more congested than in D2 and in D2 is more congested than in D1. In US 101 data set situation is quite opposite: lane one has a lot of congestions, but other lanes has only one congestion.

One bad thing what we recognize in all space-time plots are brighter horizontal lines at camera positions. This indicates that mostly at positions of camera changing vehicles drive faster. This, of course, can not be in reality and again must be an artifact of NG-VIDEO software. So we have to conclude that on camera changes not only x-coordinate has larger errors but also y-coordinate has larger errors. The reason for this can be found in forums of NGSIM projects [1] and is that cameras actually do not over lap and even more there are gaps between cameras, so that for some time (approximately 0.3 s) position of car is not recoded with either of cameras and trajectories at these point are just extrapolated.

From this short analysis it was decided to exclude Prototype data set from further analysis, because it contains only free flow data with larger errors for x-coordinate and y-coordinate than I-80 data and I-80 data set already contains enough free flow data. As US 101 data set contains data from other region and have different and changing speed limits, it is not good choice to analyze these data together as one big data set. And as we have only 15 minutes of data and we have mainly free flow traffic flow in all lanes except lane 1 it does not seems to be worth of effort to analyze also US 101 data set. So for further analysis only I-80 data set was chosen, which means that in further analysis data set with 5678 vehicles will be used. Number of vehicles and types in each subset can be found in Tabs. 2.1, 2.2 and 2.3.

Table 2.1.: Vehicles types in D1 subset of I-80 data set.

vehicle type	**number of vehicle**	**percentage**
motorcycle	14	0,68%
automobile	1942	94,64%
truck	96	4,68%
total	**2052**	**100,00%**

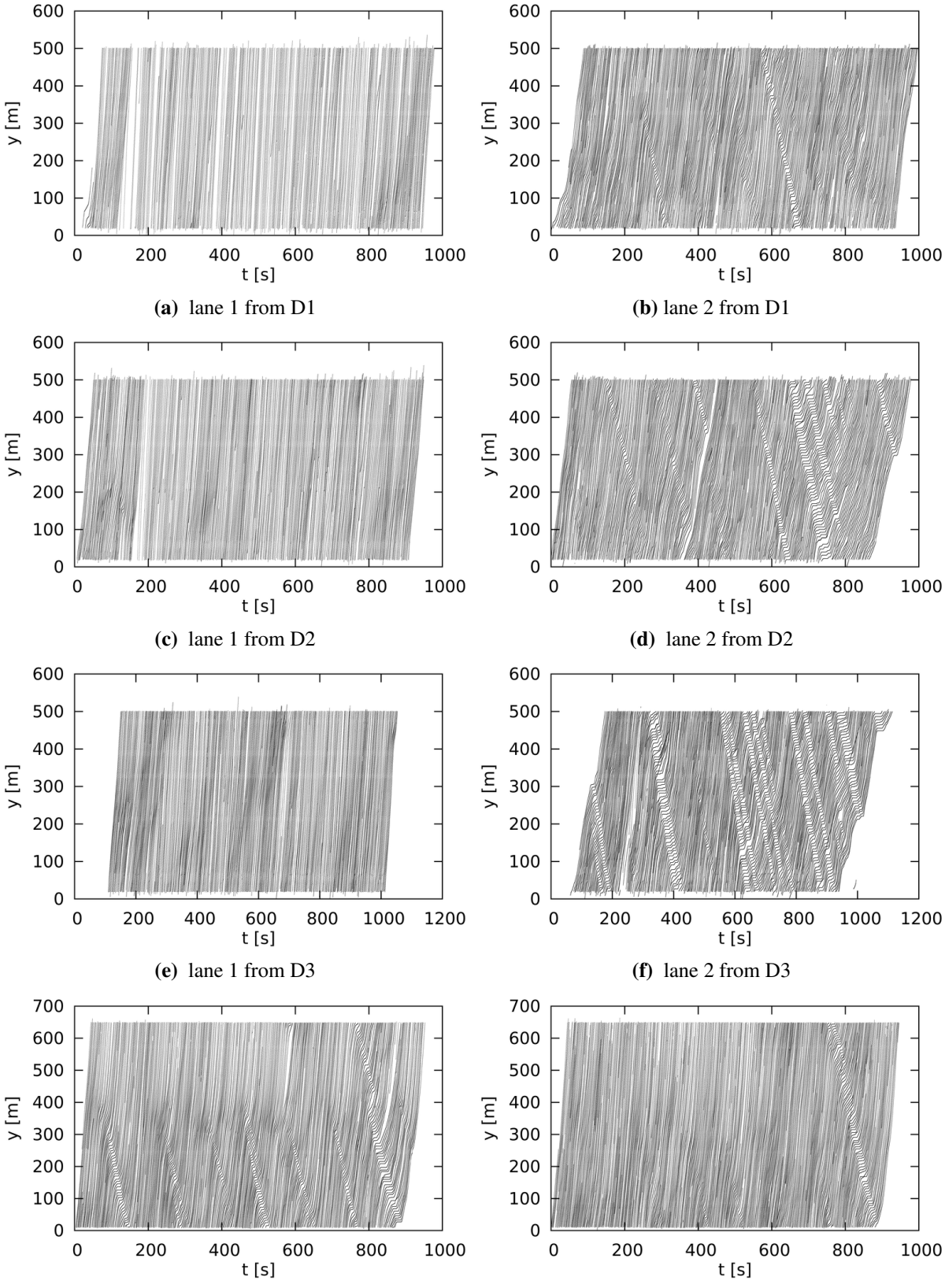

(a) lane 1 from D1

(b) lane 2 from D1

(c) lane 1 from D2

(d) lane 2 from D2

(e) lane 1 from D3

(f) lane 2 from D3

(g) lane 1 from US 101

(h) lane 2 from US 101

Figure 2.5.: Comparison of space-time plots between lanes 1 and 2 from subsets D1, D2, D3 of data set I-80 and data set US 101.

Table 2.2.: Vehicles types in D2 subset of I-80 data set.

vehicle type	number of vehicle	percentage
motorcycle	24	1,31%
automobile	1742	94,88%
truck	70	3,81%
total	**1836**	**100,00%**

Table 2.3.: Vehicles types in D3 subset of I-80 data set.

vehicle type	number of vehicle	percentage
motorcycle	17	0,95%
automobile	1724	96,31%
truck	49	2,74%
total	**1790**	**100,00%**

2.4. Errors

As mentioned before all NGSIM data sets contains errors and of course before any data analysis can be performed one have to try to correct all errors that are possible to correct. These errors we can find if we simply look at vehicle trajectory data files and processed video files. In trajectory data files we can see that acceleration values have surrealistically large values for acceleration (see figures 2.9a and 2.9b). As acceleration is computed from velocity data, also values for velocities have to be recomputed. By looking at processed videos we can see that sometime instead vehicle the shadow of the same vehicle or other vehicle is recognized (see Fig. 2.6) instead. If shadow of the same vehicle is recognized as the vehicle this will result in errors for x-coordinate and thus there will be errors for lane number, following and preceding vehicle numbers and lead gap and headway. If shadow of the other vehicle is recognized as the vehicle then this will result in errors for y-coordinate thus there will be errors for velocity, acceleration and lead gap and time headway. Unfortunately we can try to correct errors only if shadow of the same vehicle is recognized as the vehicle (lane changing errors), because y-coordinate is already smoothed and we do not see these errors in vehicle trajectory data files.

Correctable errors we can divide in two groups: lane changing errors, which appears from errors for x-coordinate and errors of velocity and acceleration, which appears, because of ignorance of noise in calculation of velocity and acceleration. As for velocity and acceleration calculation only y-coordinate is used, in principle these these error can be corrected in any oder,

Figure 2.6.: Video post-processing software NG-VIDEO errors for vehicle 1455 from subset D1. In left figure we can see that instead of vehicle 1455 its shadow is detected. In right figure we see another kind of errors, that instead vehicle 1456 vehicle's shadow 1455 is detected (vehicle 1455 is track on lane 2 and vehicle 1456 is truck at lane 3).

but as Savitzky-Golay filter [25] is also applied to x-coordinate, the velocity and acceleration errors are corrected first.

2.4.1. Errors for velocity and acceleration

If we look at acceleration data found in I-80 data sets we see that vehicles accelerate and decelerate very much even when in video there is no reason for such behavior. And if we plot probability distribution for acceleration (see Fig. 2.7), we see that that this distribution has 3 maximums: around $a = 0\ \mathrm{m/s^2}$ and $a \approx \pm 3.3\ \mathrm{m/s^2}$ ($10\ \mathrm{feet/s^2}$). If we analyze data files we can find that the peaks for acceleration around $\pm 10\ \mathrm{feet/s^2}$ appears from the way of calculation of acceleration. One can find that acceleration (negative value represents declaration) is calculated

$$a_i = \begin{cases} \mathrm{sgn}\left(v_i - v_{i-1}\right) \cdot \min\left(fps \cdot |v_i - v_{i-1}|, 10\right)\ [\mathrm{feet/s^2}] & \text{if } i > 2 \\ 0\ [\mathrm{feet/s^2}] & \text{else} \end{cases}, \tag{2.1}$$

where sgn is signum (sign) function, i is number of the frame, fps are frames per second, v_i is velocity value in this frame and v_{i-1} is velocity value in previous frame. This provides, that we do not get values for acceleration bigger than technically possible, however, probability

distribution is completely unrealistic. Moreover if we investigate accelerations for single car (see Figs. 2.9a and 2.9b), we see that in this way calculated acceleration is actually mainly the amplified noise from errors of position data. It is clear that if we want to improve our data for acceleration we have to apply some kind of filter. As we are interested in improvement of acceleration, which is second derivative of y-coordinate, to reduce noise Savitzky-Golay filter [25] was chosen, because it allows just by smoothing function calculate directly also derivatives of this function.

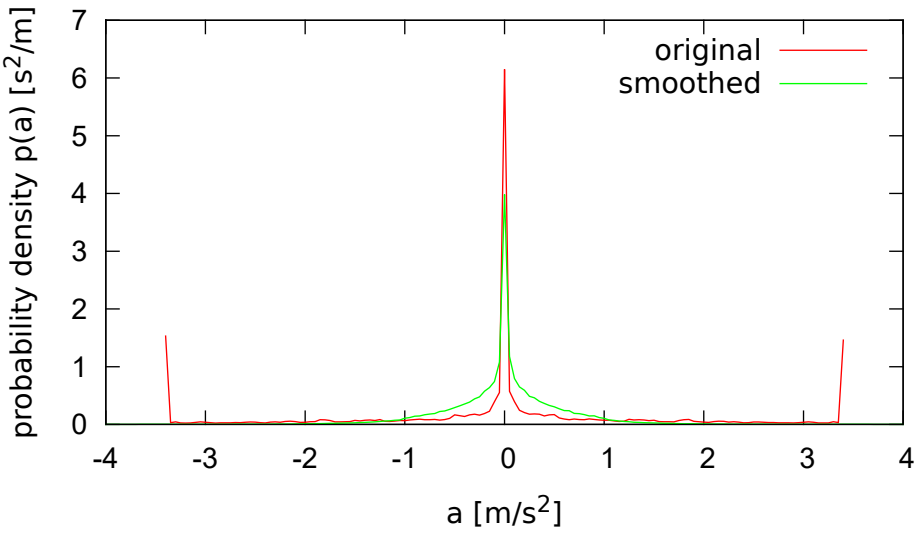

Figure 2.7.: Probability distribution of acceleration from I-80 data sets. Original (red) means unmodified data from I-80 data set files, smoothed (green) means calculated data after applying Savitzky-Golay filter to y-coordinate for data in I-80 data set.

Savitzky-Golay filter tries to fit a set of data points to a polynomial in the least-squares sense and as result new value g_i of point i with old value f_i is calculated using n_r points which are to the right to point i and using n_l points to the left of point i

$$g_i = \sum_{j=-n_r}^{n_l} c_j \cdot f_{i+j} \ , \tag{2.2}$$

where c_j are coefficients which can be found from least square interpolation and have property

$$\sum_{j=-n_r}^{n_l} c_j = 1 \ . \tag{2.3}$$

If data are fitted with polynomial with order at least 2 we can also simply calculate first and

second derivatives of function i.e. velocity and acceleration

$$v_i = fps \cdot \sum_{j=-n_r}^{n_l} \tilde{c}_j \cdot f_{i+j} \ , \ a_i = fps^2 \cdot \sum_{j=-n_r}^{n_l} \bar{c}_j \cdot f_{i+j} \ , \tag{2.4}$$

where $fps = 1/\Delta t$ means frames per second used for position detection or reciprocal of time interval between 2 following data points.

For data smoothing polynomial of order 2 and $n_r = n_l = 7$ was chosen. This unfortunately leads, that we can not calculate position, velocity, acceleration at 7 points from beginning and end. For those points we can calculate results with maximally large value of $n_r = n_l$, so for example for fifth point from beginning and end we can use $n_r = n_l = 4$. Using this approach of course noise for these points is not so good filtered and if we look to the results for acceleration of applying Savitzky-Golay filter (see Figs. 2.9a and 2.9b) for most vehicles at those points we have larger oscillations for velocity values than in other points. So for most cars it gives no sense to uses these points at all for further data analysis.

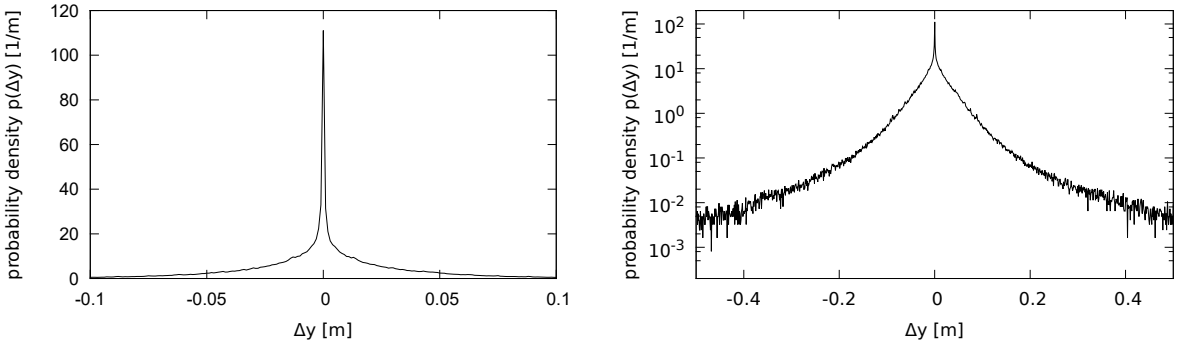

Figure 2.8.: Probability distribution for change of y-coordinate by applying Savitzky-Golay filter (absolute value of difference between old and new value) to data from I-80 data set. Left figure is in linear scale and right figure in in logarithmic scale.

The results for applying Savitzky-Golay filter to data in I-80 data set can be seen in Figs. 2.7, 2.8 and 2.9. As we can from Fig. 2.7, that by applying Savitzky-Golay filter we have a lot more realistic probability distribution for acceleration and also we can see from Fig. 2.9 have smaller and more realistic values of acceleration except first and last 7 points. Also values for velocity are a lot improved. As you can see from Fig. 2.8, this improvement was achieved only by slightly modifying original data, the changes for y-coordinate were usually smaller than $1 \ \mathrm{cm}$ which is much smaller than error for y-coordinate of vehicle. So we can conclude that it is recommendable to use Savitzky-Golay filter for y-coordinate. Improvements from applying

Savitzky-Golay filter for x-coordinate are not so obvious: some lane changing errors may be corrected (see Sec. 2.4.2) and it forces to recalculate lane numbers for vehicles, but as lane numbers are already recalculated, it is used also in further data analysis.

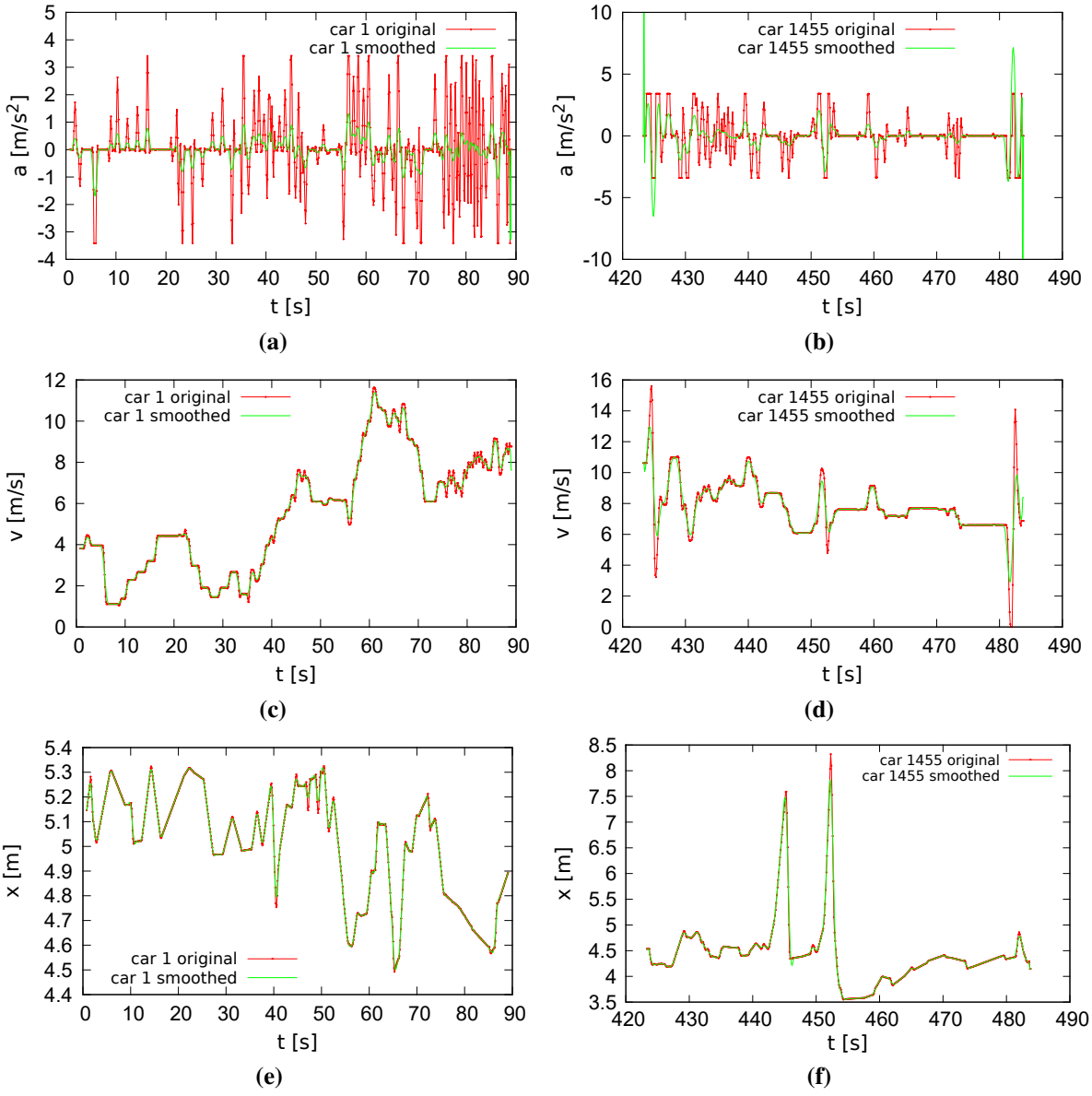

Figure 2.9.: Results for acceleration (Figs. (a)–(b)), velocity (Figs. (c)–(d)), x-coordinate (Figs. (e)–(f)) of applying Savitzky-Golay filter to vehicles with number 1 and 1455 form D1 subset of I-80 data set. Original (red) means unmodified data from I-80 data set data files, smoothed (green) means calculated data after applying Savitzky-Golay filter to y-coordinate and x-coordinate for data in I-80 data set.

2.4.2. Lane changing errors

If we plot trajectories for cars from subset D1 of I-80 data set, which change lanes more than four times (see Fig. 2.10) we notice, that some vehicles (365, 447, 518, 1455, 1628, 2087, 2767) make some fast double lane changes (change from initial lane to another lane and after small time change back to initial lane), and vehicle number 1455 at about $y = 300$ m makes slow double lane change, but it really never comes close to middle of lane 1. Looking at video

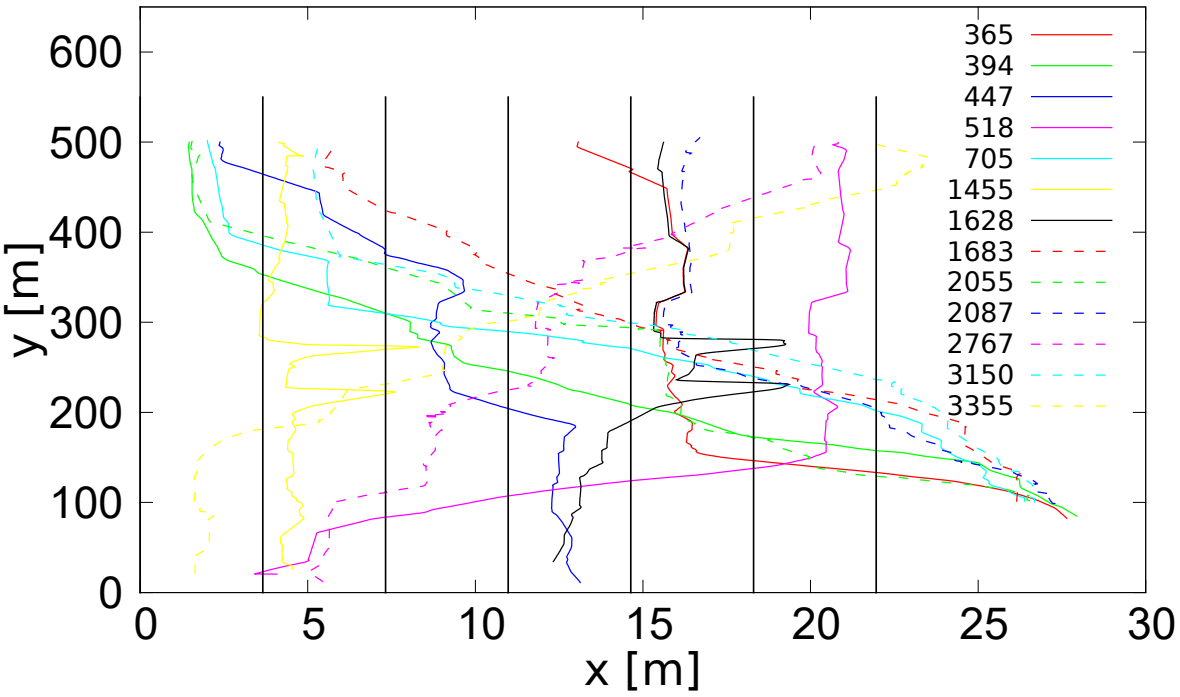

Figure 2.10.: Trajectories of cars which change lanes more than 4 times from subset D1 of data set I-80. Solid straight vertical lines represent lane ranges.

data we can see, that none of two scenarios actually happens and these are errors of video post-processing software NG-VIDEO. Usually these errors are near video camera range borders when instead of vehicle, vehicles shadow is detected (see figure 2.6). From video analysis one finds out that actually only 6 of 13 vehicles mentioned in Fig. 2.10 makes more than 4 lane changes.

The good thing is that those kind of lane changing errors are quite simple to correct, but the problem is that original lane change algorithm is unknown. The best option in this case is to correct errors using x-coordinate and y-coordinate data only. Based on road segment topography and on trajectory data analysis lane changing algorithm which can be found in listing 2.1 was created. In this algorithm variable $lane\_nr$ represents lane number arrays x and y contains x-coordinate and y-coordinate in meters. Note that there is no need to multiply with

a if coordinates of vehicle position are stored in feet. Lane number value 7 represents on ramp and -6 represents that car is on wide part of lane 6 where it is possible, that 2 cars on lane 6 may have the same y-coordinate and one car can overtake other car. This is important if we want correctly determine lead and lag gaps. To reduce number of points where $lane\_nr = -6$, we can replace $lane\_nr = -6$ with $lane\_nr = 6$ if at previous time moment $lane\_nr = 6$.

Listing 2.1: Lane change algorithm

```
double a=0.305;
if(x[i]<=12*a){
  lane_nr=1;
  }
  else if(x[i]<=24*a){
    lane_nr=2;
  }
  else if(x[i]<=36*a){
    lane_nr=3;
  }
  else if(x[i]<=48*a){
      lane_nr=4;
  }
  else if(x[i]<=60*a){
    lane_nr=5;
  }
  else if(x[i]<=75*a){
    if(y[i]<(666)*a&&y[i]>(666-170)*a&&x[i]>=72.5*a){
      lane_nr=7;
    }
    else{
      lane_nr=6;
    }
  }
  else{
    if(y[i]<666*a){
      lane_nr=7;
    }
    else{
      lane_nr=-6;
    }
```

To remove those 2 types of lane errors described before it is necessary to search for double lane changes. Then if time of double line change is smaller than 1.5 s or difference between average position (x-coordinate) on initial lane and lane where car changed is smaller than half lane width and it is not motorcycle we assume, that there were no lane changes and correct lane number. Note that main part of still remaining double lane changes are changes from lane 6 to 7, what

is not allowed (crossing of continuous white line), but video analysis confirms, that there are such aggressive drivers. Note that preceding vehicle and following vehicle numbers and other quantities which depends on them like lead and lag gaps now also have to be recalculated. In total this correction modify data for more than 10% of vehicles.

2.5. The fundamental diagram

One of the most important things for analyzing traffic on road segment is fundamental diagram, which represents car flux j dependence on car density ρ. Clearly this is one of things that have to be compared with results from mathematical model. In order to draw this diagram we need calculate car flux and car density from smoothed NGSIM data.

2.5.1. Car density

Car density is a macroscopic physical quantity which represents number of cars N per length of segment of road L.

$$\rho = \lim_{N,L\to\infty} \frac{N}{L} \approx \frac{N}{L} \tag{2.5}$$

To calculate car density at time moment t we need to choose some road segment with length L and count how many cars there are at time moment t. Note, that L should be large so that results are close to the limit case. Results for calculated densities for road segment $y \in (200 : 400)\ \mathrm{m}$ for lanes 1 and 2 from subset D1 are shown in Fig. 2.11. As we can see from Fig. 2.11 we

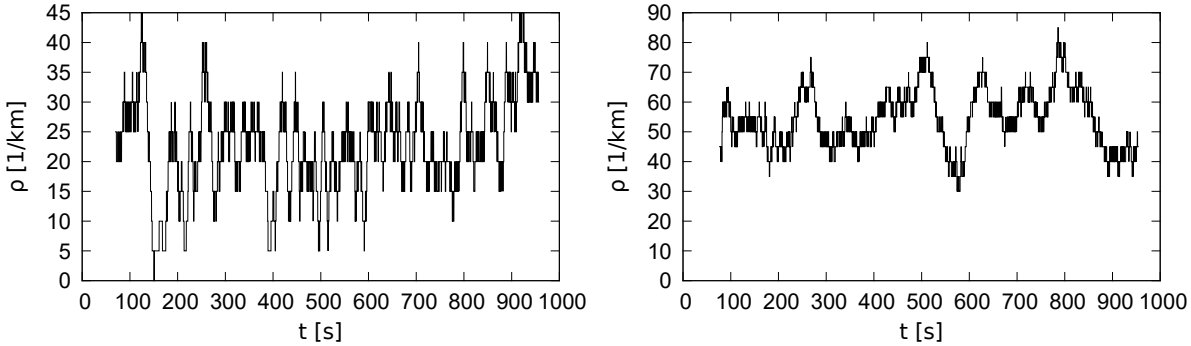

(a) lane 1 **(b)** lane 2

Figure 2.11.: Car density from lane 1 and 2 from subset D1. Car density is calculated using equation (2.5).

have discrete values of density with resolution $5\ \mathrm{km}^{-1}$. To increase resolution we can of course

increase L, but we can not increase L much, because we have only data from about $500\ \mathrm{m}$ road segment. More over we are actually interested in localized density because traffic is forward orientated and behavior of car is not influenced by traffic congestion which forms $200\ \mathrm{m}$ behind. We get better results if we either average calculated results form Eq. (2.5) over some time, or instead of fixed length L use distance between first car in this road segment and first car which is outside the road segment if first car in road segment is not too far from beginning of road segment and first car outside road segment is not too far end of road segment:

$$\rho = \begin{cases} \frac{N}{y_{N+1}-y_1} & \text{if } y_{start} - y_1 > \delta \text{ and } y_{N+1} - y_{end} > \delta \\ \frac{N}{L} & \text{else} \end{cases} \tag{2.6}$$

here δ is some constant, y_{start} is y-coordinate of beginning of road segment with length L, y_{end} is y-coordinate of end of road segment with length L, y_i is y-coordinate of i-th car and cars are numbered descending according to their coordinates and first car in the road segment has index 1. This is some mixture between macroscopic density and on road segment with length L averaged microscopic density (Eq. (2.7)) also frequently used for density calculations in traffic data analysis.

$$\rho = \frac{1}{\langle s \rangle}\,, \quad \langle s \rangle = \frac{1}{N}\sum_{i=2}^{N+1} s_i\,, \quad s_i = y_{i-1} - y_i\,, \tag{2.7}$$

where s is spacing between cars (also know as distance headway) and indexes have the same meaning for Eq. (2.6). Clearly Eqs. (2.5) and (2.7) and therefore also Eq. (2.6) in limit case $L, N \to \infty$ give the same results. Eq. (2.6) in limit case $\delta \to 0$ becomes Eq. (2.5) and $\delta \to \infty$ becomes Eq. (2.7). Note that Eq. (2.7) can not be applied directly for density calculations, because as we have data of only $500\ \mathrm{m}$ road segment, for dilute traffic cases we sometimes do not know value s_N. If we want to calculate density for some segment of the road, the value of parameter delta δ should not be too large and also it should be larger average car length, so for road segment $y \in (200 : 400)\ \mathrm{m}$ value $\delta = 40\ \mathrm{m}$ seems to be reasonable and will be used for further calculations. Also time averaging for large times makes no sense, but averaging over $1\ \mathrm{s}$ seems reasonable. By using time averaging of $1\ \mathrm{s}$ for Eq. (2.5) we get resolution of $0.5\ \mathrm{km}^{-1}$ which is definitely better. We can also try to apply time averaging to Eq. (2.6). These approaches for lanes 1 and 2 from subset D1 are compared in Fig. 2.12. As we can see form Fig. 2.12, we have improvements if we use time averaging for Eq. (2.6). But as traffic in lane 1 is quite dilute the improvements for resolution by using Eq. (2.6) are not so good and therefore

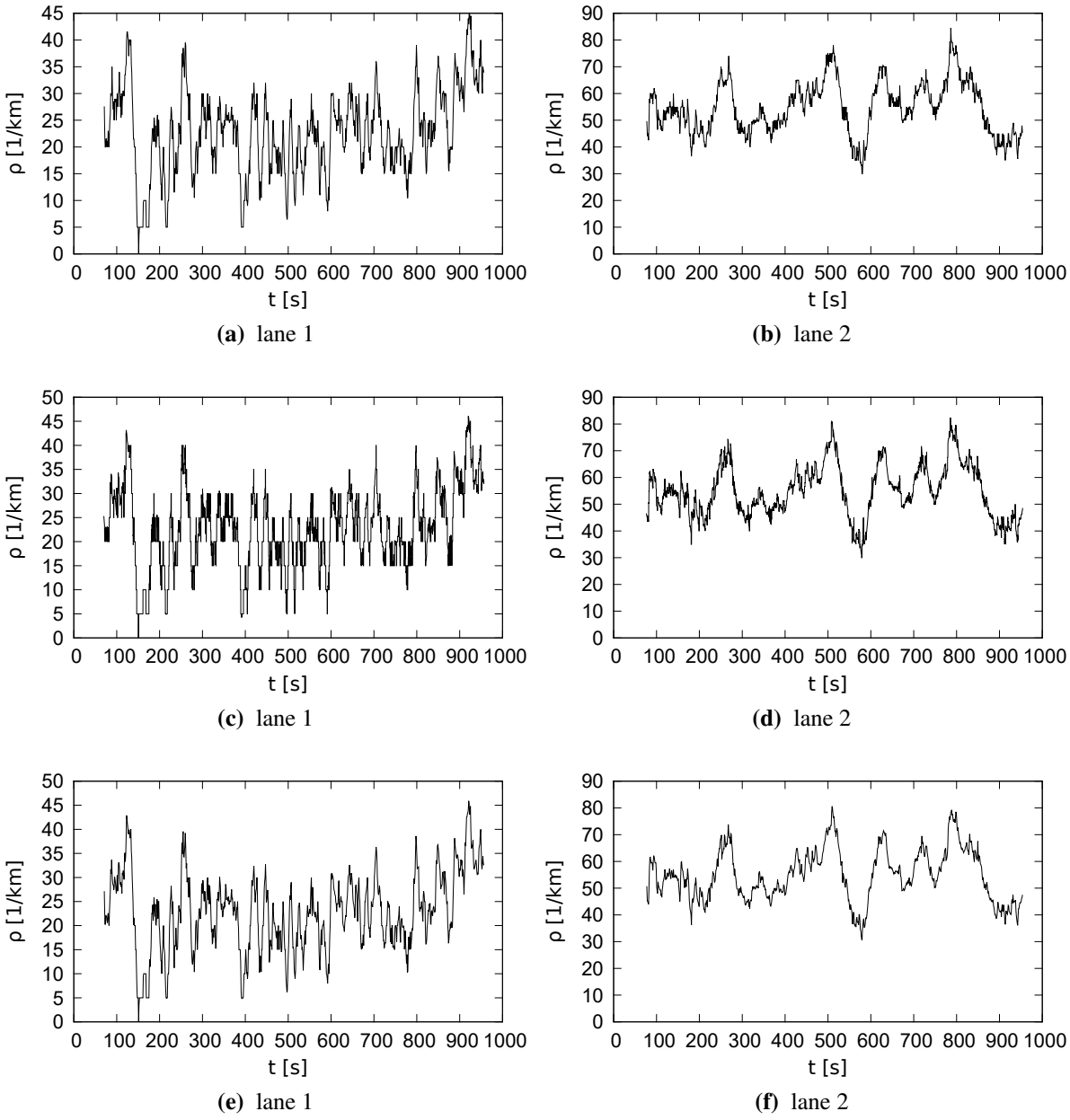

(a) lane 1 **(b)** lane 2

(c) lane 1 **(d)** lane 2

(e) lane 1 **(f)** lane 2

Figure 2.12.: Comparison between different approaches to calculate car density from lane 1 and 2 from subset D1. For Figs. (a)–(b) car density is calculated by time averaging for 1 s Eq. (2.5), Figs. (c)–(d) car density is calculated from Eq. (2.6) with $\delta = 40$ m, Figs. (e)–(f) car density is calculated by time averaging for 1 s Eq. (2.6) with $\delta = 40$ m.

we see that Eq. (2.6) works better for denser traffic. As time averaging increase resolution for dilute traffic case and we do not need to know density values after every 0.1 s and values after 1 s are still acceptable for further calculations of density 1 s time averaging for Eq. (2.6) will be used.

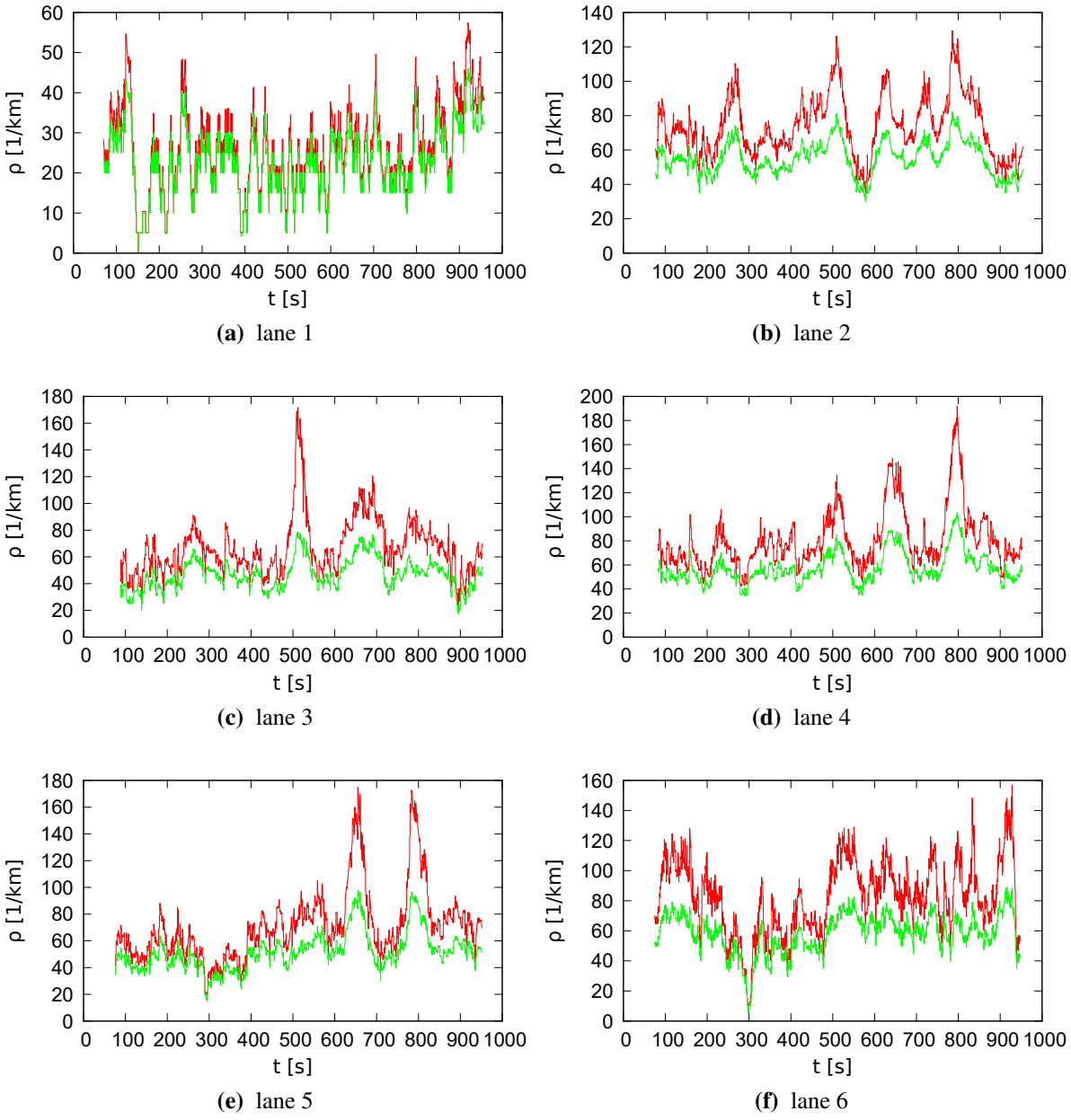

(a) lane 1 **(b)** lane 2 **(c)** lane 3 **(d)** lane 4 **(e)** lane 5 **(f)** lane 6

Figure 2.13.: Comparison between car density ρ and effective car density $\bar{\rho}$ for all lanes from subset D1. Green line represents car density and red line represents effective car density.

But there is still one more problem if we want to compare calculated density from empirical traffic data with results from mathematical models. Vehicles in I-80 data set have different length and if we do not have the same car length distribution in mathematic model as in I-80

data set, we can not compare densities, because as we can see from Tabs. 2.1-2.3 we have almost 4% trucks and truck length may be several times bigger than length of passenger car. To remove these differences we can modify Eq. (2.6) from denominator subtracting all length of cars l_i and adding a typical car length l_0 used in model instead:

$$\bar{\rho} = \begin{cases} \frac{N}{y_{N+1} - y_1 - \sum\limits_{i=1}^{N} l_i + N l_0} & \text{if } y_{start} - y_1 > \delta \text{ and } y_{N+1} - y_{end} > \delta \\ \frac{N}{L - \sum\limits_{i=1}^{N} l_i + N l_0} & \text{else} \end{cases} \tag{2.8}$$

and call this effective car density $\bar{\rho}$, but as for mathematical models of traffic usually point like cars are used, we can set $l_0 = 0$

$$\bar{\rho} = \begin{cases} \frac{N}{y_{N+1} - y_1 - \sum\limits_{i=1}^{N} l_i} & \text{if } y_{start} - y_1 > \delta \text{ and } y_{N+1} - y_{end} > \delta \\ \frac{N}{L - \sum\limits_{i=1}^{N} l_i} & \text{else} \end{cases} \tag{2.9}$$

and for dense traffic we can see that this is just reciprocal of space average of lead gap g:

$$\bar{\rho} = \frac{1}{\langle g \rangle}, \quad \langle g \rangle = \frac{1}{N} \sum_{i=2}^{N+1} g_i, \quad g_i = y_{i-1} - y_i - l_{i-1}. \tag{2.10}$$

The difference between car density and effective car density can be seen in Fig. 2.13. One can see that from effective density plots it is more easy to see congestions.

2.5.2. Car Flux

Car flux is a macroscopic physical quantity which represents number of cars in one lane N passed certain point on road per time interval ΔT.

$$j = \frac{N}{\Delta T}. \tag{2.11}$$

To calculate car flux at time moment $t + \Delta T/2$ we need to count how many cars passed some point between time moment t and $t+\Delta T$. Such calculated results for $y = 300$ m and $\Delta T = 30$ s for lanes 1 and 2 you can see in Fig. 2.14. showing that also car flux has discrete values, and we can only calculate flux at limited number of time points. Also we can see that the car flux in

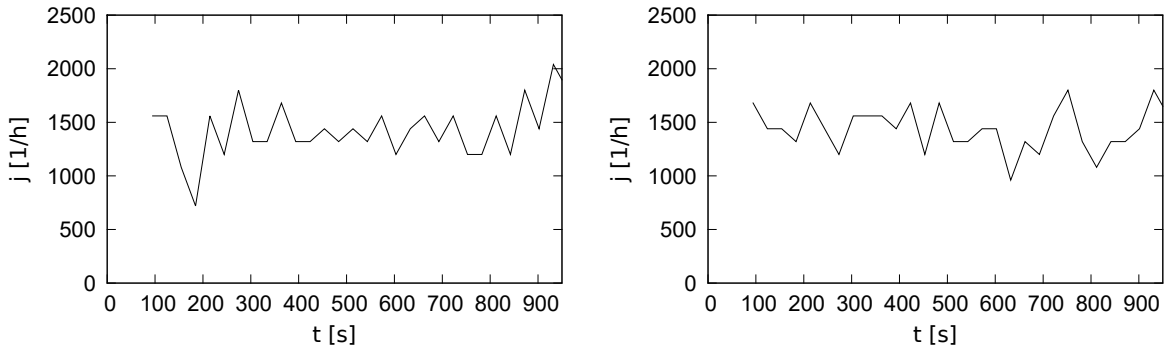

(a) lane 1 **(b)** lane 2

Figure 2.14.: Car flux changes in time for lane 1 and lane 2 of subset D1. Car flux is calculated form Eq. (2.11) with $y = 300$ m and $\Delta T = 30$ s.

lane 1 has similar value as in lane 2 despite big differences for the car density. This shows that vehicles in lane 1 drives much faster and now we finally can confirm that lane 1 is high-speed lane.

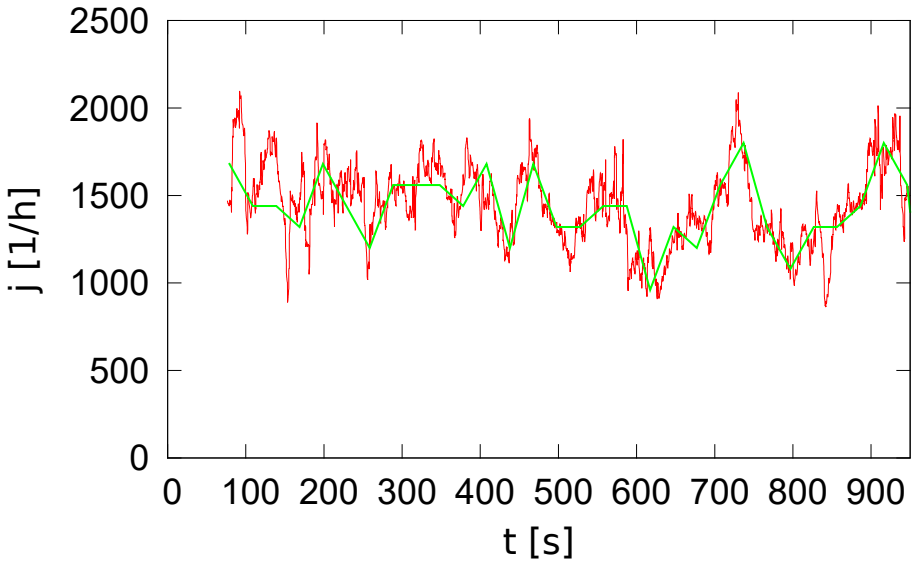

Figure 2.15.: Comparison between microscopic and macroscopic car fluxes for lane 2 of subset D1. Green line represents macroscopic car flux and red line microscopic car flux. Car density is calculated form Eq. (2.6).

To increase number of time points in which we can calculate flux, instead of macroscopic car flux we can use microscopic one, which can be calculated from

$$j = \rho \cdot \langle v \rangle \ ; \quad \langle v \rangle = \frac{1}{N} \sum_{i=i}^{N} v_i \, , \tag{2.12}$$

where $\langle v \rangle$ is space mean velocity. The comparison between macroscopic and microscopic car fluxes for lane 2 of subset D1 can be seen in Fig. 2.15. As expected Fig. 2.15 shows that microscopic and macroscopic fluxes of course good match.

As we did with car density also for flux we can introduce effective car flux $\bar{j}$, which should be for equivalent of car flux, if all vehicles had no length

$$\bar{j} = \bar{\rho} \cdot \langle v \rangle \ . \tag{2.13}$$

The difference between car flux and effective car flux can be seen in Fig. 2.16. Note, that if we

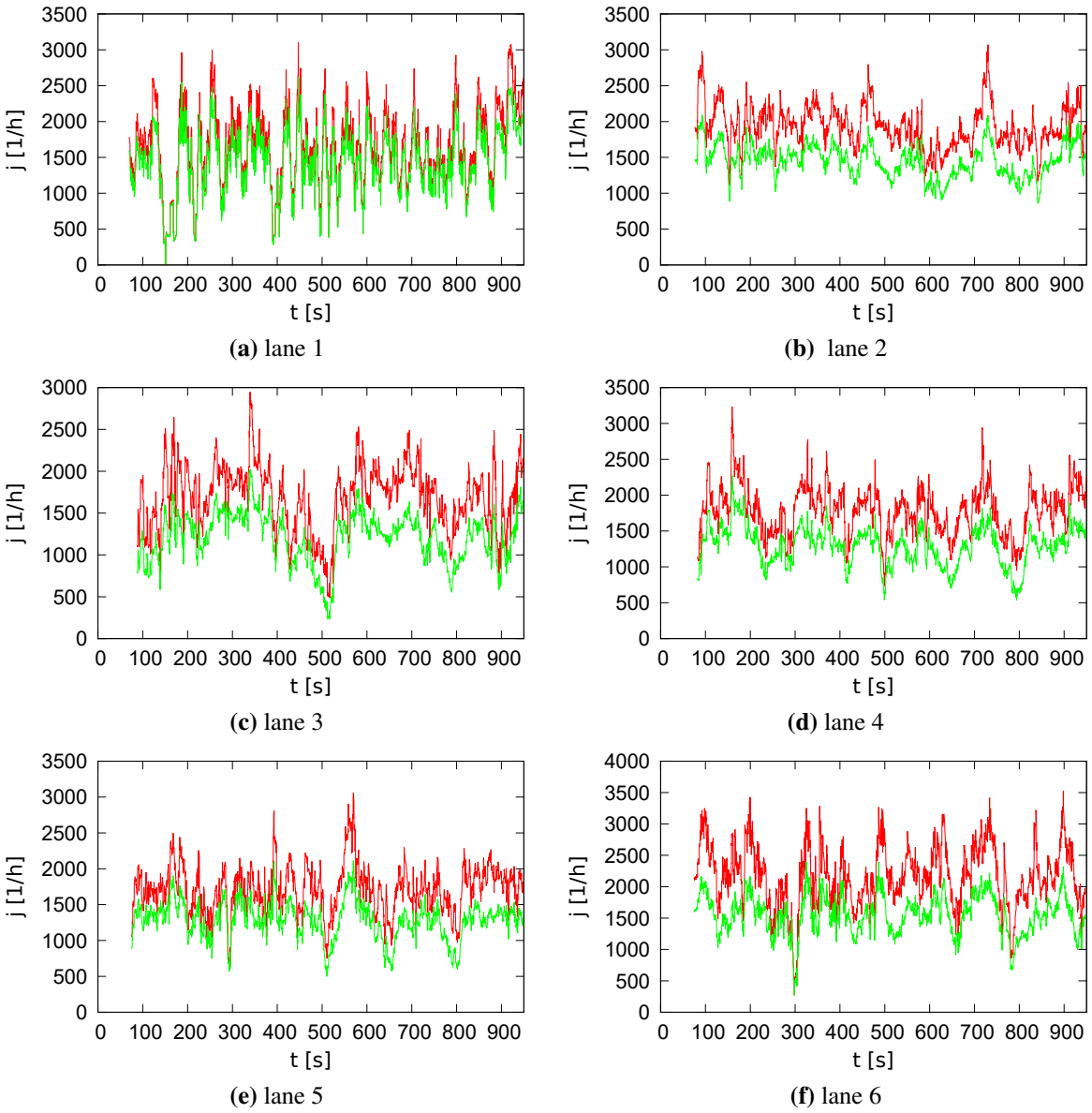

(a) lane 1 **(b)** lane 2 **(c)** lane 3 **(d)** lane 4 **(e)** lane 5 **(f)** lane 6

Figure 2.16.: Comparison between car flux j and effective car flux $\bar{j}$ for all lanes from subset D1. Green line represents car flux and red line represents effective car flux.

have congestion, than effective car flux in Fig. 2.16 has to have (local) minimum at this time moment and effective car density has to have (local) maximum. We can see this for example at $t \approx 500$ s on lane 3. However it is simpler to detect if we plot space average speed over time or in space-time plots like in Fig. 2.5.

2.5.3. Fundamental diagrams

Now when we have calculated car density and car flux we finally can plot fundamental diagrams and compare with traffic physics theory. From traffic physics theory [16] follows that fundamental diagrams usually have inverted λ-shape (see Fig. 2.17). As we can see from Fig. 2.17 in

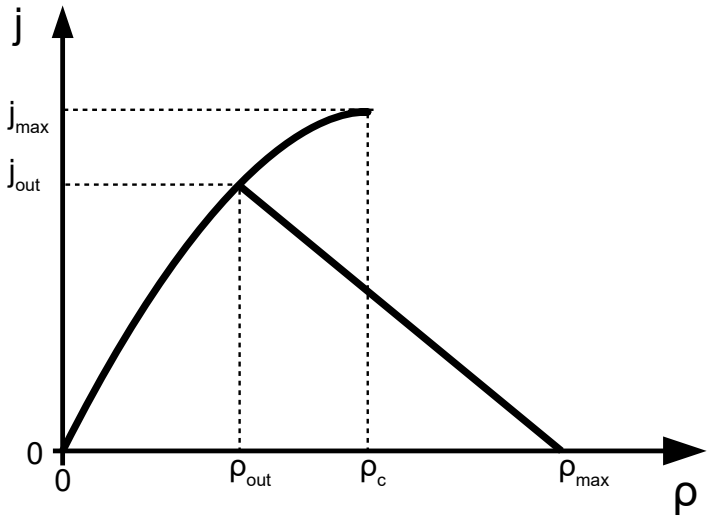

Figure 2.17.: Inverted λ-shape fundamental diagram.

density range $\rho \in (\rho_{out}; \rho_c)$ we have multi-valued fundamental diagram and therefore we can observe hysteresis. First branch for small density $\rho \in (0; \rho_c)$ describes free flow, and second branch for high density $\rho \in (\rho_{out}; \rho_{max})$ describes congested flow. In the free-flow, the flux steadily rises with increasing density and small perturbations in the traffic flow have no significant effects. This continues until critical density ρ_c is reached. At the critical density, traffic becomes metastable and small perturbations leads to a cascading effect, resulting in a breakdown of traffic and kicking it onto the congested branch. When we are on congested branch and decrease density, flux linearly increases until density ρ_{out} is reached. In region $\rho \in (\rho_{out}; \rho_c)$ we do not have transition from congested flow to free flow, because in this region congested flow is also stable for small perturbations. Only when bifurcation point (ρ_{out}, j_{out}) is reached finally we return to free flow branch.

Fundamental diagrams for lanes 1 till 6 from I-80 data set (all subsets are included) can be seen in Fig. 2.18. From Fig. 2.18 we conclude that only lane 1 has a free traffic flow branch and

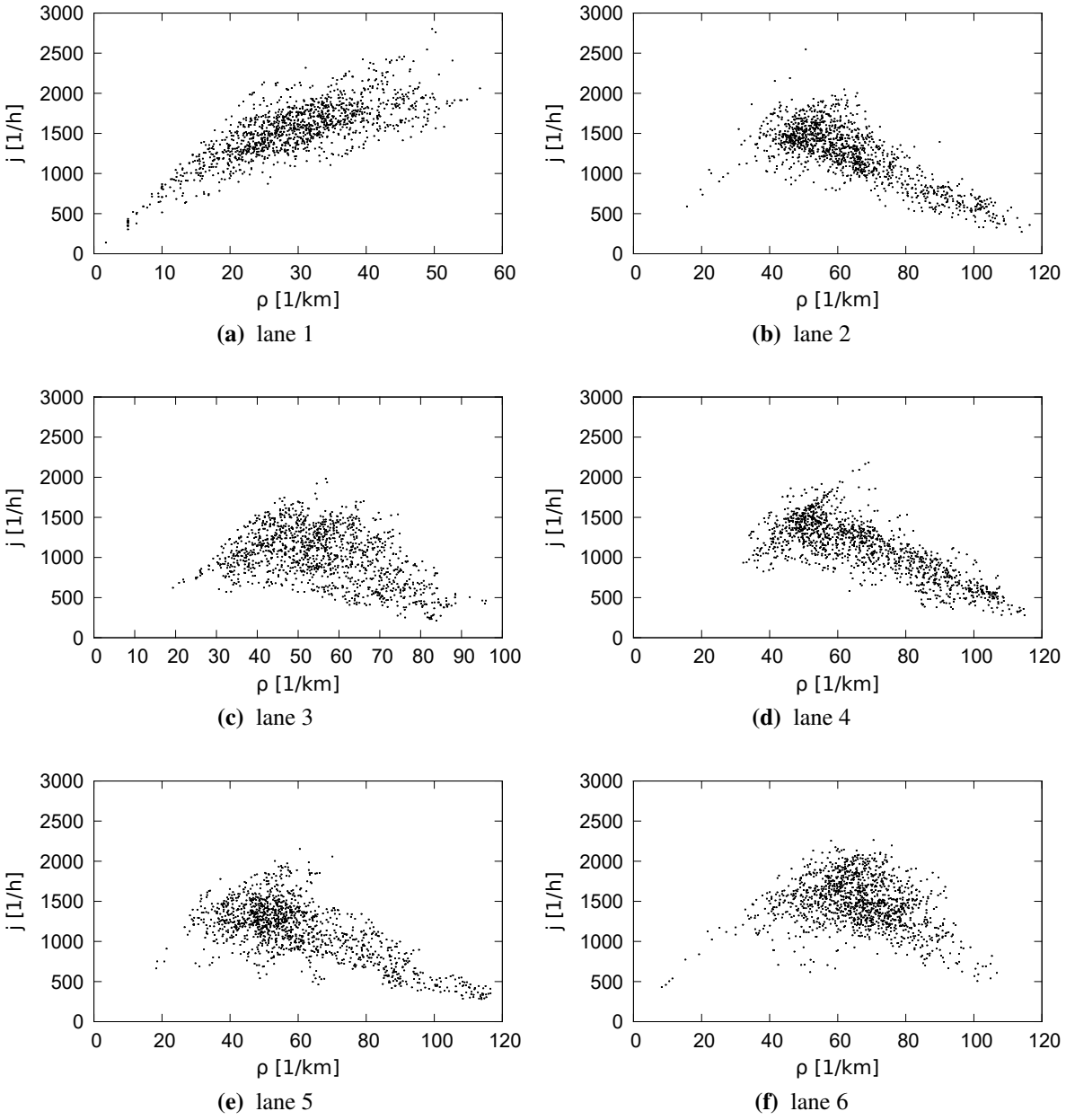

(a) lane 1 **(b)** lane 2

(c) lane 3 **(d)** lane 4

(e) lane 5 **(f)** lane 6

Figure 2.18.: Fundamental diagrams for lanes 1 till 6 from I-80 data set (all subsets are included).

all other lanes have congested traffic flow (congested traffic branch). To understand better we can look at data points from lanes 1 till 6 in the same coordinates (see Fig. 2.19a). Here clearly we see that lane 1 has other traffic properties then other lanes. From Fig. 2.19a we see that fundamental diagram has inverse λ shape, but data points has large deviations from average. As before for better comparison to mathematical models we have defined effective density $\bar{\rho}$ and

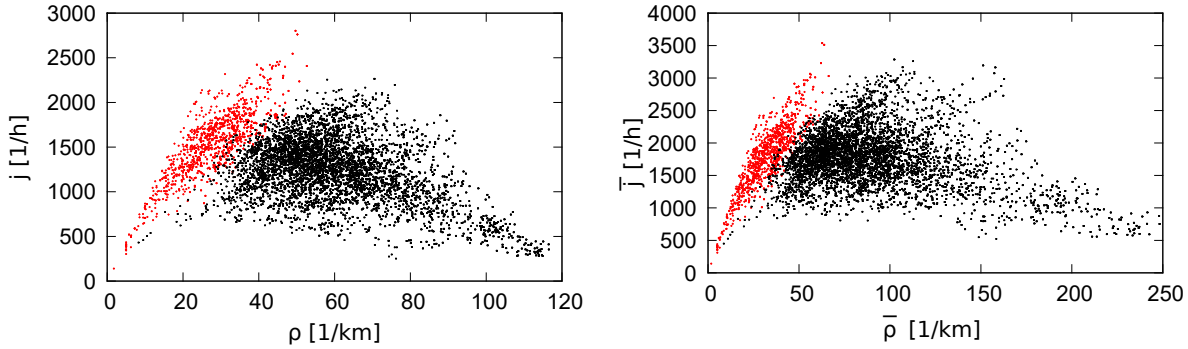

(a) fundamental diagram **(b)** effective fundamental diagram

Figure 2.19.: Comparison between fundamental diagram and effective fundamental diagram for all lanes of I-80 data set (all subsets are included). Data points from lane 1 are marked in red color and for other lanes in black color.

effective flux $\bar{j}$, we can also plot fundamental diagram using these data. For analogy lets call this effective fundamental diagram (see Fig. 2.19b). But also for effective fundamental diagram we see large deviations from average. Clearly one reason for large deviations from average is stochasticity, but other not less reason is lane changes. If we want to compare with models which do not take in account lane changes we need to exclude this effect. This effect according to [10] can be excluded by averaging flux and density over all lanes. However in this case this is not smart choice, because lane one has free flow, but other lanes has congested flow. The obviously better is to average over lanes which have free flow and lanes which have congested flow separately even when there are few lane changes from congested flow to free flow. As we have only one lane with free flow there is no need to average, but for congested flow we have to average over five lanes. By doing this (see Fig. 2.20), we see that we get much smaller

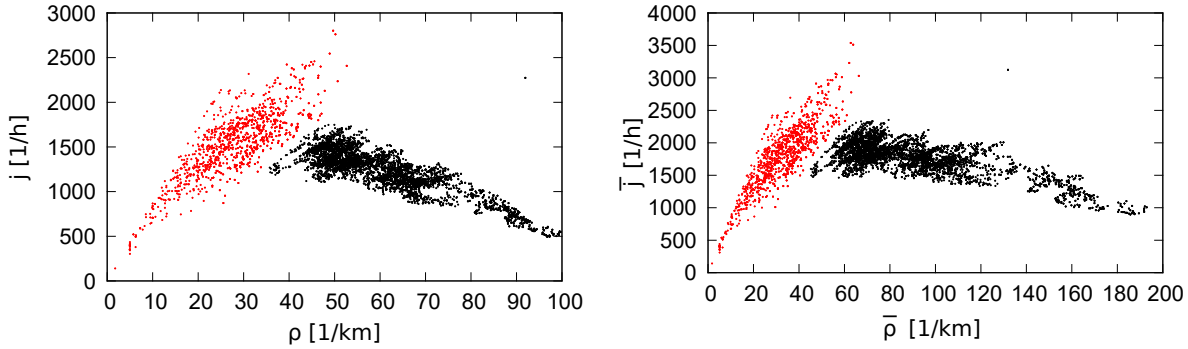

(a) fundamental diagram **(b)** effective fundamental diagram

Figure 2.20.: Comparison between fundamental diagram and effective fundamental diagram for for I-80 data set (all subsets are included). To remove lane change effects in congested flow, density and flux was averaged over lane 2 till 6.

deviations from average. We can conclude that this method at least partly removes effects of lane changing. As we can see from Fig. 2.20 there is no big difference between fundamental diagram and effective fundamental diagram except scale, but for large densities we see that congested part is not more linear.

2.6. Field data

Since fundamental diagram is very important for analysis of traffic, then for verification and improvement of microscopic traffic model we are more interesting in how car's acceleration or speed depends on lead gap or velocity difference between this car and car in front $\Delta v_i = v_i - v_{i-1}$ and other quantities. In the simplest realistic case the speed with which car wants to drive should at least depend on lead gap g (instead of lead gap one can also use time or distance headway) and velocity difference between this car and car in front, so in this case we would like to find acceleration $a_i = f(v_i, g_i, \Delta v_i)$ from vehicle trajectory data. Unfortunately it leads to problem of analyzing four dimensional plots. As stochasticity plays important role, to do this directly is almost impossible. The simplest thing what we can do is to look at projections to all six planes planes (g-v plane; g-Δv plane; g-a plane; v-a plane; v-Δv plane; Δv-a plane) instead. These projections can be seen in Fig. 2.21. Note that as before for every data point time averaging of 1 s also for projection to planes was used. But due to stochasticity data are scattered and the better option of course to to look at probability density of those plots (see Fig. 2.22).

But unfortunately if we look to plots containing velocity (see Figs. 2.22a, 2.22k and 2.22g) we see some strange patterns. As the result also for probability densities (see Fig. 2.22) for plots containing velocity we do not have smooth functions, but with several local minimums and maximums, especially good we can see this in Figs. 2.22g and 2.22h. Note that we get similar results if we use the velocities and acceleration directly from data sets, so Savitzky - Golay filter is not the cause of these artifacts.

The better understanding of cause we get if we look to the velocity - space plot (velocity of all cars in subset D1 against y-coordinate) (see Fig. 2.23) or velocity - time plot (see Fig. 2.24) with velocity in feet/s. As we can see from Figs. 2.23 and 2.24 it seems that cars like to drive with velocity which is almost precisely 5, 10, 15, 20,... in feet/s more than with the values between these velocities independent of time and position (except of camera 1 range). The exception is

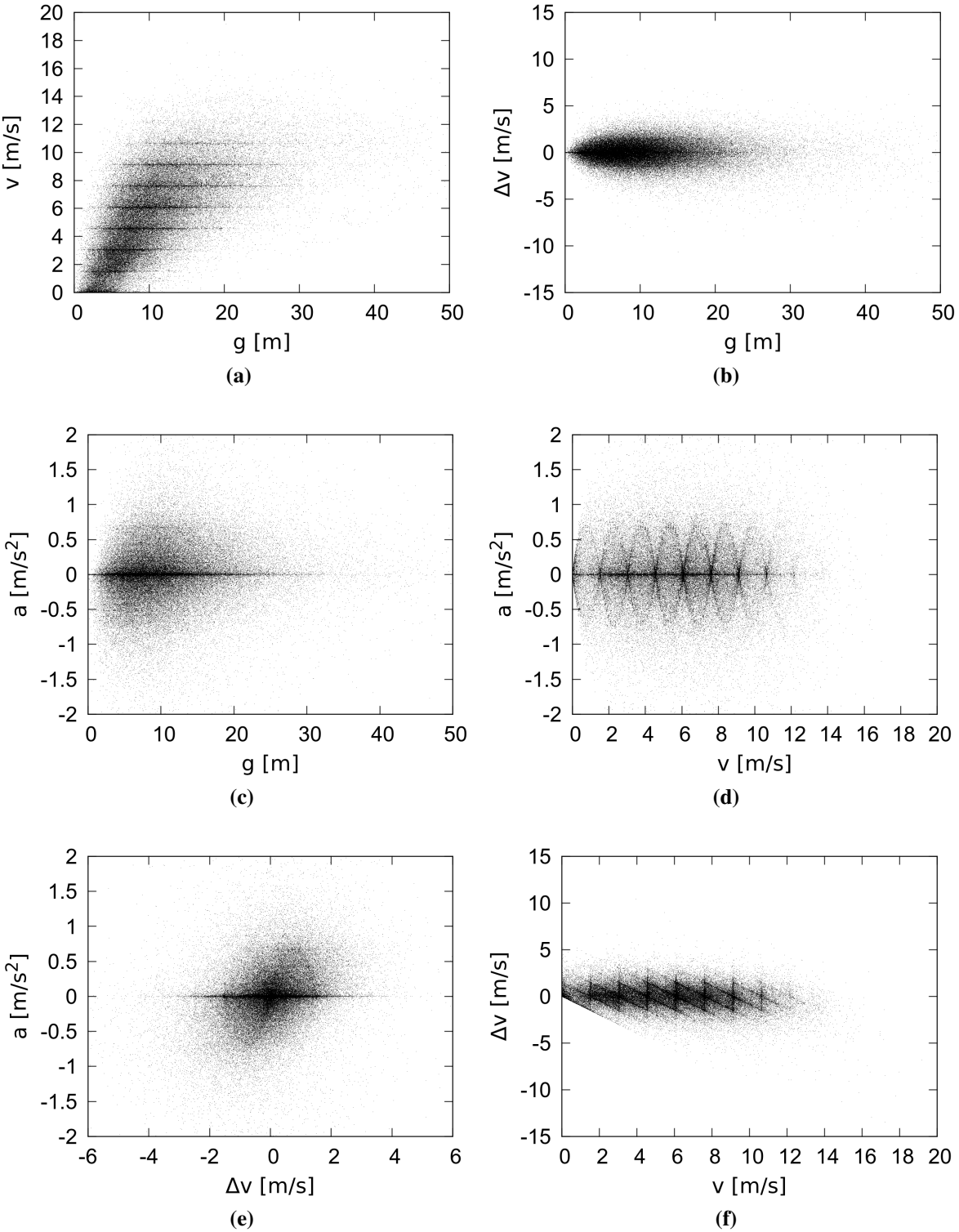

Figure 2.21.: Projection of $a_i = f(v_i, h_i, \Delta v_i)$ to all 6 planes for I-80 data set.

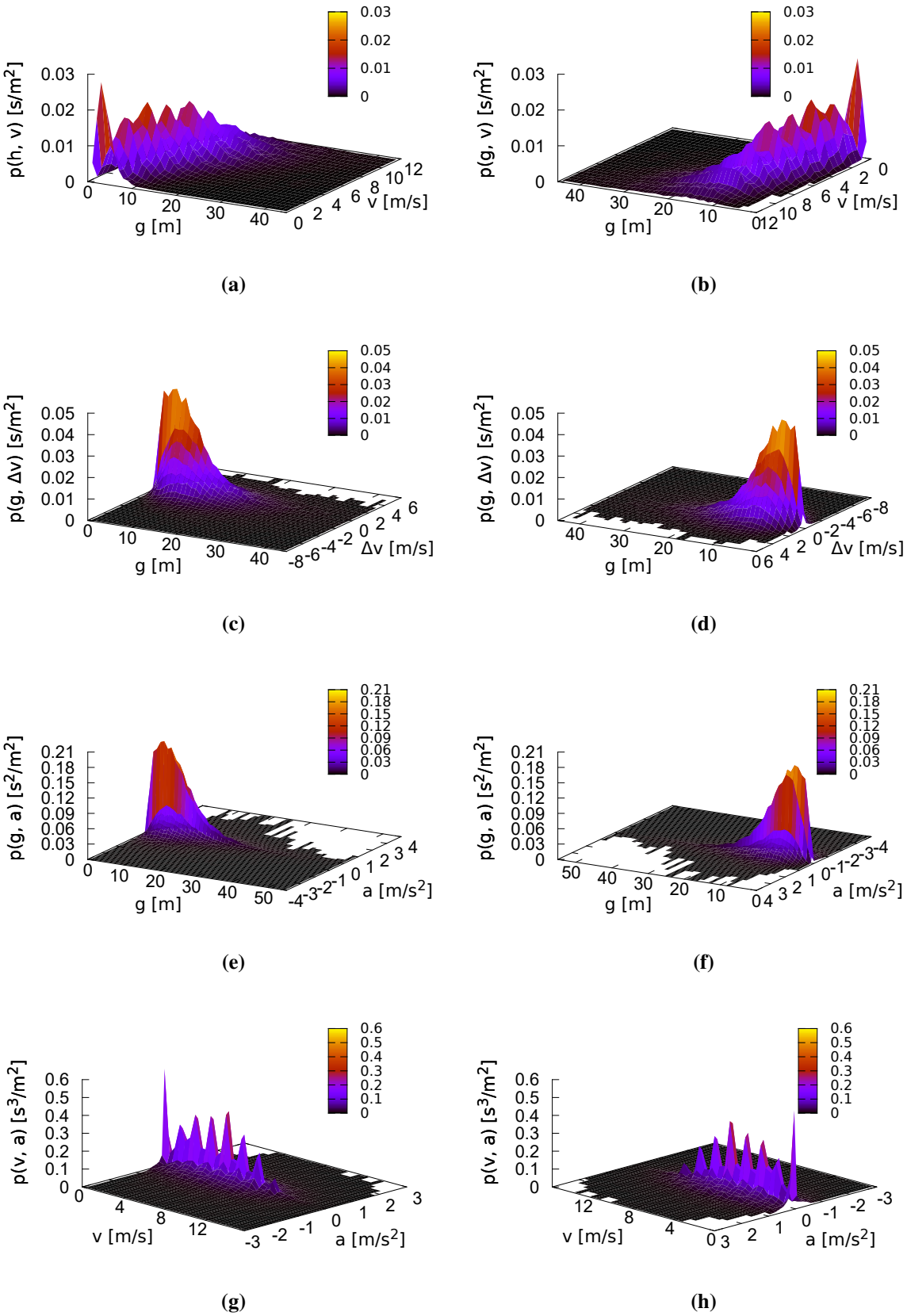

Figure 2.22.: Continued on next page.

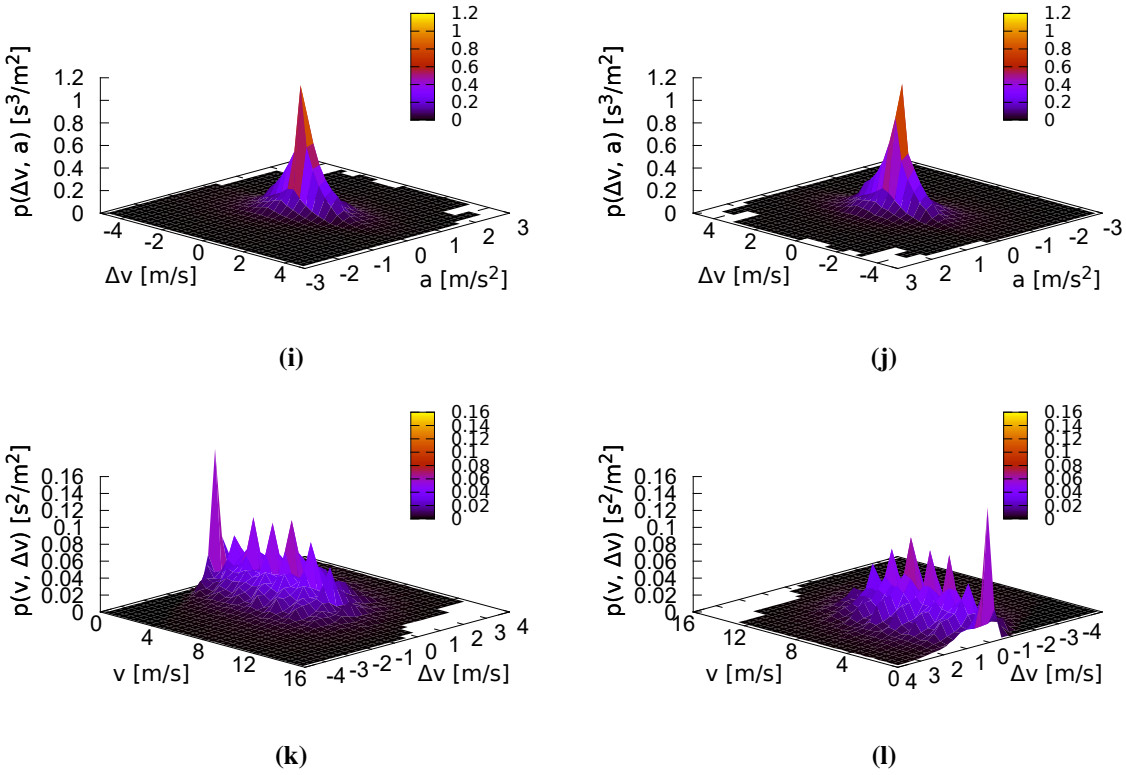

Figure 2.22.: Probability densities of projection of $a_i = f(v_i, g_i, \Delta v_i)$ to all 6 planes from I-80 data set.

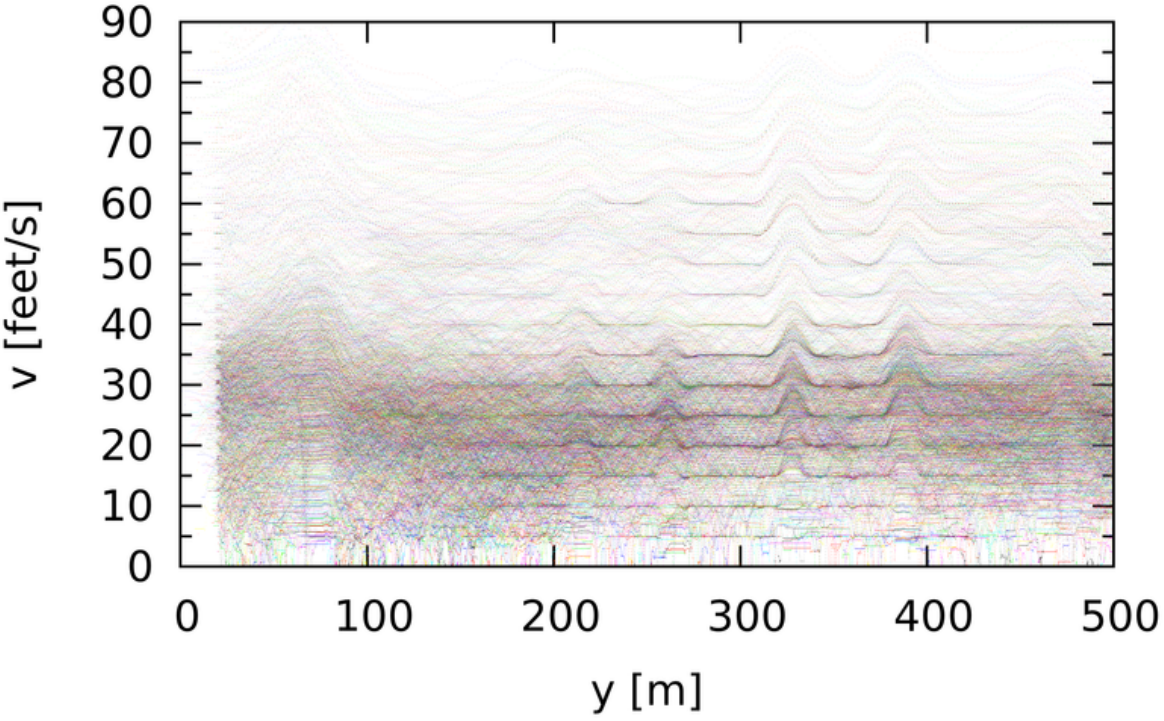

Figure 2.23.: Velocity - space plot of all cars in subset D1.

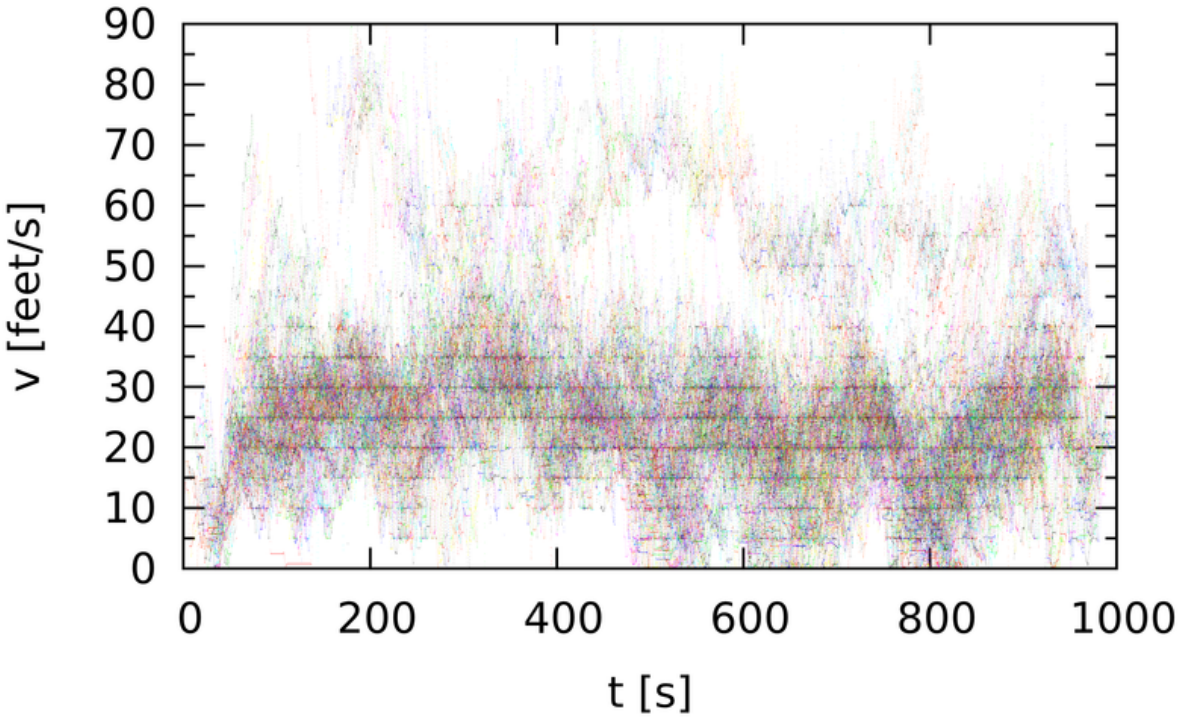

Figure 2.24.: Velocity - time plot of all cars in subset D1.

regions of changing cameras where now we can see that the cars do not like to drive any more with velocity 5, 10, 15, 20, ... in feet/s, but want to drive with parabolic like velocity profiles of position (see Fig. 2.23 where changes from camera 2 to 3 is at $y \approx 210$ m, from 3 to 4 at $y \approx 260$ m, from 4 to 5 at $y \approx 330$ m, from 5 to 6 at at $y \approx 390$ m, from 6 to 7 at $y \approx 480$ m). Clearly these parabolic like profiles are artifacts of video post-processing NG-VIDEO and also the fact that cars want to drive with velocities which almost precisely 5, 10, 15, 20,... in feet/s should also be artifacts of video post-processing NG-VIDEO. Obviously there is no reason why in reality drivers would like to drive more with these speeds because even speedometers in cars are graduated in mph (or in km/h) not in feet/s. The important question is how these artifacts were produced.

Christof Liebe in his PhD thesis [18] suggested that these artifacts were generated because of discrete nature of determination of y-coordinate. But it does not seem to be the case, because if we look to speed - space plots (see Fig. 2.25) for single car we see that a car is driving also with constant velocities up to 5 or even 8 seconds with values which are randomly distributed between 5, 10, 15, 20... in feet/s. The deeper analysis of speed - space plots for individual cars shows that for almost every car there is some road segment were it drives for some time with almost constant speed which is 5, 10, 15, 20,... in feet/s. This can not be explained differently as

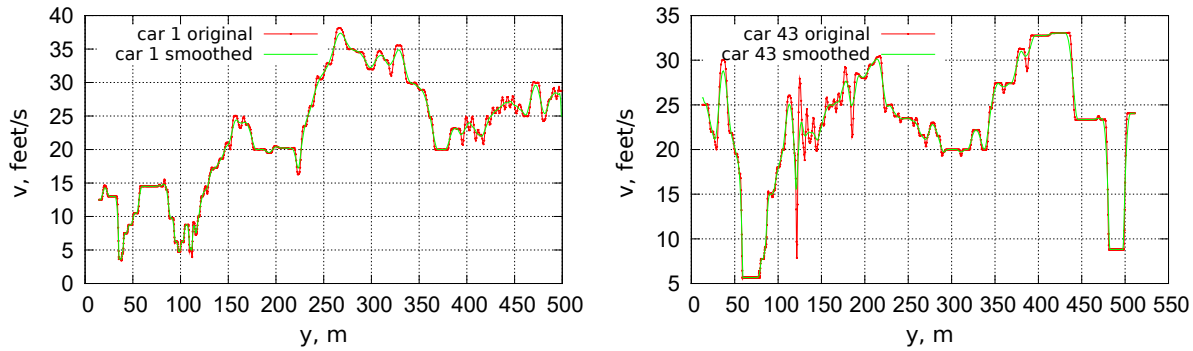

Figure 2.25.: Velocity - space plot for car number 1 and 43 form subset D1.

just it also have to be an artifact of video post-processing NG-VIDEO as well as parabolic like velocity profile of position. Most likely it has something to do with the fact that the ranges of cameras do not overlap (see Sec. 2.3). As almost every car has these artifacts, we must assume that errors for speed is at least 2.5 feet/s.

The smoother results for probability densities we get if we choose bin size for velocities so that in each bin we have exactly one value of velocity which is 5, 10, 15, 20,... in feet/s. But to remove internal structure from projection to planes plots (Fig. 2.21) is much more difficult. The only way which was found that with out modifying original data removes internal structure from velocity plots was to average data not for 1 s, but for 5 s. This approach works (see Fig. 2.26) because, as we can see in speed - space plots for individual cars, cars mostly drive with constant speed for less than 5 s. This approach removes internal structure, but we now have 5 times less

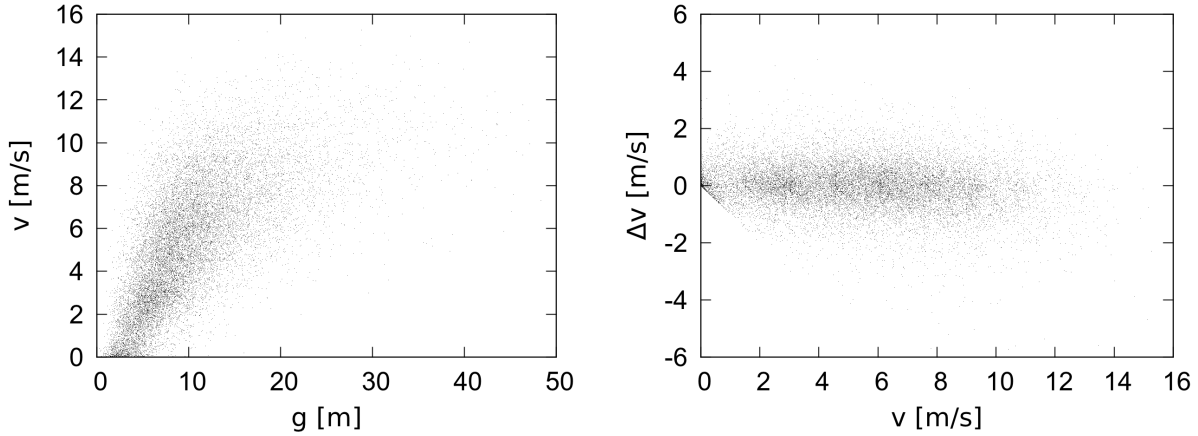

Figure 2.26.: Velocity dependence on lead gap and velocity difference dependence on velocity from I-80 data set averaged for 5 s.

points and instead more or less instantaneous velocity we have average velocity over 5 seconds which seems to be already too much averaged and we may loose some important data. The

corresponding probability densities can be seen in Fig. 2.27.

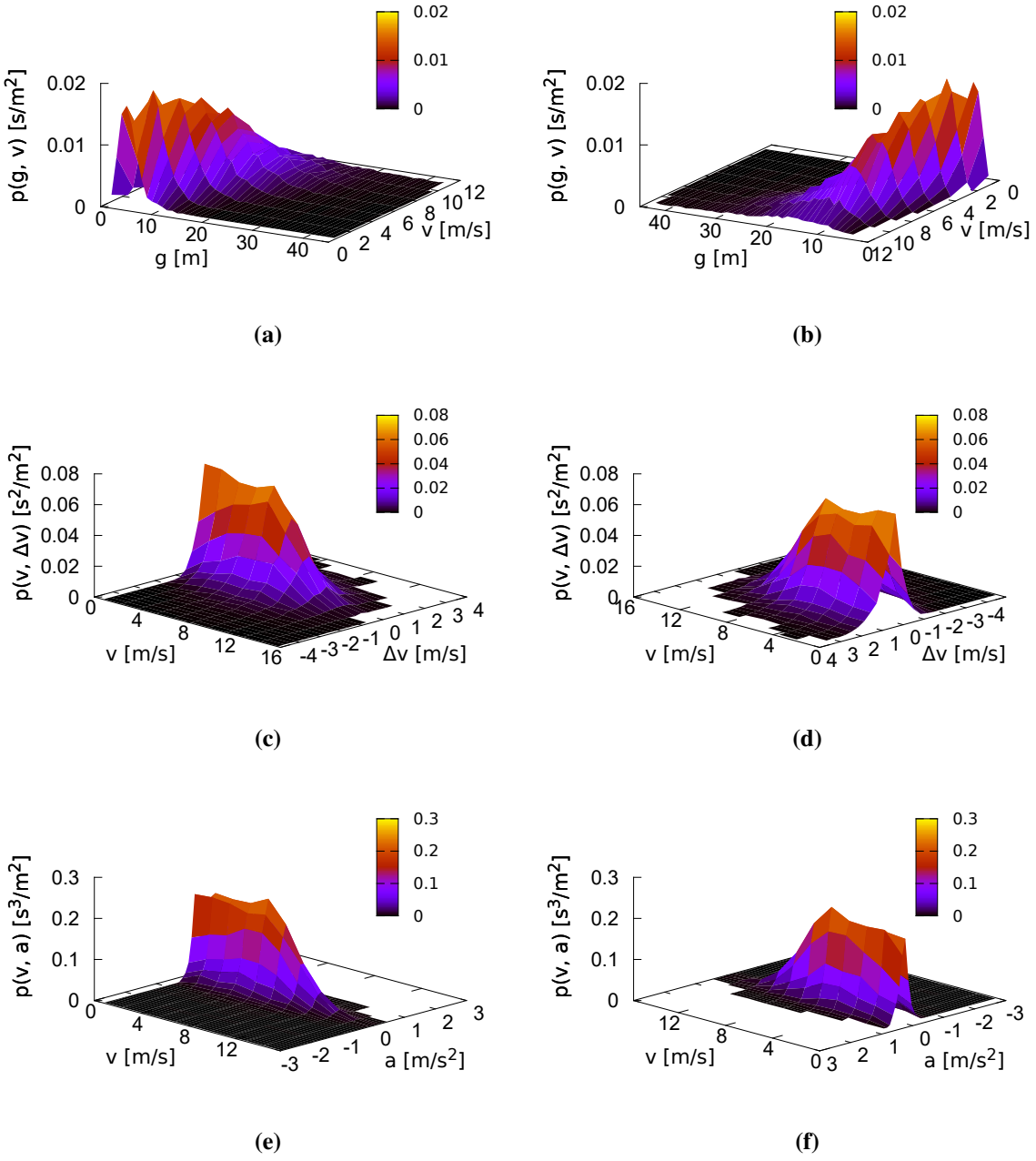

Figure 2.27.: Probability densities from I-80 data set of projection of $a_i = f(v_i, h_i, \Delta v_i)$ to planes containing velocity with 5 s time averaging and larger bins for velocity as in Fig. 2.22.

From Fig. 2.22 we can see that probability density functions $p(g, \Delta v)$ and $p(g, a)$ (Figs. 2.22c, 2.22d and 2.22e, 2.22f) has similar shape and differences are more obvious for small Δv. The similar situation we can see in Fig. 2.27 with probability density functions $p(v, \Delta v)$ and $p(v, a)$ (Figs. 2.27c, 2.27d and 2.27e, 2.27f). This indicates, that velocity difference Δv is the main cause for acceleration, but of course as we can see from Figs. 2.22i and 2.22i not only one. So

clearly for any realistic microscopic dynamical traffic model acceleration should also depend on velocity difference Δv.

2.6.1. Vector field data

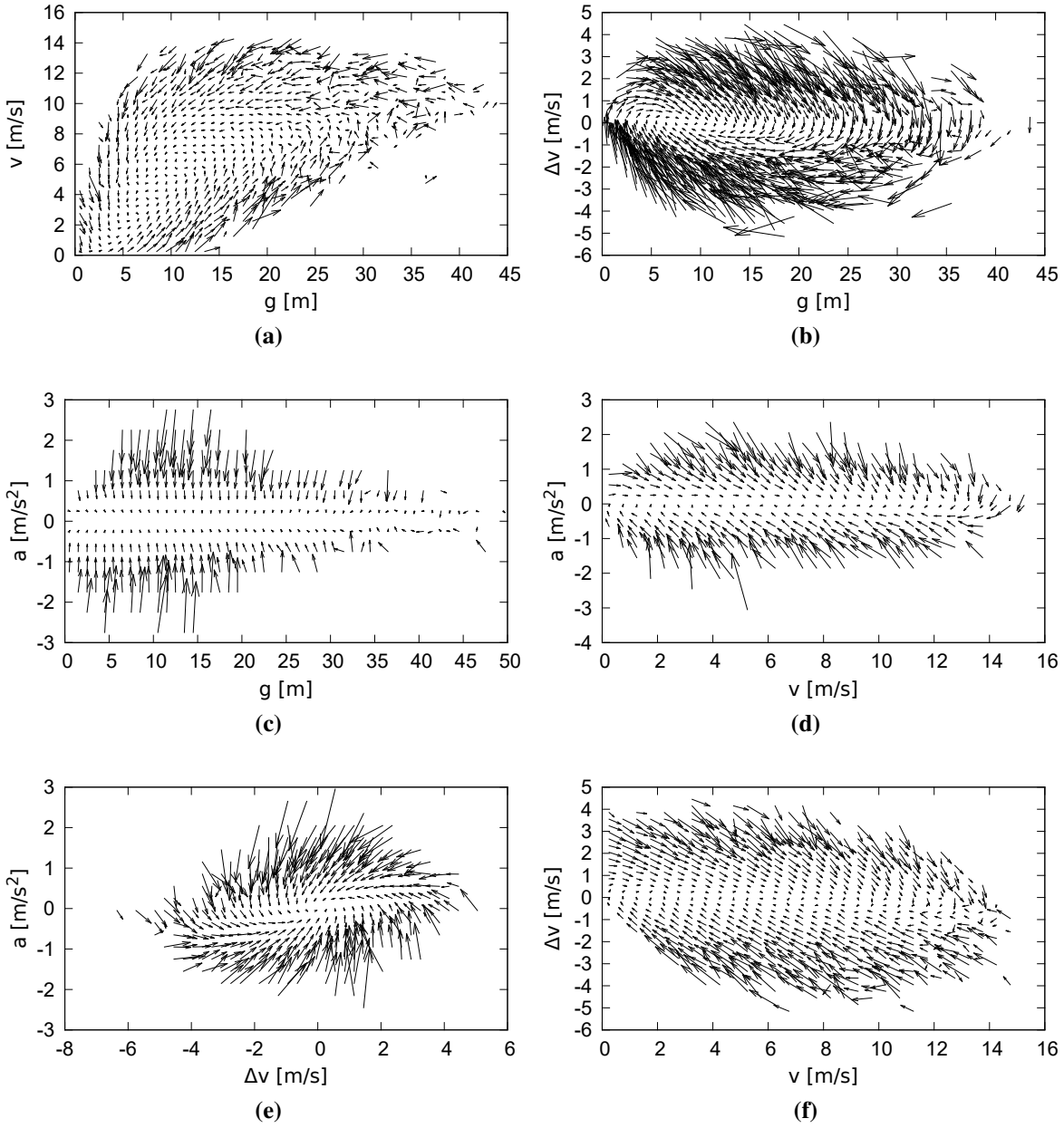

Figure 2.28.: Vector field data of projection of $a_i = f(v_i, h_i, \Delta v_i)$ to all 6 planes from I-80 data set. For plots containing acceleration vector length is scaled by $1/3$.

The other option of analyzing projections to the planes is to look at vector field data (tail of vector represent point at time moment t and head represents point at time moment $t + \Delta t$, where Δt should be small, but as we already averaged our data points over 1 s, clearly optimal value

is $\Delta t = 1$ s. As there are too many of those vectors they of course should be averaged over whole data set. The results of vector field diagrams of projections to all six planes can be seen in Fig. 2.28.

The good thing is that we do not see any clear artifacts as we saw in Fig. 2.21. This is because of average over whole data set was preformed and in this case regions with constant velocities can influence only vector length not direction which is difficult to recognize in vector field plots. Over all vector field plots seems to be more useful and more trustful for construction a microscopic dynamical traffic model.

From Figs. 2.28c, 2.28d and 2.28e (note that vectors length are scaled with scale $1/3$) we see that drivers in the cars do not like to accelerate or decelerate for long time and tries to change other parameters to drive with constant speeds (average driver is not aggressive one). From Figs. 2.28d and 2.28f we see that also vector fields as probability densities (see Fig. 2.27) for velocity - acceleration and velocity - velocity difference plots are quit similar. However vector fields for lead gap - acceleration and lead gap - velocity difference (see Figs. 2.28c and 2.28b) are completely different. Vector fields of lead gap - acceleration plot has a fix-point ($h \approx 8$ m; $\Delta v = 0$ m/s) and in general it looks like vector field of phase diagram of some stochastically driven 1D unharmonic oscillator with damping. For other plots it is difficult to say weather they have one fix-point or line segment. For lead gap - velocity plots it looks more like line segment (depending on density and other conditions position of fix-plot changes). Over all it seems that most useful for model building are lead gap - velocity, lead gap - velocity difference, velocity difference - acceleration vector field plots.

3. Microscopic model

3.1. Introduction

Microscopic traffic models try to simulate interaction between individual vehicles. Generally all these models can be divided into 3 groups:

- Car following models (with and without lane changing)
- Cellular automata models (as example see [21])
- Master equations models (as example see [19]).

Car following models (sometimes also called follow-the-leader models) assume that acceleration (for kinematic models velocity) of a driver-vehicle i is given by neighboring vehicles. The main influence comes from the leading vehicle (next vehicle $i + 1$ ahead). If model describes more than one lane highway also algorithm for lane changing has to be provided. Usually lane changing are approximated to take into account only lateral movement between neighboring lanes and drivers change lanes when they need to overtake a solver moving car or because need to take an offramp. When the driver has decided to change lanes he checks weather the gap between cars in the lane he wants to change is large enough. If gap is large enough he changes lanes [13]. As acceptable gap for lane changing varies a lot from driver to driver, the deterministic approach is bad approximation. So in further parts we will analyze only single lane traffic models.

Car following models further can be divided into deterministic and stochastic models, with time delay and without time delay models, dynamic and kinematic models. Stochastic models introduce noise into system. Models with time delay take into account reaction time τ_r which for models with time delay typically has values in range $\tau_r = 0.3 \ldots 2$ s and for models without time delay $\tau_r = 0$. Generally for deterministic dynamical model equation of motion for point

like cars can be written as

$$\begin{aligned} a_i(t+\tau_r) =& \frac{dv_i(t+\tau_r)}{dt} = f\left(g_i(t), v_i(t), \Delta v_i(t), \dots\right) \\ & \frac{dx_i(t+\tau_r)}{dt} = v_i(t+\tau_r) \ , \end{aligned} \tag{3.1}$$

where x_i is position of i-th car on the road, v_i is velocity of i-th car, a_i is acceleration of i-th car, f is some function, $g_i = x_{i+1} - x_i$ is lead gap (distance between this car and leading car), $\Delta v_i = v_{i+1} - v_i$ is velocity difference between this car and leading car. For kinematic model we can write similar equation

$$\begin{aligned} & v_i(t+\tau_r) = f_1\left(g_i(t), v_i(t), \Delta v_i(t), \dots\right) \\ & \frac{dx_i(t+\tau_r)}{dt} = v_i(t+\tau_r) \ . \end{aligned} \tag{3.2}$$

Also second equation of Eq. (3.2) can be discretized, so actually no differential equations have to be solved (for example Gipps' model [8]). For physicist, however, dynamical approach seems to be more interesting. Dynamical approach allows to better control values of acceleration and by expanding Eq. (3.2) in Taylor series up to first order any kinematic model can be transformed into dynamical one.

3.2. History of car following models

The very early car following models were proposed by engineer Reuschel [24] in 1950 and physicist Pipes [23] in 1953. These models currently are known as "two second rule" (to avoid accident drivers should drive such that time headway is at lest 2 seconds) thought in driving schools.

The first dynamical models depended only on velocity difference between leading and following cars

$$\frac{dv_i(t)}{dt} = \frac{1}{T}\Delta v_i(t) \ , \tag{3.3}$$

where T is a relaxation parameter. Clearly Eq. (3.3) describes only stable system. To produce some instabilities Chandler et al. in 1958 proposed to include explicit reaction time $\tau_r \approx 1.3$ s into model Eq. (3.3)

$$\frac{dv_i(t+\tau_r)}{dt} = \frac{1}{T}\Delta v_i(t) \ . \tag{3.4}$$

It can be shown numerically that for $\tau_r/T > 0.55$ variations of individual velocity densities will be amplified, which leads to stop-and-go traffics and accidents. However, Eq. (3.4) still does not depends on distance between vehicles. To fix this problem in 1959 Gazis et al. modified Eq. (3.4) [6] by making relaxation time gap depending:

$$\frac{dv_i(t+\tau_r)}{dt} = \lambda \frac{\Delta v_i(t)}{g_i} \ , \tag{3.5}$$

where λ is control parameter and $T(g_i) = \frac{1}{\lambda} g_i$. In 1961 Gazis et al. generalized model even further into what is is called General Motors non-linear model [7]:

$$\frac{dv_i(t+\tau_r)}{dt} = \lambda v_i^m \frac{\Delta v_i(t)}{g_i^l} \ , \tag{3.6}$$

where λ, l, m are model parameters and may be non-integer numbers. Clearly parameters l, m has no physical meaning and also λ has some crazy dimension.

In the next years many other multi-parameter models were created. In these models most of parameters where introduced just for larger shape control of function with no physical meaning. Situation quite changed in 1994 when Bando et al. published optimal velocity model (OVM) [3] (see Sec. 3.3). The difference to other models is that it is a very simple model, but still shows phase transitions. It has small number of parameters, which all has physical meaning, and there is no time delay. But for actual traffic simulations OVM is not really suitable because it gives higher values of acceleration and deceleration then observed in real traffic.

One improvement of OVM which try to model more precisely what drivers do and gives more realistic results for acceleration is "intelligent driver model" proposed by Treiber and Helbing [26] in 1999:

$$\begin{aligned} \frac{dv_i}{dt} &= a_{max} \left[1 - \left(\frac{v_i}{v_{max}} \right)^{\delta} - \left(\frac{g^*(v_i, \Delta v_i)}{g_i} \right)^2 \right] \\ \frac{dx_i}{dt} &= v_i \ , \end{aligned} \tag{3.7}$$

with optimal gap function which depends on velocity and velocity difference

$$g^*(v_i, \Delta v_i) = g_{min} + T_i v_i + \frac{v_i \Delta v_i}{2\sqrt{a_{max} a_{comf}}} \ , \tag{3.8}$$

where parameters a_{max} is maximal acceleration, a_{comf} is comfortable deceleration, v_{max} is

maximal velocity, $T_i = \frac{g_i}{v_i}$ is safe clearance time, g_{min} is minimal gap between cars and δ is acceleration exponent. For $\delta = 1$ cars accelerate with exponential in time acceleration and for $\delta \to \infty$ with constant acceleration. Typically value $\delta = 4$ is used. The acceleration of vehicle i can be separated into a free road term and an interaction term:

$$a_i^{\text{free}} = a_{max}\left(1 - \left(\frac{v_i}{v_{max}}\right)^{\delta}\right) \qquad a_i^{\text{int}} = -a_{max}\left(\frac{g^*(v_i, \Delta v_i)}{g_i}\right)^2 . \tag{3.9}$$

a_i^{free} describes acceleration tendency on free road, and a_i^{int} deceleration due to interaction with leader car. But unfortunately it is hard to analyze Eq. (3.7). We have really complex expressions even for steady state velocity.

3.3. Optimal velocity model

The optimal velocity model by Bando et al. [3] was first proposed in 1994. It assumes that acceleration of vehicle is dependent only on velocity of vehicle and lead gap

$$\begin{aligned} \frac{dv_i}{dt} &= \frac{1}{\tau}\left(V_{opt}(g_i) - v_i\right) \\ \frac{dx_i}{dt} &= v_i \ , \end{aligned} \tag{3.10}$$

where $V_{opt}(g_i)$ is optimal velocity function and τ is relaxation time. As this model originally is constructed for point like cars, then in origin version instead of lead gap g_i space headway was used $h_i = \Delta x_i = x_{i+1} - x_i$. So in further analysis it will be assumed, that cars are point like and instead of g_i quantity Δx_i will be used.

Historically the optimal velocity model by Bando et al. is based on kinematic time delay optimal velocity model proposed by Newell [22] in 1961:

$$v_i(t) = f(x_{i+1}(t - \tau_r) - x_i(t - \tau_r)) \ . \tag{3.11}$$

One can show that by expanding Eq. (3.11) in Taylor series and setting time-step $\Delta t = \tau_r$ we arrive to Eq. (3.10).

Originally as optimal velocity function [3]

$$V_{opt}\left(\Delta x\right) = \tanh\left(\Delta x - 2\right) + \tanh(2) \ , \tag{3.12}$$

were introduced, but in general any sigmoid optimal velocity function can be used. Nowadays many different formulations of optimal velocity function are available. One of the simplest is optimal velocity function proposed by Mahnke et al. [20]:

$$V_{opt}\left(\Delta x\right) = v_{max}\frac{\left(\Delta x\right)^2}{D^2 + \left(\Delta x\right)^2}\ , \tag{3.13}$$

where D is interaction distance and v_{max} is maximal speed which car can reach.

If we introduce dimensionless variables $\tilde{x}_i = \frac{x_i}{D}$, $\tilde{v}_i = \frac{v_i}{v_{max}}$, $\tilde{t} = \frac{t}{\tau}$, $\tilde{L} = \frac{L}{D}$, $\alpha = \frac{D}{v_{max}\tau}$, then dimensionless form of Eq. (3.10) with optimal velocity function Eq. (3.13) is

$$\begin{cases} \dfrac{d\tilde{v}_i}{d\tilde{t}} = \dfrac{(\Delta\tilde{x}_i)^2}{1 + (\Delta\tilde{x}_i)^2} - \tilde{v}_i \\ \dfrac{d\tilde{x}_i}{d\tilde{t}} = \dfrac{1}{\alpha}\tilde{v}_i \end{cases} \tag{3.14}$$

For dimensionless form of Eq. (3.10) we have only 3 independent control parameters: α and from boundary and initial conditions dimensionless track length $\tilde{L}$ and number of cars on track N.

3.4. Improvement of optimal velocity model

The optimal velocity model by Bando et al. is very simple model and in the same time it shows phase transitions, hysteresis and produces reverse λ-shape fundamental diagram (see Fig. 3.1).

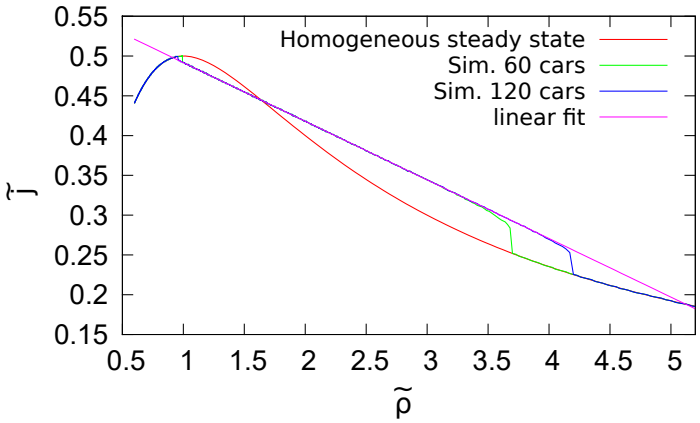

Figure 3.1.: Fundamental diagram for OVM by Bando et al. calculated using Eq. (3.14) with $\alpha = 1.1$, $\tilde{\rho} = \frac{N}{\tilde{L}}$, $\tilde{j} = \tilde{\rho}\left\langle\tilde{v}\right\rangle$, where $\left\langle\tilde{v}\right\rangle$ is space mean dimensionless velocity. Red - line show homogeneous solution, green and blue lines are simulation results with 60 and 120 cars on circular road, pink line is linear fit and should correspond to limit case $N, \tilde{L} \to \infty$.

The problem is that in OVM there is no explicit velocity dependence, however, empirical field and vector field data (see Sec. 2.6) suggest for that. Also OVM model is not collision-free (see Sec. 3.6). For $\alpha < 0.9$ it is not possible to carry out any simulations due to accidents (fast moving cars brake too slow and crash into slow moving cars). Fully collision free starting from reasonable initial conditions model becomes only for $\alpha > 1.172$. This limits choice of α to $\alpha \in (1.172; \frac{3\sqrt{3}}{4} \approx 1.299)$. But for these value of α acceleration and declaration values are much larger then observed in real traffic.

These problems have been noticed already earlier and couple of models which reduces these problems have been proposed. In 1998 Helbing and Tilch proposed generalized force model (GFM) [12]:

$$\frac{dv_i}{dt} = \frac{1}{\tau}\left(V_{opt}(\Delta x_i) - v_i\right) + \lambda \mathcal{H}(-\Delta v_i)\Delta v_i \ , \tag{3.15}$$

where λ is a constant and $\mathcal{H}(x)$ is Heaviside step function. GFM only for negative velocity differences adds extra term to OVM which linearly depends on velocity differences. In 2001 Wu et al. suggested that also positive velocity difference motives following car to accelerate and created full velocity difference model (FVDF)[15]:

$$\frac{dv_i}{dt} = \frac{1}{\tau}\left(V_{opt}(\Delta x_i) - v_i\right) + \lambda \Delta v_i \ . \tag{3.16}$$

They made also further generalization and replaced constant λ with step functions

$$\lambda = \begin{cases} a & \text{if} \Delta x_i \leq \Delta x_c, \\ b & \text{if} \Delta x_i > \Delta x_c, \end{cases} \tag{3.17}$$

where a, b , Δx_c are constants. Generally even with $a = b$ FVDM gives better agreement with empirical field data than GFM [28].

Here we are going one step further and replace λ with continuous function of Δx_i. The dimensionless form of equation of motion now is:

$$\begin{cases} \dfrac{d\tilde{v}_i}{d\tilde{t}} = \dfrac{(\Delta\tilde{x}_i)^2}{1 + (\Delta\tilde{x}_i)^2} - \tilde{v}_i + \beta f(\Delta\tilde{x}_i)\Delta\tilde{v}_i \\ \dfrac{d\tilde{x}_i}{d\tilde{t}} = \dfrac{1}{\alpha}\tilde{v}_i \end{cases} , \tag{3.18}$$

where $\beta = \tau\lambda$ is constant and $f(\Delta\tilde{x}_i)$ is dimensionless function depending only on $\Delta\tilde{x}_i$. For situation when leading car is very far away (diver of the following car do not see leader car)

there should be no dependence on velocity difference. So function $f(\Delta\tilde{x}_i)$ should have property $\lim_{\Delta\tilde{x}_i\to\infty} f(\Delta\tilde{x}_i) = 0$. On the other hand for small distances to avoid collisions velocity difference has to be very important. One of function which has these properties is reverse sigmoid shape function. As we are using already one sigmoid function $\tilde{V}_{opt}(\Delta x_i) = \frac{(\Delta\tilde{x}_i)^2}{1+(\Delta\tilde{x}_i)^2}$, the reasonable choice for $f(\Delta\tilde{x}_i)$ seems to be

$$f(\Delta\tilde{x}_i) = 1 - \tilde{V}_{opt}(\Delta x_i) = \frac{1}{1+(\Delta\tilde{x}_i)^2} \ . \tag{3.19}$$

By inserting Eq. (3.19) into Eq. (3.18) we end up with model

$$\begin{cases} \dfrac{d\tilde{v}_i}{d\tilde{t}} = \dfrac{(\Delta\tilde{x}_i)^2}{1+(\Delta\tilde{x}_i)^2} - \tilde{v}_i + \beta\dfrac{1}{1+(\Delta\tilde{x}_i)^2}\Delta\tilde{v}_i \\ \dfrac{d\tilde{x}_i}{d\tilde{t}} = \dfrac{1}{\alpha}\tilde{v}_i \end{cases} , \tag{3.20}$$

which further will be called as our model. This corresponds to dimension form equation

$$\begin{cases} \dfrac{dv_i}{dt} = \dfrac{1}{\tau}\left(\dfrac{(\Delta x_i)^2}{D^2+(\Delta x_i)^2} - v_i\right) + \lambda\dfrac{1}{D^2+(\Delta x_i)^2}\Delta v_i \\ \dfrac{dx_i}{dt} = v_i \end{cases} . \tag{3.21}$$

Our model in dimensionless form depends only on 4 parameters α, β and from initial and boundary condition N, $\tilde{L}$. This is one more then for OVM, but our model contains explicit dependence on velocity difference. As we can see that this is generalization of OVM, because by setting $\beta = 0$ we have OVM.

3.5. Linear stability analysis

Let us write our model in more generalized form with arbitrary optimal velocity function and general $f(\Delta\tilde{x}_i)$

$$\begin{cases} \dfrac{d\tilde{v}_i}{d\tilde{t}} = V_{opt}(\Delta\tilde{x}_i) - \tilde{v}_i + \beta f(\Delta\tilde{x}_i)\Delta\tilde{v}_i \\ \dfrac{d\tilde{x}_i}{d\tilde{t}} = \dfrac{1}{\alpha}\tilde{v}_i \end{cases} . \tag{3.22}$$

Eq. (3.22) has homogeneous solution $(\tilde{x}_i^h(\tilde{t}), \tilde{v}_i^h(\tilde{t}))$

$$\begin{aligned} \tilde{x}_i^h(\tilde{t}) &= x_0 + i \cdot \tilde{b} + V_{opt}(\tilde{b})\tilde{t} \\ \tilde{v}_i^h(\tilde{t}) &= V_{opt}(\tilde{b}) \ , \end{aligned} \tag{3.23}$$

where $\tilde{b} = \tilde{L}/N$ is distance between cars and x_0 is position of first car at $t = 0$.

To preform linear stability analysis lets first linearize Eq. (3.22) around $(\tilde{x}_i^h(\tilde{t}), \tilde{v}_i^h(\tilde{t}))$

$$\begin{aligned} \frac{d\tilde{v}_i}{d\tilde{t}} &= V'_{opt}(\tilde{b})\Delta\tilde{x}_i - \tilde{v}_i + \beta f(\tilde{b})\Delta\tilde{v}_i \\ \frac{d\tilde{x}_i}{d\tilde{t}} &= \frac{1}{\alpha}\tilde{v}_i \ , \end{aligned} \tag{3.24}$$

where $V'_{opt}(\tilde{b}) = \frac{d}{d\Delta\tilde{x}} V_{opt}(\Delta\tilde{x})\big|_{\Delta\tilde{x}=\tilde{b}}$.

Lets assume that small perturbation $(\tilde{\xi}(\tilde{t}), \tilde{\eta}(\tilde{t}))$ is added to homogeneous solution Eq. (3.23)

$$\begin{aligned} \tilde{x}_i^h(\tilde{t}) &= x_0 + i \cdot \tilde{b} + V_{opt}(\tilde{b})\tilde{t} + \tilde{\xi}(\tilde{t}) \\ \tilde{v}_i^h(\tilde{t}) &= V_{opt}(\tilde{b}) + \tilde{\eta}(\tilde{t}) \ . \end{aligned} \tag{3.25}$$

By inserting Eq. (3.25) into Eq. (3.24) we get equation for perturbations

$$\begin{aligned} \frac{d\tilde{v}_i}{d\tilde{t}} &= V'_{opt}(\tilde{b})\left(\tilde{\xi}_{i+1} - \tilde{\xi}_i\right) - \tilde{v}_i + \beta f(\tilde{b})\left(\tilde{\eta}_{i+1} - \tilde{\eta}_i\right) \\ \frac{d\tilde{\xi}_i}{d\tilde{t}} &= \frac{1}{\alpha}\tilde{\eta}_i \ . \end{aligned} \tag{3.26}$$

Using vector notations $\tilde{\boldsymbol{\xi}} = \left(\tilde{\xi}_1, \tilde{\xi}_2, \cdots, \tilde{\xi}_N\right)^T$, $\tilde{\boldsymbol{\eta}} = \left(\tilde{\eta}_1, \tilde{\eta}_2, \cdots, \tilde{\eta}_N\right)^T$ Eq. (3.26) can be written in matrix form

$$\begin{pmatrix} \frac{d}{d\tilde{t}}\tilde{\boldsymbol{\xi}} \\ \frac{d}{d\tilde{t}}\tilde{\boldsymbol{\eta}} \end{pmatrix} = \begin{pmatrix} 0\boldsymbol{I} & \frac{1}{\alpha}\boldsymbol{I} \\ \boldsymbol{A} & \boldsymbol{B} \end{pmatrix} \begin{pmatrix} \tilde{\boldsymbol{\xi}} \\ \tilde{\boldsymbol{\eta}} \end{pmatrix} = \boldsymbol{M} \begin{pmatrix} \tilde{\boldsymbol{\xi}} \\ \tilde{\boldsymbol{\eta}} \end{pmatrix} \ , \tag{3.27}$$

where $\boldsymbol{I}$ is $N \times N$ identity matrix and $\boldsymbol{A}$ and $\boldsymbol{B}$ are following $N \times N$ matrices

$$\boldsymbol{A} = \begin{pmatrix} -V'_{opt}(\tilde{b}) & V'_{opt}(\tilde{b}) & 0 & \dots & 0 \\ 0 & -V'_{opt}(\tilde{b}) & V'_{opt}(\tilde{b}) & \ddots & \vdots \\ \vdots & \ddots & \ddots & \ddots & 0 \\ 0 & \ddots & 0 & -V'_{opt}(\tilde{b}) & V'_{opt}(\tilde{b}) \\ V'_{opt}(\tilde{b}) & 0 & \dots & 0 & -V'_{opt}(\tilde{b}) \end{pmatrix} , \tag{3.28}$$

$$\boldsymbol{B} = \begin{pmatrix} -1-\beta f(\tilde{b}) & \beta f(\tilde{b}) & 0 & \dots & 0 \\ 0 & -1-\beta f(\tilde{b})(\tilde{b}) & \beta f(\tilde{b}) & \ddots & \vdots \\ \vdots & \ddots & \ddots & \ddots & 0 \\ 0 & \ddots & 0 & -1-\beta f(\tilde{b}) & \beta f(\tilde{b}) \\ \beta f(\tilde{b}) & 0 & \dots & 0 & -1-\beta f(\tilde{b}) \end{pmatrix} . \tag{3.29}$$

The conditions for eigenvalues λ of Eq. (3.27) reads as $\det(\boldsymbol{M} - \lambda \boldsymbol{I}) = 0$, which simplifies to

$$\det(\boldsymbol{M} - \lambda \boldsymbol{I}) = \det \begin{pmatrix} -\lambda \boldsymbol{I} & \frac{1}{\alpha}\boldsymbol{I} \\ \boldsymbol{A} & \boldsymbol{B} - \lambda \boldsymbol{I} \end{pmatrix} = \det \left(\lambda^2 \boldsymbol{I} - \lambda \boldsymbol{B} - \frac{1}{\alpha}\boldsymbol{A} \right) = \det(\boldsymbol{C}) \ , \tag{3.30}$$

where $\boldsymbol{C}$ is $N \times N$ matrix

$$\boldsymbol{C} = \begin{pmatrix} c & -d & 0 & \dots & 0 \\ 0 & c & -d & \ddots & \vdots \\ \vdots & \ddots & \ddots & \ddots & 0 \\ 0 & \ddots & 0 & c & -d \\ -d & 0 & \dots & 0 & c \end{pmatrix} , \tag{3.31}$$

with $c = \lambda^2 + \lambda + \lambda\beta f(\tilde{b}) + \frac{1}{\alpha}V'_{opt}(\tilde{b})$ and $d = \lambda\beta f(\tilde{b}) + \frac{1}{\alpha}V'_{opt}(\tilde{b})$. Note that in derivation of Eq. (3.30) $N \times N$ block matrix property

$$\text{if} \quad \boldsymbol{AB} = \boldsymbol{BA} \quad \Rightarrow \quad \det \begin{pmatrix} \boldsymbol{A} & \boldsymbol{B} \\ \boldsymbol{C} & \boldsymbol{D} \end{pmatrix} = \det(\boldsymbol{DA} - \boldsymbol{CB}) \tag{3.32}$$

was used. The determinant of matrix $\boldsymbol{C}$ can be simply calculated recursively using Laplace's

formula which leads to result

$$\det\left(\boldsymbol{C}\right) = c^N - d^N = 0. \tag{3.33}$$

So equation for eigenvalue reads as

$$\lambda^2 + \lambda + \lambda\beta f(\tilde{b}) + \frac{1}{\alpha}V'_{opt}(\tilde{b}) = \left[\lambda\beta f(\tilde{b}) + \frac{1}{\alpha}V'_{opt}(\tilde{b})\right]\left(\cos\frac{2\pi m}{N} + i\sin\frac{2\pi m}{N}\right) , \tag{3.34}$$

where m is an integer $m \in [1; N]$. By splitting λ in real μ and imaginary ω parts $\lambda = \mu + i\omega$, inserting into Eq. (3.34) and separating real and imaginary parts, one obtains

$$\begin{aligned} \mu^2 - \omega^2 + \mu\left(1 + \beta f(\tilde{b})\right) + \frac{1}{\alpha} &= \left(\mu\beta f(\tilde{b}) + \frac{1}{\alpha}V'_{opt}(\tilde{b})\right)\cos\frac{2\pi m}{N} - \omega\beta f(\tilde{b})\sin\frac{2\pi m}{N} \\ \omega\left(2\mu + 1 + \beta f(\tilde{b})\right) &= \left(\mu\beta f(\tilde{b}) + \frac{1}{\alpha}V'_{opt}(\tilde{b})\right)\sin\frac{2\pi m}{N} + \omega\beta f(\tilde{b})\cos\frac{2\pi m}{N} . \end{aligned} \tag{3.35}$$

The homogeneous solutions is unstable when $\mu > 0$. To find bifurcation point we have to set $\mu = 0$ in Eq. (3.35)

$$\omega^2 = \frac{1}{\alpha}V'_{opt}(\tilde{b})\left(1 - \cos\frac{2\pi m}{N}\right) - \omega\beta f(\tilde{b})\sin\frac{2\pi m}{N} \tag{3.36}$$

$$\omega\left(1 + \beta f(\tilde{b})\left(1 - \cos\frac{2\pi m}{N}\right)\right) = \frac{1}{\alpha}V'_{opt}(\tilde{b})\sin\frac{2\pi m}{N} . \tag{3.37}$$

By inserting Eq. (3.37) into Eq. (3.36) we finally obtain stability criteria for m-th mode

$$\frac{1}{\alpha}V'_{opt}(\tilde{b}) = \beta f(\tilde{b}) + \frac{\left(1 + \beta f(\tilde{b})\left(1 - \cos\frac{2\pi m}{N}\right)\right)^2}{1 + \cos\frac{2\pi m}{N}} . \tag{3.38}$$

The homogeneous solution is unstable when it is unstable at least for one value of m, and as homogeneous solution becomes first unstable for $m = 1$

$$\frac{1}{\alpha}V'_{opt}(\tilde{b}) = \beta f(\tilde{b}) + \frac{\left(1 + \beta f(\tilde{b})\left(1 - \cos\frac{2\pi}{N}\right)\right)^2}{1 + \cos\frac{2\pi}{N}} > \beta f(\tilde{b}) + \frac{1}{1 + \cos\frac{2\pi}{N}} > \beta f(\tilde{b}) + \frac{1}{2} , \tag{3.39}$$

$$V'_{opt}(\tilde{b}) > \frac{\alpha}{2} + \alpha\beta f(\tilde{b}) . \tag{3.40}$$

When $\beta = 0$, Eq. (3.40) is consistent with results for OVM by Bando et al. [4]. When $f(\tilde{b}) = 1$, Eq. (3.40) is consistent with results for FVDM by Yu et al. [28].

By inserting in Eq. (3.40) functions of our model $V_{opt}(\tilde{b}) = \frac{\tilde{b}^2}{1+\tilde{b}^2}$, $f(\tilde{b}) = \frac{1}{1+\tilde{b}^2}$, we obtain that

homogeneous solution becomes unstable if

$$F\left(\tilde{b},\beta\right)=\frac{4\tilde{b}}{\left(1+\tilde{b}^2\right)\left(1+\tilde{b}^2+2\beta\right)}>\alpha\ . \tag{3.41}$$

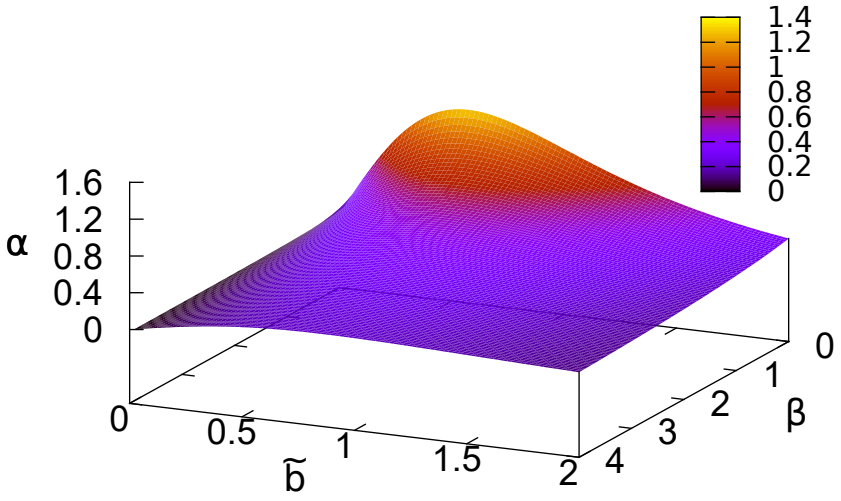

Figure 3.2.: Stability of the homogeneous solution for our model. Under the curve homogeneous solution is unstable.

For fixed value of β, $F\left(\tilde{b},\beta\right)$ has maximum at point

$$\tilde{b}_{max}=\frac{1}{\sqrt{3}}\sqrt{\sqrt{\beta^2+8\beta+4}-\beta-1}\ , \tag{3.42}$$

So for $\alpha > F(\tilde{b}_{max},\beta)$ homogeneous solution is stable for all values $\tilde{b}$ and for $\alpha < F(\tilde{b}_{max},\beta)$ there exist range of $\tilde{b}$ where homogeneous solution is unstable (see Fig. 3.3).

As we can see from Fig. 3.3, by increasing value of β we reduce maximal value of α for which homogeneous solution is unstable. This seems to make this model less attractive than OVM, but we also lover minimal value of α for which model starting from reasonable initial conditions is collision-free (see Sec. 3.6) and we can make simulations.

3.6. Collision test

As mentioned before OVM is not collision free one. For $\alpha < 0.9$ it is not possible to make any simulations at all due to collisions. Collisions happens when fast moving following car

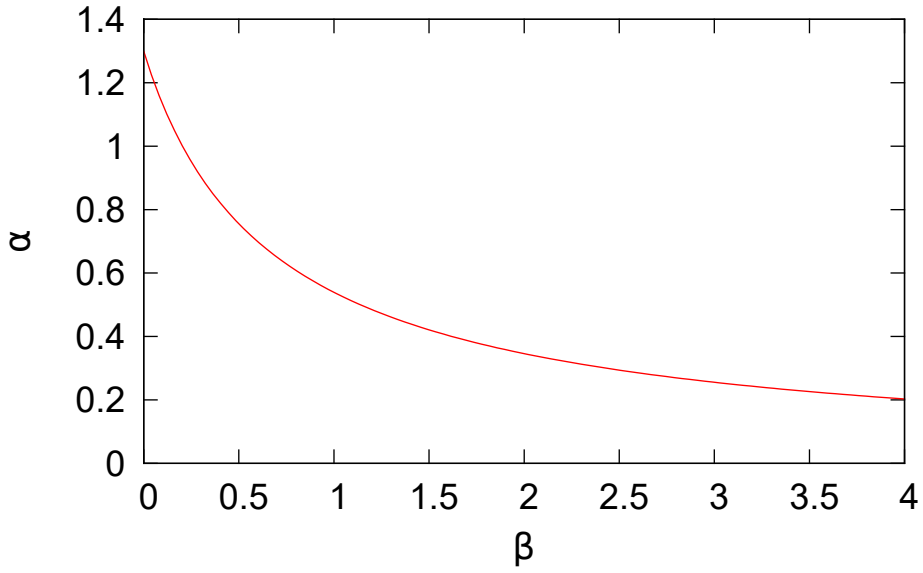

Figure 3.3.: Stability of the homogeneous solution for our model. For parameter values α , β which lie nuder the curve there exist critical density when homogeneous solution becomes unstable.

crash into slowly moving leader car. This happens because cars start to break too late or brake with too small deceleration. As OVM is special case of our model, clearly our model has the same problems. Such collisions should not happen in good model, so it is necessary to find out parameter range for which model is free of collisions.

The good test for this is vehicle and wall (standing leader vehicle). For wall located at $x = 0$ Eq. (3.20) for vehicle and wall simplifies to

$$\begin{cases} \dfrac{d\tilde{v}}{d\tilde{t}} = \dfrac{\tilde{x}^2}{1+\tilde{x}^2} - \tilde{v} - \beta \dfrac{1}{1+\tilde{x}^2}\tilde{v} \\ \dfrac{d\tilde{x}}{d\tilde{t}} = \dfrac{1}{\alpha}\tilde{v} \end{cases} . \tag{3.43}$$

To exclude collisions starting from initial conditions $\tilde{x}(\tilde{t}=0) = \tilde{x}_s$, $\tilde{v}(\tilde{t}=0) = 0$ the solution of Eq. (3.43) should be bounded only to negative values of $\tilde{x}$ ($\lim_{t\to\infty} \tilde{x}(\tilde{t}) < 0$) for any value of $\tilde{x}_s < 0$. Unfortunately it is not possible to solve Eq. (3.43) analytically and it has to be solved numerically. For numerical investigation we chose $x_c = -1000$ and as indicator whether collision happened sign of $\tilde{x}(\tilde{t} = 100000)$ was used (collision happened if $\tilde{x}(\tilde{t} = 100000) > 0$). Numerical results can bee seen in Fig. 3.4. From collision test we see that for reasonable value of $\beta > 0$ we actually have larger range for α then for OVM for which model is collision free and the same time phase transitions can be observed.

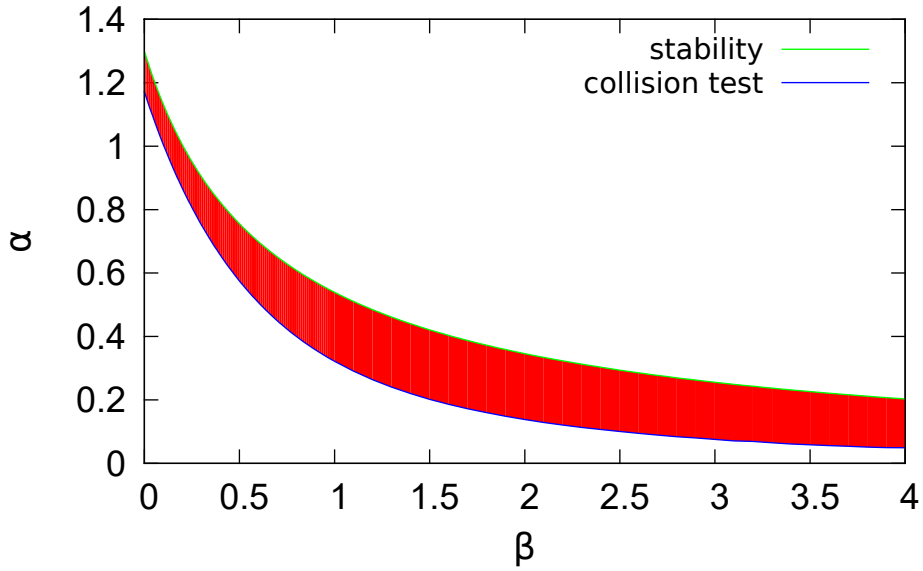

Figure 3.4.: Numerical results of vehicle and wall test. Blue line represents minimal value of α depending on value of β for which vehicle did not crash into the wall (Eq. (3.43)). Green line shows maximal value of α depending on value of of β for which we can still observe phase transitions. Red area represents parameter range for which model is collision free and we can observe phase transitions.

3.7. Fundamental diagrams

To plot fundamental diagram of our model we have to find steady states solutions of Eq. (3.20) with N cars on circular road with length $\tilde{L}$. Then using Eq. (3.44) we can simply plot them.

$$\tilde{\rho} = \frac{N}{\tilde{L}} \; ; \quad \tilde{j} = \tilde{\rho}\,\langle \tilde{v} \rangle \; ; \quad \langle \tilde{v} \rangle = \frac{1}{N} \sum_{i=1}^{N} \tilde{v}_i \tag{3.44}$$

But for $N > 2$ it is not possible to solve this problem analytically so we have to solve it numerically. The simplest way is to search for long time solutions of Eq. (3.20) starting with some initial conditions. The numerical solutions with Runge-Kutta 4-th order method for fixed N and different values of $\tilde{L}$ with parameter values $\alpha = 0.5$ and $\beta = 0.8$ can be seen in Fig. 3.5.

Fundamental diagram of our model (see Fig. 3.5) shows hysteresis. Starting from point S ($\tilde{\rho}_S = 0$) and increasing density, flux increases and homogeneous solution is stable. At point B homogeneous solution becomes unstable and long time solution is heterogeneous solution with one cluster. By further increasing density, flux decreases linearly until point D is reached. At point D heterogeneous solution becomes unstable and we observe transition back to homoge-

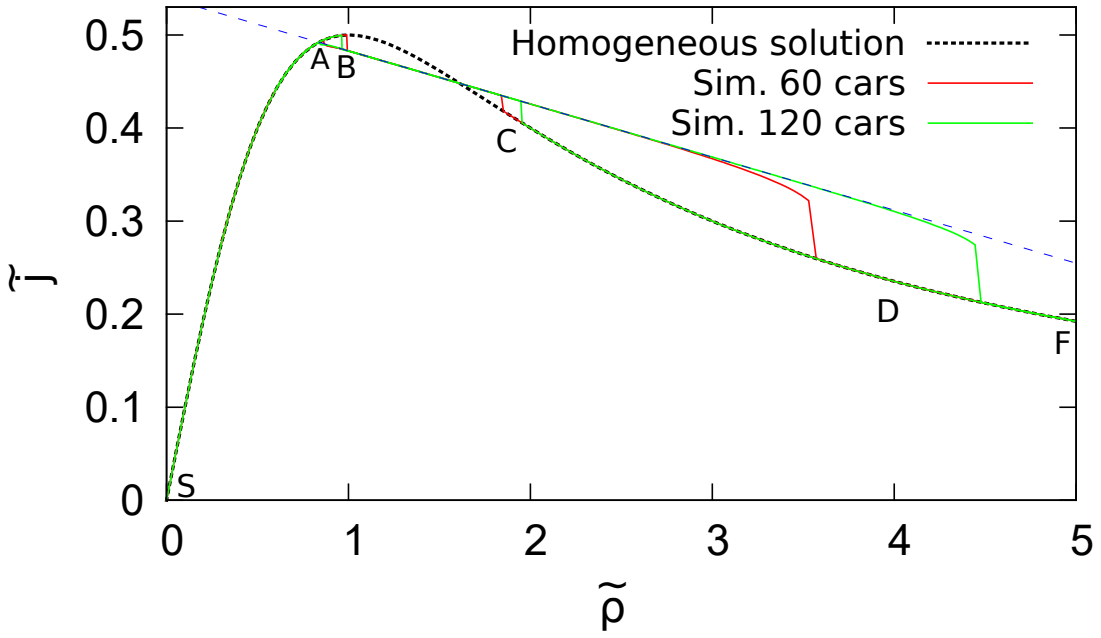

Figure 3.5.: Fundamental diagram of our model with $\alpha = 0.5$ and $\beta = 0.8$. Density was changed by changing $\tilde{L}$ and keeping N constant. Dotted black line represents homogeneous solution, solid red line represents results for simulation with 60 cars, solid green line represents results for simulation with 120 cars, dashed blue line is linear fit and should represent heterogeneous solution for limit case $N, \tilde{L} \to \infty$.

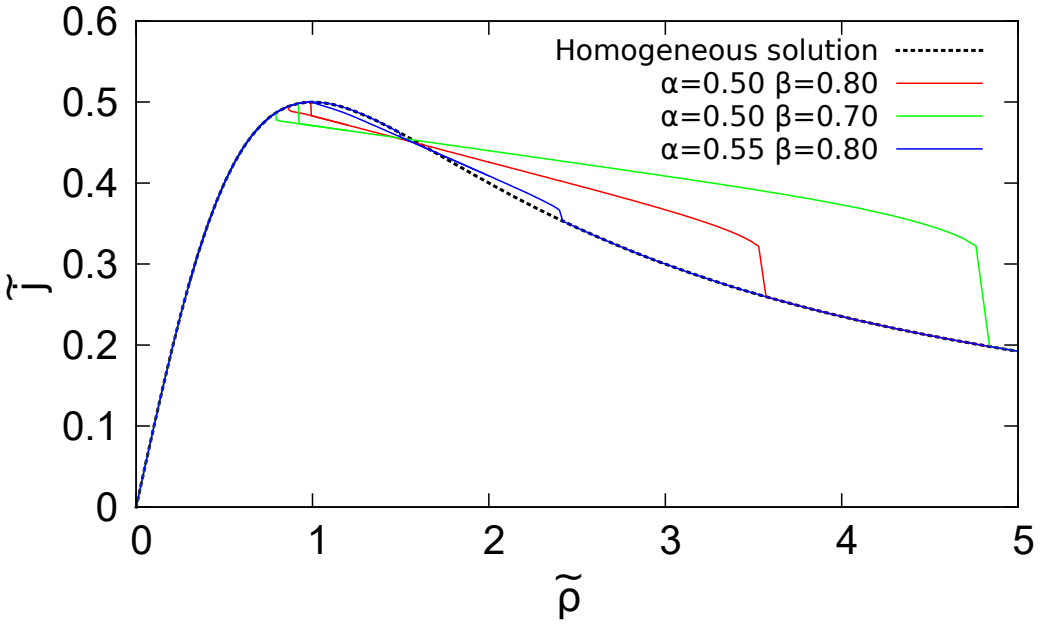

Figure 3.6.: Fundamental diagram of our model with $N = 60$ for different parameter values α and β. Density was changed by changing $\tilde{L}$ and keeping N constant.

neous solution. Starting from point F and decreasing density, flux increases and homogeneous solution is stable. At point C homogeneous solution becomes unstable and we observe transition to heterogeneous solution with one cluster. At point A heterogeneous solution becomes unstable and we observe transition back to homogeneous solution. Note that if point D is further then F ($\tilde{\rho}_F < \tilde{\rho}_D$ like in Fig. 3.6) we have reverse λ-shaped fundamental diagram which is observed empirical traffic data (see Sec. 2.5.3).

From Fig. 3.5 we see that position of points A, B, C, D depends on N. This is due to finite size effect (only integer numbers of cars can be in the cluster). For limit case $N, \tilde{L} \to \infty$ positions of points A and D can be found from linear linear fit (dashed blue line in Fig. 3.5) and points B and C are solutions of Eq. (3.41). Note that also for finite N position of points B and C well match with results obtained from Eq. (3.39)).

By changing parameter values of α and β fundamental diagram slightly changes (see Fig. 3.6), but in limit case $N, \tilde{L} \to \infty$ still remains reverse λ-shaped fundamental diagram (see Fig. 3.7).

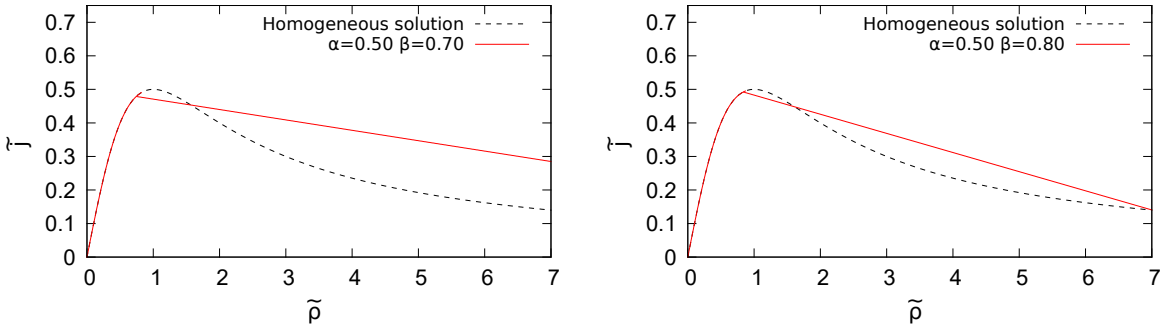

Figure 3.7.: Fundamental diagram of our model with parameter values $\alpha = 0.50$, $\beta = 0.70$ and $\alpha = 0.50$, $\beta = 0.80$ for limit case $N, \tilde{L} \to \infty$.

If we now compare fundamental diagrams for limit case $N, \tilde{L} \to \infty$ (Fig. 3.7) with results from NGSIM I-80 data set (Fig. 2.20) we see that they are quite similar. The parts between points S and A, A and B (for point names see Fig. 3.5) for I-80 data set seems to be more linear then for our model. And part between points A and B where homogeneous solution is still stable is larger for I-80 data set.

3.8. Field data

When long-time solution of our model is homogeneous one, then $\tilde{g} = \tilde{b}$, $\tilde{v} = \tilde{V}_{opt}\tilde{b}$, $\Delta\tilde{v} = 0$, $\tilde{a} = 0$ and this gives only one point in field data plots. When long-time solution is heterogeneous

one, the situation is more complex and field data are limit cycles (see Fig. 3.8).

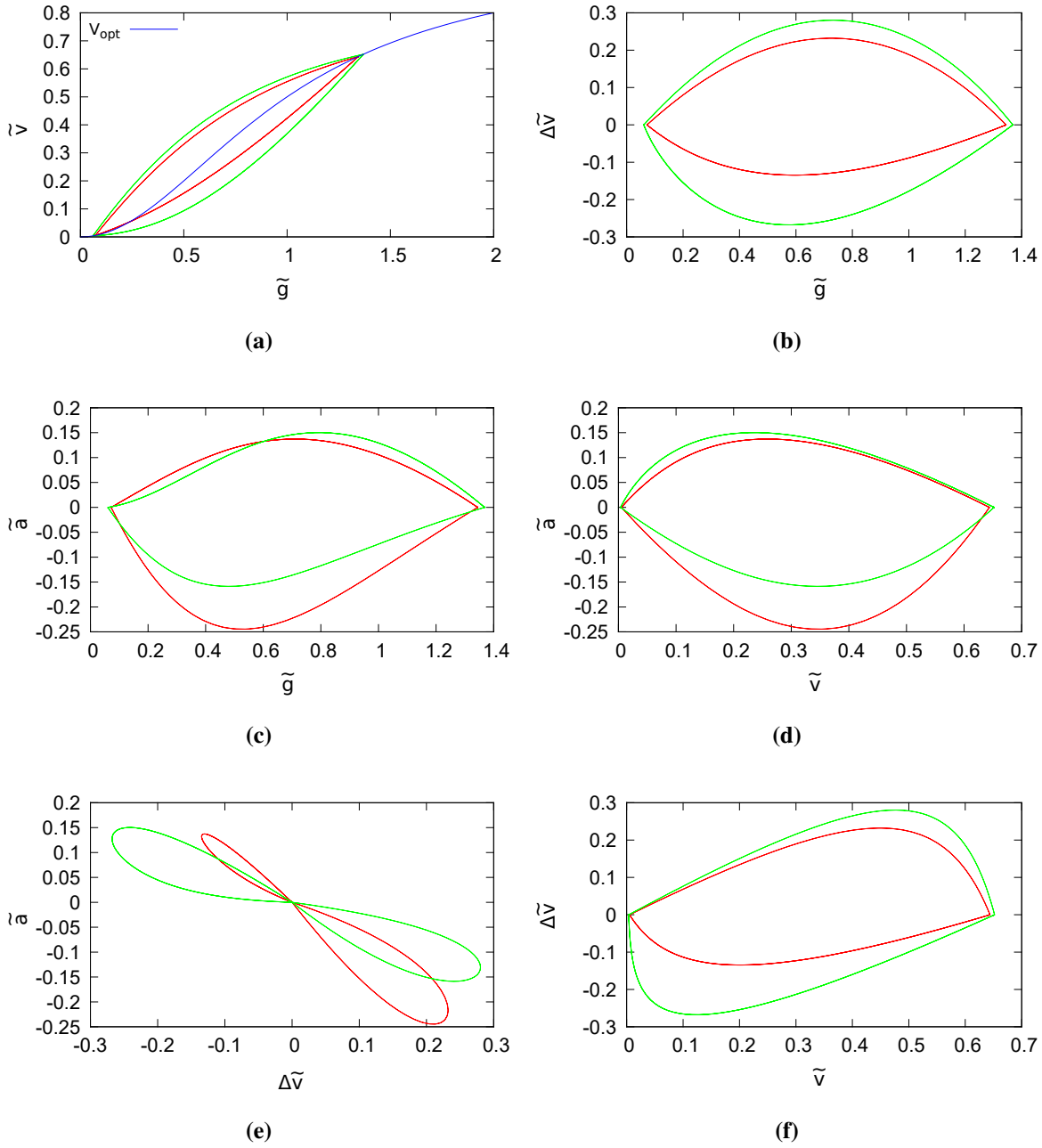

Figure 3.8.: Field data of our model with $\alpha = 0.5$, $\beta = 0.7$ (red line) comparison with OVM with $\alpha = 0.94$ (green line) for $\tilde{\rho} = 2$.

As we can form Fig. 3.8 our model for $\beta > 0$ produces more asymmetrical field data than OVM. If we now compare with field data (Fig. 2.21) and vector data (Fig. 2.28) of I-80 data set we see notable differences. The reason for that are both the model itself and the simplified traffic situation. The differences could be reduced by adding stochasticity to our model which as we can see from I-80 data sets plays large role, however, it is quit difficult, because due to lane changes it is not just withe noise.

4. The model of Martin Hilliges and Wolfgang Weidlich

4.1. Introduction

Usually microscopic models give better agreement with empirical data than fluid dynamical models [27], because they better describe forward oriented property of traffic. Forward oriented here imply that model must be asymmetrical and third law of Newton is invalid. As it is quite difficult to build in asymmetry in fluid dynamical models mostly all fluid dynamical models are symmetric (third law of Newton is valid).

One interesting asymmetric fluid dynamical model is that by Martin Hilliges and Wolfgang Weidlich from University of Stuttgart published in 1995 [14]. This model uses forward oriented flux definition and the velocity relaxation as microscopic optimal velocity model. The disadvantage is that this is quasi-discrete model (all road segment is divided into cells and in each cell density and velocity is constant).

Also it was already published in 1995, since then this model was not analyzed in details and original paper uses only very simple, unrealistic optimal velocity functions and does not provide any analysis of stationary moving profiles. Due to this reasons it was decided to revisit model by Martin Hilliges and Wolfgang Weidlich. For model analysis periodic boundary conditions and optimal velocity function proposed by Mahnke et al. [20] was chosen. The main analysis was concentrated on traffic jam formation and shape.

4.2. Model formulation

Consider a road segment with length L, which is divided it into N cells with size Δx such that $L = N\Delta x$. In each cell it is assumed that density ρ_i and velocity v_i is constant (see Fig. 4.1).

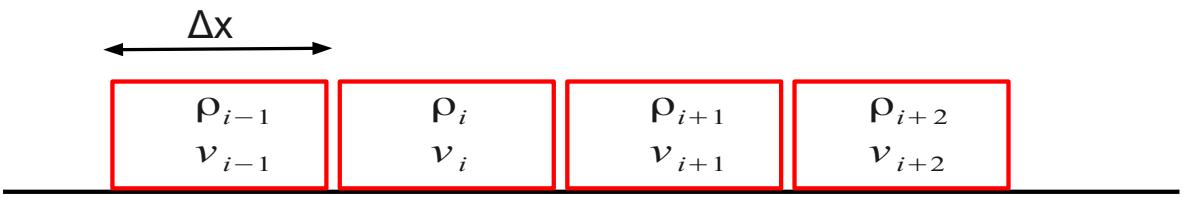

Figure 4.1.: Road segment with length L divided into cells with length Δx

Density in cell i can change only because of inflow from cell $i-1$ and outflow to cell $i+1$. As traffic is forward oriented inflow flux from cell $i-1$ to cell i is defined as $j_i^{in} = \rho_{i-1} v_i$ and outflow flux from cell i to cell $i+1$ is $j_i^{out} = \rho_i v_{i+1}$. Note that this differs from usual inflow and outflow flux definitions and clearly shows forward oriented thinking of drivers, but of course in the limit case $\Delta x \to 0$ it gives the same results as usual definition. Now we can write flux conservation equation

$$\frac{\partial \rho_i}{\partial t} \Delta x = j_i^{in} - j_i^{out} = \rho_{i-1} v_i - \rho_i v_{i+1} \,. \tag{4.1}$$

If we expand density and velocity in Taylor series up to second order at i cell

$$\begin{aligned} \rho_{i-1} &= \rho_i - \Delta x \frac{\partial \rho_i}{\partial x} + \frac{(\Delta x)^2}{2} \frac{\partial^2 \rho_i}{\partial x^2} \\ v_{i+1} &= v_i + \Delta x \frac{\partial v_i}{\partial x} + \frac{(\Delta x)^2}{2} \frac{\partial^2 v_i}{\partial x^2} \end{aligned} \tag{4.2}$$

and insert into Eq. (4.1) we end up with

$$\frac{\partial \rho_i}{\partial t} + \frac{\partial}{\partial x} (\rho_i v_i) = \frac{\Delta x}{2} \frac{\partial}{\partial x} \left(\frac{\partial \rho_i}{\partial x} v_i - \frac{\partial v_i}{\partial x} \rho_i \right) \,. \tag{4.3}$$

As Eq. (4.3) contains only quantities which can be determined in cell i we can directly write continuous form of (4.3) by dropping indexes

$$\frac{\partial \rho}{\partial t} + \frac{\partial}{\partial x} (\rho v) = \frac{\Delta x}{2} \frac{\partial}{\partial x} \left(\frac{\partial \rho}{\partial x} v - \frac{\partial v}{\partial x} \rho \right) \,. \tag{4.4}$$

But we still need equation for velocity. For velocity the same relaxation ansatz as for optimal velocity model (see Sec. 3.3) is used:

$$\frac{Dv}{Dt} = \frac{1}{\tau} \left(V_{opt}(\rho) - v \right) \,, \tag{4.5}$$

where $\frac{D}{Dt} = \frac{\partial}{\partial t} + v\frac{\partial}{\partial x}$ is material derivative and V_{opt} is optimal velocity function.

We can finally write continuous form of vehicular traffic model by Hilliges and Weidlich as system of two coupled partial differential equations (PDEs)

$$\begin{aligned} \frac{\partial \rho}{\partial t} + \frac{\partial}{\partial x}(\rho v) &= \frac{\Delta x}{2}\frac{\partial}{\partial x}\left(\frac{\partial \rho}{\partial x}v - \frac{\partial v}{\partial x}\rho\right) \\ \frac{\partial v}{\partial t} + v\frac{\partial v}{\partial x} &= \frac{1}{\tau}\left(V_{opt}(\rho) - v\right) \ . \end{aligned} \tag{4.6}$$

Note that we have already defined two discretized versions of Eq. (4.6)

$$\begin{aligned} \frac{\partial \rho_i}{\partial t} + \frac{\partial}{\partial x}(\rho_i v_i) &= \frac{\Delta x}{2}\frac{\partial}{\partial x}\left(\frac{\partial \rho_i}{\partial x}v_i - \frac{\partial v_i}{\partial x}\rho_i\right) \\ \frac{\partial v_i}{\partial t} + v_i\frac{\partial v}{\partial x} &= \frac{1}{\tau}\left(V_{opt}(\rho_i) - v_i\right) \end{aligned} \tag{4.7}$$

and

$$\begin{aligned} \frac{\partial \rho_i}{\partial t}\Delta x &= \rho_{i-1}v_i - \rho_i v_{i+1} \\ \frac{\partial v_i}{\partial t} + v_i\frac{\partial v}{\partial x} &= \frac{1}{\tau}\left(V_{opt}(\rho_i) - v_i\right) \ , \end{aligned} \tag{4.8}$$

which have slightly different equation for density.

To compare results with microscopic models (see Chap. 3) for further investigate periodic boundary conditions (circular road) and optimal velocity function proposed by Mahnke et al. [20] was chosen

$$V_{opt}(\rho) = v_{max}\frac{1}{D^2\rho^2 + 1}. \tag{4.9}$$

By introducing dimensionless variables $\tilde{x} = \frac{x}{D}$, $\tilde{t} = \frac{t}{\tau}$, $\tilde{\rho} = \rho D$, $\tilde{v} = \frac{v}{v_{max}}$, $\Delta\tilde{x} = \frac{\Delta x}{D}$, $\tilde{L} = \frac{L}{D}$, $\alpha = \frac{D}{\tau v_{max}}$ we get dimensionless form of Eq. (4.6)

$$\begin{aligned} \frac{\partial \tilde{\rho}}{\partial \tilde{t}} &= -\frac{1}{\alpha}\frac{\partial}{\partial \tilde{x}}(\tilde{\rho}\tilde{v}) + \frac{1}{\alpha}\frac{\Delta\tilde{x}}{2}\frac{\partial}{\partial \tilde{x}}\left(\frac{\partial \tilde{\rho}}{\partial \tilde{x}}\tilde{v} - \frac{\partial \tilde{v}}{\partial \tilde{x}}\tilde{\rho}\right) \\ \frac{\partial \tilde{v}}{\partial \tilde{t}} &= -\frac{1}{\alpha}\tilde{v}\frac{\partial \tilde{v}}{\partial \tilde{x}} + \left(\frac{1}{\tilde{\rho}^2 + 1} - \tilde{v}\right) \ , \end{aligned} \tag{4.10}$$

for which we have only thee control parameters α, $\Delta\tilde{x}$, N.

4.3. Stability analysis

To see whether Eq. (4.10) can describe cluster formations on the road we have to check whether in some parameter range $\Delta\tilde{x}$ and α there is some critical $\tilde{\rho}_{crit}$ density at which homogeneous solution $\tilde{\rho}(\tilde{x},\tilde{t}) = \tilde{\rho}_h$ and $\tilde{v}(\tilde{x},\tilde{t}) = \tilde{v}_h$ becomes unstable. To find out this at least linear stability analysis of Eq. (4.10) has to be preformed.

To preform linear analysis first we have to linearize Eq. (4.10) around point $(\tilde{\rho}_h\,;\tilde{v}_h)$

$$\begin{aligned}\frac{\partial\tilde{\rho}}{\partial\tilde{t}} &= -\frac{1}{\alpha}\left(\tilde{\rho}_h\frac{\partial\tilde{v}}{\partial\tilde{x}} + \tilde{v}_h\frac{\partial\tilde{\rho}}{\partial\tilde{x}}\right) + \frac{1}{\alpha}\frac{\Delta\tilde{x}}{2}\left(\tilde{v}_h\frac{\partial^2\tilde{\rho}}{\partial\tilde{x}^2} - \tilde{\rho}_h\frac{\partial^2\tilde{v}}{\partial\tilde{x}^2}\right)\\ \frac{\partial\tilde{v}}{\partial\tilde{t}} &= -\frac{1}{\alpha}\tilde{v}_h\frac{\partial\tilde{v}}{\partial\tilde{x}} - \left(\tilde{\rho}\frac{2\tilde{\rho}_h}{\left(\tilde{\rho}_h^2+1\right)^2} + \tilde{v}\right)\ .\end{aligned} \tag{4.11}$$

Lets consider trajectory in neighborhood of stationary solution $(\tilde{\rho}_h\,;\tilde{v}_h)$

$$\begin{aligned}\tilde{\rho}(\tilde{x},\tilde{t}) &= \tilde{\rho}_h + \tilde{\eta}(\tilde{x},\tilde{t})\\ \tilde{v}(\tilde{x},\tilde{t}) &= \tilde{v}_h + \tilde{\zeta}(\tilde{x},\tilde{t})\ ,\end{aligned} \tag{4.12}$$

where $\tilde{\eta}(\tilde{x},\tilde{t})$ and $\tilde{\zeta}(\tilde{x},\tilde{t})$ are small space time dependent perturbations.

Inserting Eq. (4.12) into Eq. (4.11) we get equation for perturbations

$$\begin{aligned}\frac{\partial\tilde{\eta}}{\partial\tilde{t}} &= -\frac{1}{\alpha}\left(\tilde{\rho}_h\frac{\partial\tilde{\zeta}}{\partial\tilde{x}} + \tilde{v}_h\frac{\partial\tilde{\eta}}{\partial\tilde{x}}\right) + \frac{1}{\alpha}\frac{\Delta\tilde{x}}{2}\left(\tilde{v}_h\frac{\partial^2\tilde{\rho}}{\partial\tilde{x}^2} - \tilde{\rho}_h\frac{\partial^2\tilde{\zeta}}{\partial\tilde{x}^2}\right)\\ \frac{\partial\tilde{\zeta}}{\partial\tilde{t}} &= -\frac{1}{\alpha}\tilde{v}_h\frac{\partial\tilde{\zeta}}{\partial\tilde{x}} - \left(\tilde{\eta}\frac{2\tilde{\rho}_h}{\left(\tilde{\rho}_h^2+1\right)^2} + \tilde{\zeta}\right)\ .\end{aligned} \tag{4.13}$$

Using the notation $\Psi = (\tilde{\eta}\,;\tilde{\zeta})^T$ one can write Eq. (4.13) in concise form

$$\frac{\partial}{\partial t}\Psi = \hat{L}\cdot\Psi\ , \tag{4.14}$$

with the linear operator

$$\hat{L} = \begin{pmatrix} -\frac{1}{\alpha}\tilde{v}_h\left(\partial_x - \frac{\Delta\tilde{x}}{2}\partial_x^2\right) & -\frac{1}{\alpha}\tilde{\rho}_h\left(\partial_x + \frac{\Delta\tilde{x}}{2}\partial_x^2\right)\\ -\frac{2\tilde{\rho}_h}{\left(\tilde{\rho}_h^2+1\right)^2} & -1 - \frac{1}{\alpha}\tilde{v}_h\partial_x \end{pmatrix}\ . \tag{4.15}$$

Plane wave ansatz for perturbations

$$\begin{aligned}\tilde{\eta}(\tilde{x},\tilde{t}) &= \tilde{\eta}_0 \cdot e^{ik\tilde{x}} \cdot e^{\lambda\tilde{t}} \\ \tilde{\zeta}(\tilde{x},\tilde{t}) &= \tilde{\zeta}_0 \cdot e^{ik\tilde{x}} \cdot e^{\lambda\tilde{t}}\end{aligned} \tag{4.16}$$

solves Eq (4.14) with values of k which satisfy boundary conditions. Inserting Eq. (4.16) into Eq. (4.14) one obtains

$$\hat{L} = \begin{pmatrix} -\frac{k}{\alpha}\tilde{v}_h\left(i+\frac{\Delta\tilde{x}}{2}k\right) & -\frac{k}{\alpha}\tilde{\rho}_h\left(i-\frac{\Delta\tilde{x}}{2}k\right) \\ -\frac{2\tilde{\rho}_h}{\left(\tilde{\rho}_h^2+1\right)^2} & -1-ik\frac{1}{\alpha}\tilde{v}_h \end{pmatrix} . \tag{4.17}$$

The condition for eigenvalues λ of Eq. (4.14) reads as $\det\left|\hat{L}-\lambda\hat{I}\right| = 0$, where $\hat{I} = \mathrm{diag}(1;1)$, or

$$\left[\frac{k}{\alpha}\tilde{v}_h\left(i+\frac{\Delta\tilde{x}}{2}k\right)+\lambda\right]\left(1+ik\frac{1}{\alpha}\tilde{v}_h+\lambda\right) - \frac{k}{\alpha}\frac{2\tilde{\rho}_h^2}{\left(\tilde{\rho}_h^2+1\right)^2}\left(i-\frac{\Delta\tilde{x}}{2}k\right) = 0 . \tag{4.18}$$

The solution of Eq. (4.18) is

$$\lambda^{\pm} = -\frac{1}{2}\left[1+\frac{\Delta\tilde{x}}{2\alpha}k^2\tilde{v}_h + i\frac{2k}{\alpha}\tilde{v}_h \pm \sqrt{\left(1-\frac{\Delta\tilde{x}}{2\alpha}k^2\tilde{v}_h\right)^2 + \frac{k}{\alpha}\frac{8\tilde{\rho}_h^2}{\left(\tilde{\rho}_h^2+1\right)^2}\left(i-\frac{\Delta\tilde{x}}{2}k\right)}\right] , \tag{4.19}$$

here for square root of complex number ($\sqrt{x+iy}$) principal value of square root is used

$$\sqrt{x+iy} = \frac{\sqrt{2}}{2}\left[\sqrt{\sqrt{x^2+y^2}+x} + i\,\mathrm{sgn}(y)\sqrt{\sqrt{x^2+y^2}-x}\right] . \tag{4.20}$$

Stationary homogeneous solution is unstable if $\Re\lambda^{\pm} > 0$. Clearly due to definition of principal value of square root of complex number, $\Re\lambda^{+} < 0$ (λ^{+} is solution with $+$ sign) and we have to analyze only $\lambda^{-}(k)$. Since Eq. (4.19) is 4-th order equation for k, $\Re\lambda^{-}(k) = 0$ can have maximal 4 different roots, but as $\Re\lambda^{-}(k) = \Re\lambda^{-}(-k)$, $k = 0$ is root of oder two and we can have maximum 3 different roots $k_{1,2} = 0$, $k_{3,4} = \pm k_0$. One can easy show, that

$$\lim_{k\to 0}\Re\lambda^{-}(k) = 0 \; ; \; \lim_{k\to\pm\infty}\Re\lambda^{-}(k) < 0 , \tag{4.21}$$

from which follows that roots $k_{3,4} \neq 0$ only exist if $\Re\lambda(k=\varepsilon) > 0$, where $|\varepsilon| \to 0$. So to understand whether homogeneous solution is stable it is enough to expand $\lambda^{-}(k)$ in Taylor

series around $k = 0$ up to first nonzero term for real part.

Expanding Eq. (4.19) in Taylor series up to second order we get

$$\lambda^{-}(k) = \frac{1}{\alpha}\left(\frac{2\tilde{\rho}_h^2}{\left(1+\tilde{\rho}_h^2\right)^2} - \tilde{v}_h\right) ik + \left[\frac{1}{\alpha^2}\frac{4\tilde{\rho}_h^4}{\left(1+\tilde{\rho}_h^2\right)^4} - \frac{\Delta\tilde{x}}{2\alpha}\left(\tilde{v}_h + \frac{2\tilde{\rho}_h^2}{\left(1+\tilde{\rho}_h^2\right)^2}\right)\right] k^2 + O(k^3)\,. \tag{4.22}$$

From Eq. (4.22) we see that stationary homogeneous solution becomes unstable if

$$\frac{1}{\alpha^2}\frac{4\tilde{\rho}_h^4}{\left(1+\tilde{\rho}_h^2\right)^4} - \frac{\Delta\tilde{x}}{2\alpha}\left(\tilde{v}_h + \frac{2\tilde{\rho}_h^2}{\left(1+\tilde{\rho}_h^2\right)^2}\right) > 0\,, \tag{4.23}$$

which by inserting $\tilde{v}_h = \frac{1}{\tilde{\rho}_h^2+1}$ (see Sec. 4.4.1) simplifies to

$$\alpha\Delta\tilde{x} < \frac{8\tilde{\rho}_h^4}{\left(1+3\tilde{\rho}_h^2\right)\left(1+\tilde{\rho}_h^2\right)^2}\,. \tag{4.24}$$

For simpler analysis lets define function

$$F(\tilde{\rho}_h^2) := \frac{8\tilde{\rho}_h^4}{\left(1+3\tilde{\rho}_h^2\right)\left(1+\tilde{\rho}_h^2\right)^2}\,. \tag{4.25}$$

By solving equation

$$\frac{d}{d\tilde{\rho}_h^2}F(\tilde{\rho}_h^2) = 0 \tag{4.26}$$

we find that $F(\tilde{\rho}_h^2)$ has maximal value at point $\tilde{\rho}_{cr}^2 = \frac{1}{2}\left(1+\frac{1}{3}\sqrt{33}\right) \approx 1.4574$ and

$$\max\left\{F(\tilde{\rho}_h^2)\right\} = F(\tilde{\rho}_{cr}^2) = \frac{16\left(3+\sqrt{33}\right)^2}{\left(5+\sqrt{33}\right)\left(9+\sqrt{33}\right)^2} \approx 0.52371. \tag{4.27}$$

So for $\alpha\Delta\tilde{x} > F(\tilde{\rho}_{cr}^2) \approx 0.52371$ stationary homogeneous solution is stable and for $\alpha\Delta\tilde{x} < F(\tilde{\rho}_{cr}^2)$ there is density range for which homogeneous solution is unstable (see Fig. 4.2).

The group velocity $\tilde{v}_g$ which determines propagation speed of perturbation can be calculated using

$$\tilde{v}_g(k) = \frac{d}{dk}\omega(k) = \frac{d}{dk}\operatorname{Im}\lambda(k)\,. \tag{4.28}$$

So sign of derivative of imaginary part of $\lambda^{-}(k)$ determines propagation direction of perturbation. If $\operatorname{Im}\frac{d\lambda^{-}(k)}{dk} < 0$ this means that perturbation propagates in the same directions as cars and $\operatorname{Im}\frac{d\lambda^{-}(k)}{dk} > 0$ means that in opposite direction (usual congestion propagation direction). For

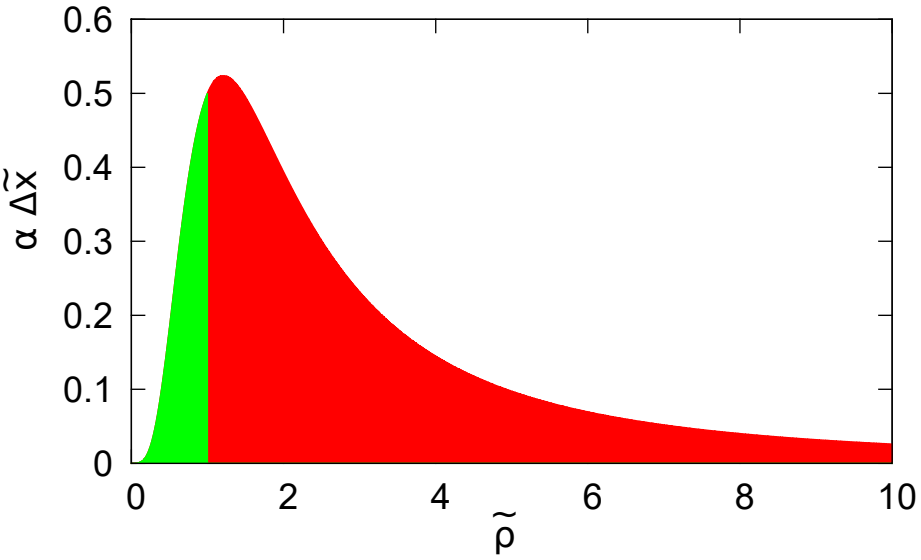

Figure 4.2.: Stability of stationary homogeneous solution. Filled region represents region where stationary homogeneous solution is unstable. Green means that perturbation propagates in the same direction as cars and reds means that perturbation propagates in opposite direction.

opposite propagation direction we have condition

$$\frac{1}{\alpha}\left(\frac{2\tilde{\rho}_h^2}{\left(1+\tilde{\rho}_h^2\right)^2}-\tilde{v}_h\right)>0\,, \tag{4.29}$$

which by inserting $\tilde{v}_h = \frac{1}{\tilde{\rho}_h^2+1}$ (see Sec. 4.4.1) simplifies to

$$\tilde{\rho}_h > 1\,. \tag{4.30}$$

Now we can summarize that for $\alpha\Delta\tilde{x} \in (F(\tilde{\rho}_{cr}^2) \approx 0.52371; \infty)$ stationary homogeneous solution is stable, for $\alpha\Delta\tilde{x} \in (0.5; F(\tilde{\rho}_{cr}^2) \approx 0.52371)$ stationary homogeneous solution is unstable and perturbations can propagate in opposite direction to direction of cars and for $\alpha\Delta\tilde{x} \in (0; 0.5)$ stationary homogeneous solution is unstable and perturbations can propagate in both directions depending on whether $\tilde{\rho}_h > 1$. As we can see by choosing parameter Δx we can adjust whether model describes only homogeneous flow or congested flow where perturbations propagate only in direction opposite to direction of cars or we have congested flow where for small densities ($\tilde{\rho}_h < 1$) congestions propagate in the same direction as cars and for large ($\tilde{\rho}_h > 1$) densities in opposite direction.

4.4. Stationary solution

To derive equation for stationary solutions of Eq. (4.10) we just have to so set $\frac{d\tilde{\rho}}{d\tilde{t}} = \frac{d\tilde{v}}{d\tilde{t}} = 0$

$$\begin{aligned} 0 &= -\frac{1}{\alpha}\frac{\partial}{\partial\tilde{x}}\left(\tilde{\rho}\tilde{v}\right) + \frac{1}{\alpha}\frac{\Delta\tilde{x}}{2}\frac{\partial}{\partial\tilde{x}}\left(\frac{\partial\tilde{\rho}}{\partial\tilde{x}}\tilde{v} - \frac{\partial\tilde{v}}{\partial\tilde{x}}\tilde{\rho}\right) \\ 0 &= -\frac{1}{\alpha}\tilde{v}\frac{\partial\tilde{v}}{\partial\tilde{x}} + \left(\frac{1}{\tilde{\rho}^2+1} - \tilde{v}\right) . \end{aligned} \tag{4.31}$$

We see that first equation of Eq. (4.31) can be straight forward integrated and by doing this we get

$$\tilde{\rho}\tilde{v} = \frac{\Delta\tilde{x}}{2}\left(\frac{\partial\tilde{\rho}}{\partial\tilde{x}}\tilde{v} - \frac{\partial\tilde{v}}{\partial\tilde{x}}\tilde{\rho}\right) + C\,, \tag{4.32}$$

where C is integration constant. As for homogeneous flow (see Sec. 4.4.1)

$$C = \tilde{\rho}_h\tilde{v}_h = \frac{\tilde{\rho}_h}{\tilde{\rho}_h^2+1} \leq \frac{1}{2}\,. \tag{4.33}$$

So equation for stationary solution is

$$\begin{aligned} \frac{\partial\tilde{\rho}}{\partial\tilde{x}} &= \frac{2}{\Delta\tilde{x}}\left(\tilde{\rho} - \frac{C}{\tilde{v}}\right) + \frac{\partial\tilde{v}}{\partial\tilde{x}}\frac{\tilde{\rho}}{\tilde{v}} \\ \frac{\partial\tilde{v}}{\partial\tilde{x}} &= \frac{\alpha}{\tilde{v}}\left(\frac{1}{\tilde{\rho}^2+1} - \tilde{v}\right) , \end{aligned} \tag{4.34}$$

which by rewriting in normal form becomes

$$\begin{aligned} \frac{\partial\tilde{\rho}}{\partial\tilde{x}} &= \frac{2}{\Delta\tilde{x}}\left(\tilde{\rho} - \frac{C}{\tilde{v}}\right) + \frac{\alpha\tilde{\rho}}{\tilde{v}^2}\left(\frac{1}{\tilde{\rho}^2+1} - \tilde{v}\right) \\ \frac{\partial\tilde{v}}{\partial\tilde{x}} &= \frac{\alpha}{\tilde{v}}\left(\frac{1}{\tilde{\rho}^2+1} - \tilde{v}\right) . \end{aligned} \tag{4.35}$$

Unfortunately it is not possible in general case to solve Eq. (4.35) analytically. One can solve analytically only for homogeneous velocity and density profiles and for case $\Delta\tilde{x} = 0$ (see Sec. A.1.1 in Appendix). However, as $\lim_{\Delta\tilde{x}\to 0+}$ and case $\Delta\tilde{x} = 0$ gives different results (for $\Delta\tilde{x} = 0$ one of two homogeneous solutions (with lower density) is always stable, where for $\lim_{\Delta\tilde{x}\to 0+}$ both homogeneous solutions are always unstable) it does not really tell much about systems properties.

It is possible to solve Eq. (4.35) numerically, however with periodical boundary conditions only homogeneous solution have some physical meaning.

4.4.1. Homogeneous solution

Eq. (4.35) of course has homogeneous solution. To get them we just have to set $\frac{\partial\tilde{\rho}}{\partial\tilde{x}} = \frac{\partial\tilde{v}}{\partial\tilde{x}} = 0$ and by inserting them in Eq. (4.35)

$$\begin{aligned} C &= \tilde{\rho}\tilde{v} \\ 0 &= \alpha\left(\frac{\tilde{v}}{C^2+\tilde{v}^2} - 1\right) , \end{aligned} \tag{4.36}$$

which has two solutions

$$f\begin{cases} \tilde{\rho} = \tilde{\rho}_h \\ \tilde{v} = \tilde{v}_h \end{cases} \quad \text{and} \quad \begin{cases} \tilde{\rho} = \dfrac{1}{\tilde{\rho}_h} \\ \tilde{v} = 1 - \tilde{v}_h \end{cases} , \tag{4.37}$$

where $\tilde{v}_h = \frac{1}{\tilde{\rho}^2+1}$.

4.5. Stationary moving profiles

As in traffic congestions moves, we are actually interested in stationary moving profiles (stationary solutions in some moving reference frame). To find stationary moving profiles which moves with group velocity $\tilde{v}_g$, we have to write equations in coordinate system which moves with speed $\tilde{v}_g$. Space coordinate $\tilde{\xi}$ in this coordinate system now is $\tilde{\xi} = \tilde{x} - \frac{1}{\alpha}\tilde{v}_g\tilde{t}$. The Eq. (4.10) in this coordinate system can be written as

$$\begin{aligned} \frac{\partial\tilde{\rho}}{\partial\tilde{t}} - \frac{1}{\alpha}\tilde{v}_g\frac{\partial\rho}{\partial\tilde{\xi}} &= -\frac{1}{\alpha}\frac{\partial}{\partial\tilde{\xi}}(\tilde{\rho}\tilde{v}) + \frac{1}{\alpha}\frac{\Delta\tilde{x}}{2}\frac{\partial}{\partial\tilde{\xi}}\left(\frac{\partial\tilde{\rho}}{\partial\tilde{x}}\tilde{v} - \frac{\partial\tilde{v}}{\partial\tilde{x}}\tilde{\rho}\right) \\ \frac{\partial\tilde{v}}{\partial\tilde{t}} - \frac{1}{\alpha}\tilde{v}_g\frac{\partial v}{\partial\tilde{\xi}} &= -\frac{1}{\alpha}\tilde{v}\frac{\partial\tilde{v}}{\partial\tilde{\xi}} + \left(\frac{1}{\tilde{\rho}^2+1} - \tilde{v}\right) \end{aligned} \tag{4.38}$$

and for stationary moving profiles we have condition

$$\frac{\partial\tilde{v}(\tilde{\xi},\tilde{t})}{\partial\tilde{t}} = \frac{\partial\tilde{\rho}(\tilde{\xi},\tilde{t})}{\partial\tilde{t}} = 0 . \tag{4.39}$$

So to find such profiles we have to solve

$$\begin{aligned}\frac{\partial\tilde{\rho}}{\partial\tilde{\xi}} &= \frac{2}{\Delta\tilde{x}}\left(\tilde{\rho}\left(1-\frac{\tilde{v}_g}{\tilde{v}}\right)-\frac{C_g}{\tilde{v}}\right)+\frac{\alpha\tilde{\rho}}{\tilde{v}(\tilde{v}-\tilde{v}_g)}\left(\frac{1}{\tilde{\rho}^2+1}-\tilde{v}\right)\\ \frac{\partial\tilde{v}}{\partial\tilde{\xi}} &= \frac{\alpha}{\tilde{v}-\tilde{v}_g}\left(\frac{1}{\tilde{\rho}^2+1}-\tilde{v}\right),\end{aligned} \tag{4.40}$$

where C_g is integration constant which physical meaning is flux in this moving reference frame and $C_g = \tilde{\rho}_h(\tilde{v}_h - \tilde{v}_g) = C - \tilde{\rho}_h\tilde{v}_g$ and now $-\tilde{\rho}_h\tilde{v}_g \leq C_g \leq 0.5 - \tilde{\rho}_h\tilde{v}_g$ and physical solution requires $0 \leq C_g \leq 0.5 - \tilde{\rho}_h\tilde{v}_g$ (see Sec. 4.5.1) .

4.5.1. Homogeneous solutions

In this case homogeneous solutions solutions can be found by solving

$$\begin{aligned}C_g &= \tilde{\rho}\,(\tilde{v}-\tilde{v}_g)\\ 0 &= \alpha\left(\frac{1}{\tilde{\rho}^2+1}-\tilde{v}\right).\end{aligned} \tag{4.41}$$

If we introduce dimensionless flux $\tilde{j} = \tilde{\rho}\tilde{v}$ which in this case is

$$\tilde{j}(\tilde{\rho}) = \frac{\tilde{\rho}}{\tilde{\rho}^2+1} \tag{4.42}$$

then Eq. (4.41) can be written as

$$\begin{aligned}C_g + \tilde{\rho}\tilde{v}_g &= \tilde{j}(\tilde{\rho})\\ \tilde{v} &= \frac{1}{\tilde{\rho}^2+1}.\end{aligned} \tag{4.43}$$

The Eq. (4.43) can be simply solved graphically and example with $C_g = 0.4$ and $\tilde{v}_g = -0.03$ can be found in Fig. 4.3 where the solutions are intersection points. Note that for negative values of $\tilde{v}_g$ C_g can be larger than 0.5. In general, as we can see from Fig. 4.3, for positive values of $\tilde{v}_g$ we can have up to 2 solutions, and for negative $\tilde{v}_g$ up to 3 solutions. Lets look to situation when $\tilde{\rho}_h = 1.4$ and $\tilde{v}_g = -0.079$. This case corresponds to $C \approx 0.473$ with $C_g \approx 0.584$. Graphical solutions of Eq. (4.43) can be seen in Fig. 4.4. As we can see in Fig. 4.4 we have 3 solutions $\tilde{\rho} \approx \{\tilde{\rho}_h = 1.4, 1.075, 4.80\}$. We also see that $\tilde{\rho} = \tilde{\rho}_h$ still is solution of stationary problem in moving reference frame and it can be showed that this is valid for every velocity $\tilde{v}_g$ and every density $\tilde{\rho}_h$. For larger but still negative v_g we can have also solutions with $\tilde{\rho} < 1$

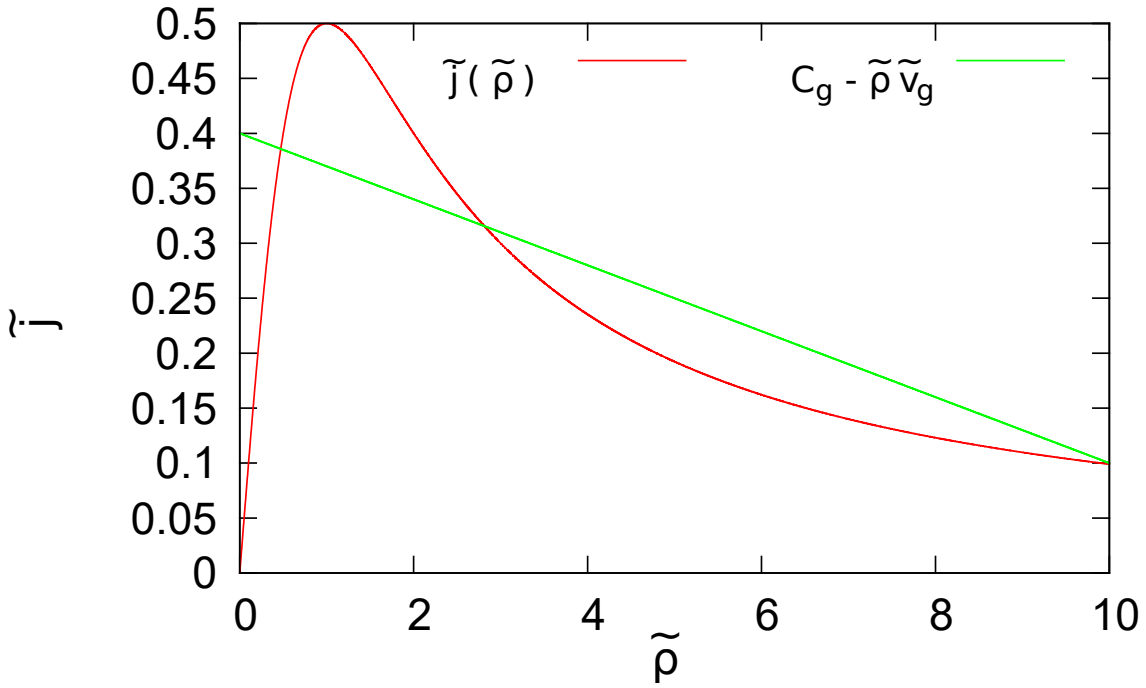

Figure 4.3.: Graphical solution of Eq. (4.43) with $C_g = 0.4$ and $\tilde{v}_g = -0.03$. Solutions are at crossings of lines.

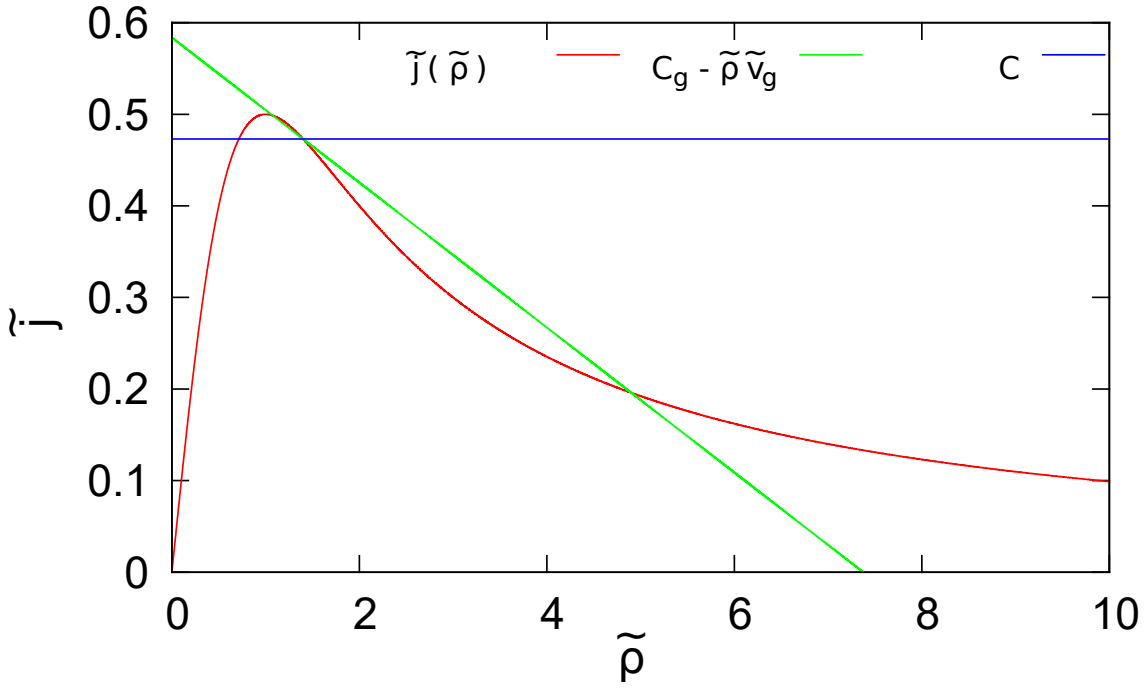

Figure 4.4.: Graphical solution of Eq. (4.43) for $C \approx 0.473$ and $\tilde{v}_g = -0.079$. Solutions are at crossings of lines.

for which small perturbations propagate actually with positive value of $\tilde{v}_g$. However numerical simulations (see Sec. 4.6) shows that large perturbations also for $\tilde{\rho} < 1$ propagate with negative speed. This shows that linear perturbation analysis is insufficient. The other physical condition which have to be satisfied is that $\tilde{v}_h > \tilde{v}_g$, because traffic is forward orientated and congestion can not propagate with larger speed than cars are driving with. Mathematically this is equivalent to

$$C_g \geq 0 \Leftrightarrow \tilde{v}_g \leq \frac{C}{\rho} \,. \tag{4.44}$$

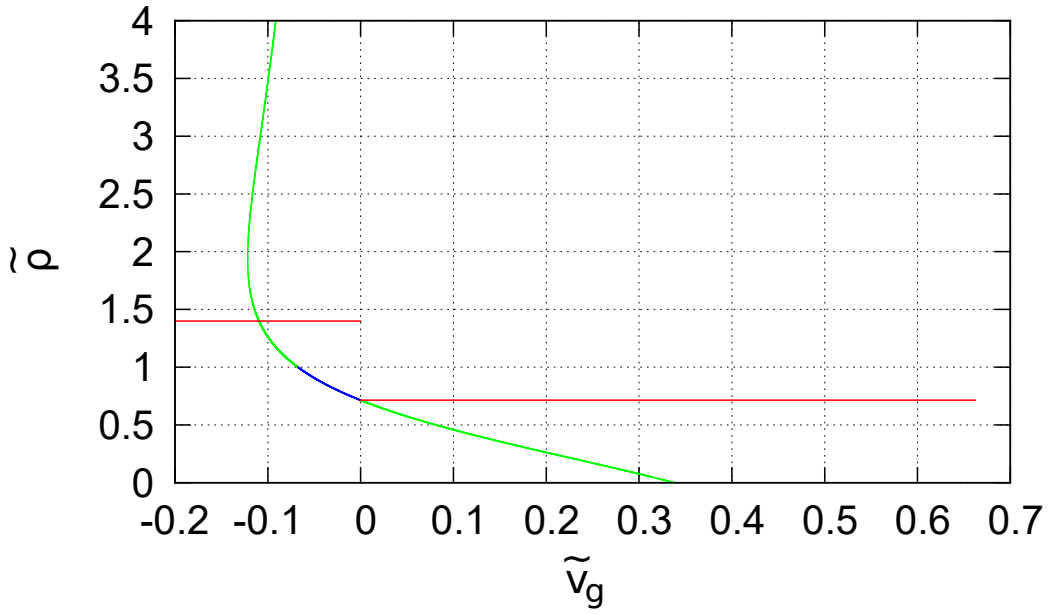

Figure 4.5.: Valid solution of Eq. (4.43) as function of $\tilde{v}_g$ for $C \approx 0.473$. Red line shows stationary homogeneous solution, green line shows solutions for which small and large perturbations propagate both with either positive or negative speeds. Blue line show solution for which small perturbations propagate with positive speed and large perturbations with negative. Note that Eq. (4.44) requires that for stationary homogeneous solution $\tilde{v}_g < 0.6622$.

Valid solutions can bee seen in Fig. 4.5. We see that for negative value of $\tilde{v}_g$ we have 3 solutions and for positive value of $\tilde{v}_g$ up to 2 solutions.This suggest that for negative values of v_g we can observe wide traffic jams or if initial density is too low narrow traffic jams and for positive value of $\tilde{v}_g$ we can observe only narrow traffic jams. To observe wide traffic jams (see Fig. 4.8) we need two non-stationary homogeneous solutions: one with larger density than homogeneous stationary solution and one with smaller density than stationary homogeneous solution. To observe narrow traffic jams (see Fig. 4.7) we need one stationary non-homogeneous solution with density smaller than for homogeneous solution. Numerical simulations (see Sec. 4.6) confirm

these conclusions.

4.5.2. Non-homogeneous solutions

As for stationary profiles also for stationary moving profiles in general case it is not possible to solve Eq. (4.40) analytically. Analytically one is able to find to solve only for case with $\Delta\tilde{x} = 0$ (see Sec. A.1.2 in Appendix). However, as we saw already for stationary solutions, $\lim_{\Delta\tilde{x}\to 0+}$ and case $\Delta\tilde{x} = 0$ gives different results and not much useful information can be extracted from case $\Delta\tilde{x} = 0$.

The only option is to try to solve Eq. (4.40) numerically. But unfortunately currently we are still unsuccessful with this task. Neither shooting or Newton's method (see Sec. A.1.3 in Appendix) works. Newton's method does not work even when for initial conditions long time solution with approximate value of $\tilde{v}_g$ (see Sec. 4.6) are used. The problem is that Eq. (4.40) is really sensitive to parameter $\tilde{v}_g$ and it has to be determined with higher than double precision and small deviations immediately lead to unphysical solutions for which in some interval ($\tilde{v} < 0$ or $\tilde{v} > 1$ or $\tilde{\rho} < 0$).

4.6. Numerical simulations

Eq. (4.10) can not be solved analytically, so it has to be solved numerically. As in each cell density and velocity is constant and cells has the same size, it was decided to use finite difference approach. Spacial derivatives are approximated with central finite differences:

$$\frac{\partial\tilde{\rho}_i}{\partial\tilde{x}} = \frac{\tilde{\rho}_{i+1} - \tilde{\rho}_{i-1}}{2\tilde{h}} \quad ; \quad \frac{\partial\tilde{v}_i}{\partial\tilde{x}} = \frac{\tilde{v}_{i+1} - \tilde{v}_{i-1}}{2\tilde{h}} \tag{4.45}$$

$$\frac{\partial^2\tilde{\rho}_i}{\partial\tilde{x}^2} = \frac{\tilde{\rho}_{i+1} - 2\tilde{\rho}_i + \tilde{\rho}_{i-1}}{\tilde{h}^2} \quad ; \quad \frac{\partial^2\tilde{v}_i}{\partial\tilde{x}^2} = \frac{\tilde{v}_{i+1} - 2\tilde{v}_i + \tilde{v}_{i-1}}{\tilde{h}^2} \tag{4.46}$$

and as in each cell velocity and density is constant, obviously space discretization step has to be $\tilde{h} = \Delta\tilde{x}$. Note that only if $\tilde{h} = \Delta\tilde{x}$ Eqs. (4.7) and (4.8) give the same results and if this condition is not satisfied then simulations of Eq. (4.7) shows that there is no stable long time solution with only positive values of density and velocity. For circular road segment (periodic

boundary conditions) with length $\tilde{L} = N\Delta\tilde{x}$ now we have

$$\begin{aligned}
\frac{\partial\tilde{\rho}_1}{\partial t} &= \frac{1}{\alpha\Delta x}\left(\tilde{\rho}_N\tilde{v}_1 - \tilde{\rho}_1\tilde{v}_2\right)\\
\frac{\partial\tilde{v}_1}{\partial\tilde{t}} &= -\frac{1}{2\alpha\Delta x}\tilde{v_1}\left(v_2 - v_N\right) + \left(\frac{1}{\tilde{\rho_2}^2+1} - \tilde{v_1}\right)\\
\frac{\partial\tilde{\rho}_i}{\partial t} &= \frac{1}{\alpha\Delta x}\left(\tilde{\rho}_{i-1}\tilde{v}_i - \tilde{\rho}_i\tilde{v}_{i+1}\right)\\
\frac{\partial\tilde{v}_i}{\partial\tilde{t}} &= -\frac{1}{2\alpha\Delta x}\tilde{v_i}\left(v_{i+1} - v_{i-1}\right) + \left(\frac{1}{\tilde{\rho_i}^2+1} - \tilde{v_i}\right)\\
\frac{\partial\tilde{\rho}_N}{\partial t} &= \frac{1}{\alpha\Delta x}\left(\tilde{\rho}_{N-1}\tilde{v}_N - \tilde{\rho}_N\tilde{v}_1\right)\\
\frac{\partial\tilde{v_N}}{\partial\tilde{t}} &= -\frac{1}{2\alpha\Delta x}\tilde{v_N}\left(v_1 - v_{N-1}\right) + \left(\frac{1}{\tilde{\rho_N}^2+1} - \tilde{v_N}\right)\ ,
\end{aligned} \tag{4.47}$$

where $i = 2, 3, \ldots, N-1$.

Then Eq. (4.47) starting from some initial conditions is solved with Runge-Kutta 4th order method.

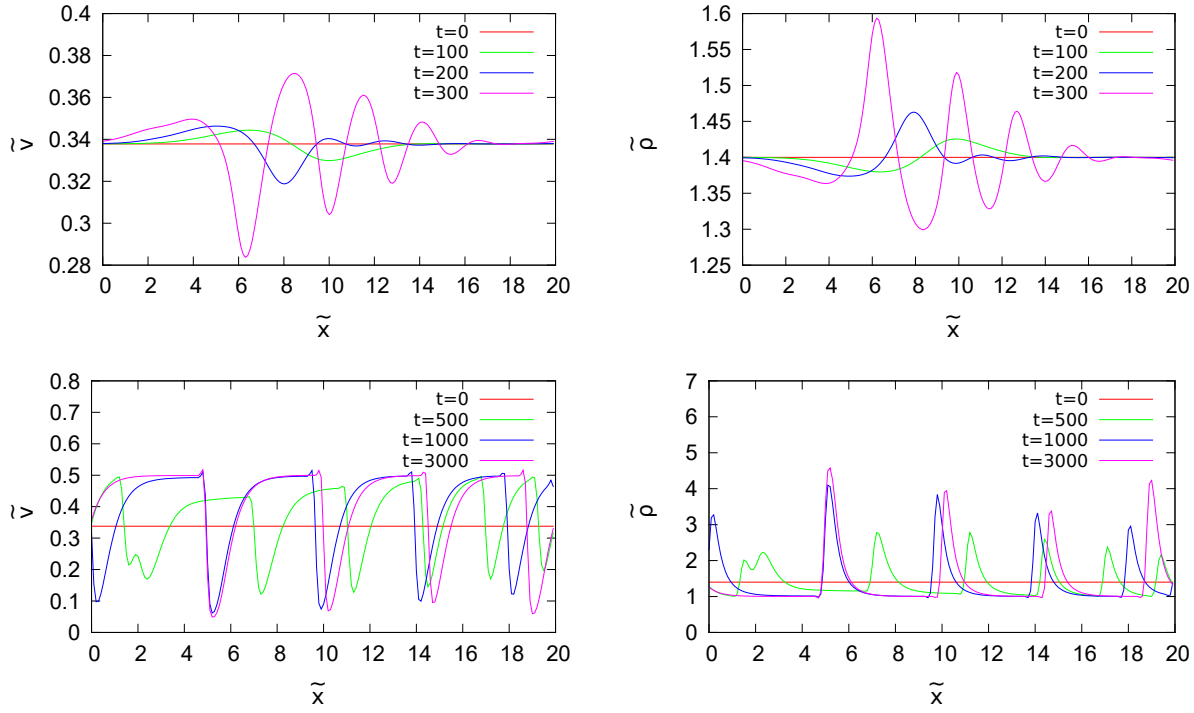

Figure 4.6.: Solution of Eq. (4.10) with $\alpha = 4.0$, $\tilde{L} = 20$, $\Delta\tilde{x} = 0.1$ starting with homogeneous solution $\tilde{\rho}(\tilde{x}, \tilde{t} = 0) = \tilde{\rho}_h = 1.4$, $\tilde{v}(\tilde{x}, \tilde{t} = 0) = \tilde{v}_h = \frac{1}{1+\tilde{\rho}_h^2}$.

Solutions of Eq. (4.47) with initial conditions $\tilde{\rho}(\tilde{x}, \tilde{t} = 0)$ and $\tilde{v}(\tilde{x}, \tilde{t} = 0)$ which correspond

homogeneous density solution

$$\tilde{\rho}_h = \frac{1}{\tilde{L}} \int_0^{\tilde{L}} \mathrm{d}\tilde{x}\ \tilde{\rho}(\tilde{x}, \tilde{t} = 0) \tag{4.48}$$

and with parameter values of α and $\Delta\tilde{x}$, such that Eq. (4.24) is satisfied, shows that homogeneous flow solution is unstable and clusters are formed (see Fig. 4.6). Note that even by choosing $\tilde{\rho}(\tilde{x}, \tilde{t} = 0) = \tilde{\rho}_h$ and $\tilde{v}(\tilde{x}, \tilde{t} = 0) = \tilde{v}_h$ (as in Fig. 4.6) roundoff errors will create small perturbations and after some time clusters will be formed. This process can be accelerated by adding small perturbation already in velocity profile in initial conditions $\tilde{v}(\tilde{x}, \tilde{t} = 0) = \tilde{v}_h + \varepsilon(\tilde{x})$, where $\varepsilon(\tilde{x})$ is small perturbation. Fig. 4.6 shows that at the beginning one cluster is created which then splits into several narrow clusters. The number of these narrow clusters is proportional to length $\tilde{L}$ of circular road. These clusters have different peak value of density and thats why they propagate with different speeds and collide. After collision of two clusters one cluster with higher peak value of density than any of colliding clusters and one or several clusters with smaller peak value of density than any of colliding clusters are created. These clusters with small peak value of density are fast absorbed by clusters with much higher peak value of density. When conditions are such that wide traffic jams can not appear ($\tilde{v}_g > 0$ or $\alpha\Delta\tilde{x} < 0.32$ or initial density is not high enough to have wide traffic jams) clusters fast collide until only one narrow cluster remains (see Fig. 4.7).

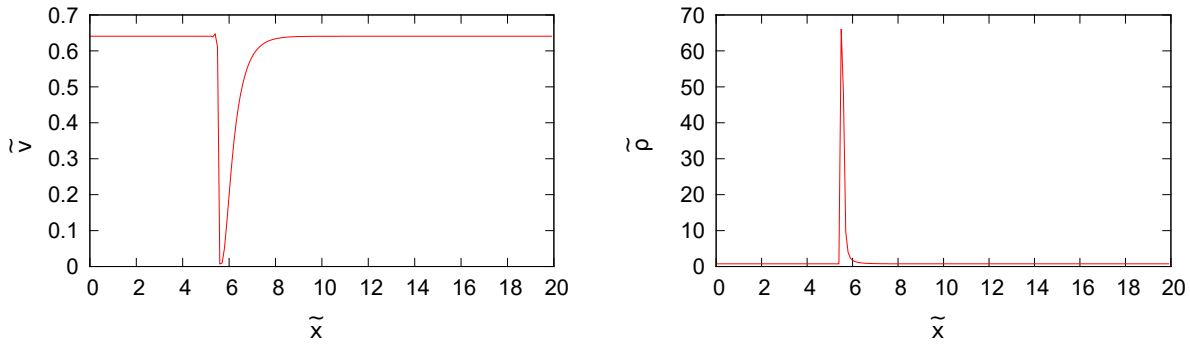

Figure 4.7.: Long time solution of Eq. (4.10) with $\alpha = 3.2$, $\tilde{L} = 20$, $\Delta\tilde{x} = 0.1$ starting with homogeneous density profile $\tilde{\rho}(\tilde{x}, \tilde{t} = 0) = \tilde{\rho}_h = 1.4$. We can see that in this case long time solution is one narrow jam (cluster).

When conditions are such that wide traffic jams appears then after narrow cluster collisions two or more wide clusters appears. All wide clusters have the same maximum and almost the same propagation speed. So it takes months long simulations (Intel Core 2 Quad processor

Q9300, 2.50 Ghz) until one wide cluster is reached (see Fig. 4.8).

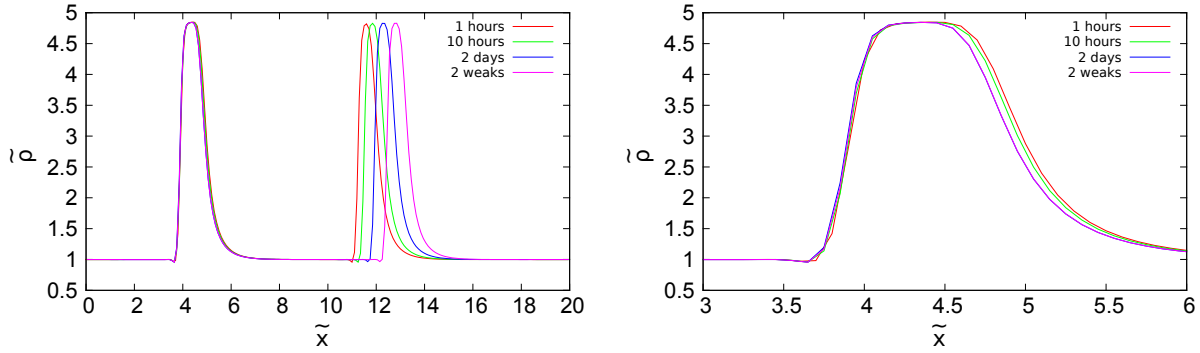

Figure 4.8.: Long time solution of Eq. (4.10) with $\alpha = 4$, $\tilde{L} = 20$, $\Delta\tilde{x} = 0.1$ starting with homogeneous density profile $\tilde{\rho}(\tilde{x}, \tilde{t} = 0) = \tilde{\rho}_h = 1.4$ (the same initial conditions and parameter values as for Fig. 4.6). The time is computational time needed on Intel Core 2 Quad processor Q9300 (2.50 Ghz). We see that solution with two wide jams are quasi stationary and it would take moth to reach solution with only one wide jam.

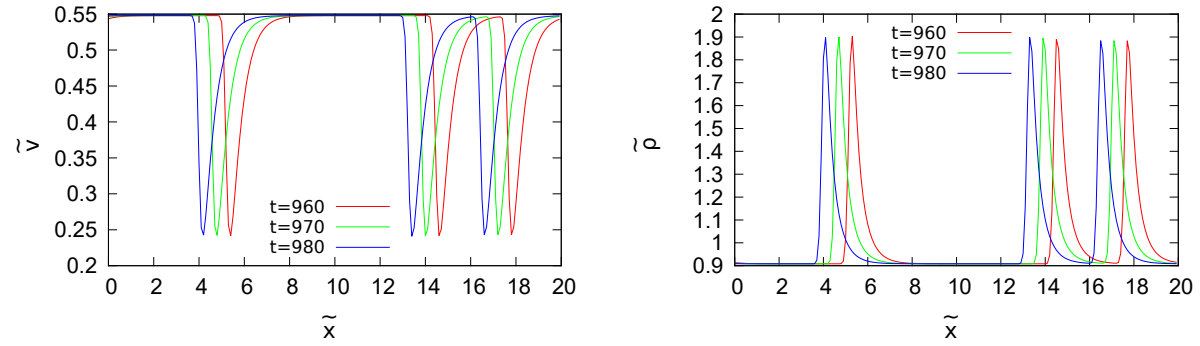

Figure 4.9.: Clusters moving in the opposite direction to moving direction of cars. (Cars drive such that $\tilde{x}$ increases.)

Generally as we already know Eq. (4.10) describes 2 types of clusters, those which are moving in the opposite direction to moving direction of cars (negative value of $\tilde{v}_g$ see Fig. 4.9) and in the same direction (positive value of $\tilde{v}_g$ see Fig. 4.10). In general if we start with initial condition which correspond to $\tilde{\rho}_h < 1$ we always end with clusters with positive value of $\tilde{v}_g$. This well much with the results from linear perturbation analysis. But if we start with initial condition which correspond to $\tilde{\rho}_h > 1$, situation is more complicated. For $\alpha\Delta\tilde{x} > 0.32$ we always have clusters with negative value of $\tilde{v}_g$. For $\alpha\Delta\tilde{x} < 0.30$ as long time solution we always have clusters with positive value of $\tilde{v}_g$. Generally by increasing value of $\alpha\Delta\tilde{x}$ we reduce value of $\tilde{v}_g$. For $0.32 < \alpha\Delta\tilde{x} < 0.30$ sign of $\tilde{v}_g$ depends on density and clusters are moving really slow. Also for small, but negative values of $\tilde{v}_g$ (blue line in Fig. 4.5), we observe that clusters with

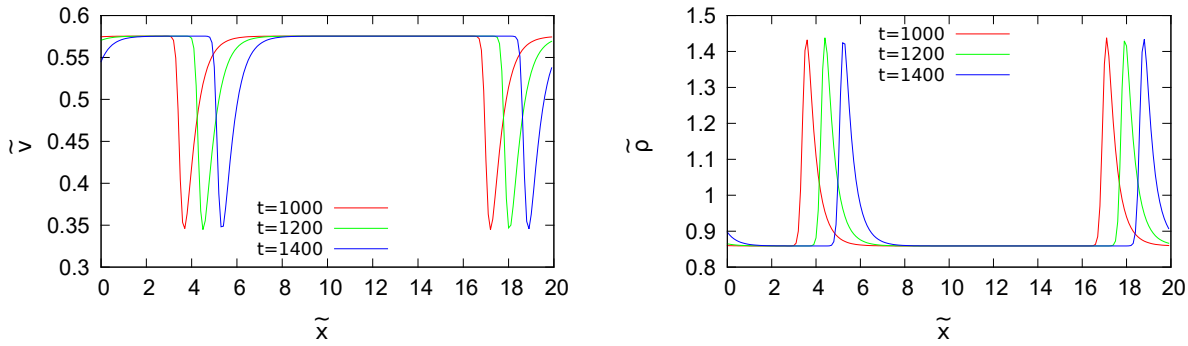

Figure 4.10.: Clusters moving in the same direction as cars. (Cars drive such that $\tilde{x}$ increases.)

large and small peak densities moves in opposite direction. This of course shows that linear perturbation analysis is insufficient.

The shapes of profiles (when there are only narrow clusters) with positive and negative value of $\tilde{v}_g$ (see Figs. 4.9 and 4.10) are quite similar. These profiles we can describe with peak value of cluster density $\tilde{\rho}_{paek}$ and homogeneous density outside cluster $\tilde{\rho}_{free}$. The value of $\tilde{\rho}_{free}$ actually well much with smallest value non-stationary homogeneous solutions of Eq. (4.43) (blue and green lines in Fig. 4.5). As for negative value of $\tilde{v}_g$ there are 2 non-stationary homogeneous solutions solutions of Eq. (4.43), the second solution match to $\tilde{\rho}_{paek}$ if initial density is high enough to observe wide jams.

5. Summary

This thesis is divided into three parts.

First part (Chap. 2) is about empirical (experimental) data analysis obtained from video recordings. The aim is to prepare empirical data (fundamental diagrams, field data, vector field data) for comparison with theoretical models. First we try to get general information about traffic flow and rough data quality from all available highway data sets. Based on information obtained from vehicle trajectory plots and space-time plots as well as number of vehicle trajectories contained in data sets it was decided for further analysis to use only 3 subsets of I-80 data set. As a rough analysis of video and trajectory data files of I-80 data showed that data contains errors, it was attempted to correct all errors which are possible to correct (errors for velocity and acceleration and lane changing errors). After error correction fundamental diagrams, field and vector field data was plotted. Fundamental diagrams show large lane changing influence and are reverse λ-shaped. The field and vector field data show large impact of the velocity difference to the car in front. Unfortunately field data contains artifacts (cars like to drive with velocity which is almost precisely 5, 10, 15, 20,... in feet/s more than with the values between these velocities independent of time and position). Analysis shows that these artifacts have to be produced with video post-processing software NG-VIDEO and probably are caused by the fact that ranges of cameras do not overlap. As almost every car has these artifacts, we must assume that errors for velocity is at least 2.5 feet/s. This unfortunately do not allow to do any further analysis for noise and raise question about quality of data.

Second part (Chap. 3) is about building a microscopic traffic model based on optimal velocity model and analysis of empirical traffic data. Here we try to improve optimal velocity model by Bando et al. by adding explicit velocity difference to the vehicle in front dependence. Construction is partly based on results of empirical data analysis and improvements proposed before [12, 15]. For improved model linear stability analysis, vehicle and wall (standing vehicle) collision test and time series simulations are preformed. The improved model shows better match to

fundamental diagrams from empirical data, smaller values of acceleration and deceleration, the values for deceleration are larger then for acceleration, faster convergence to long-time solution then optimal velocity model. However, when we compare results with field data and vector field data with empirical data we see clear differences. The reason for that are both the model itself and the simplified traffic situation. To reduce these differences the next step would be to add stochasticity to the model.

Third part (Chap. 4) is an analysis of fluid dynamical model by Martin Hilliges and Wolfgang Weidlich. The analysis is mainly focused on traffic jam formation and shape. For this model linear stability and dispersion analysis as well as time series simulations are preformed. The long-time solution for this model are wide and narrow (can be interpreted as traffic jam with only two cars in it) traffic jams. The difference to the microscopic model is that narrow traffic jams can propagate in the same direction as cars are driving or in opposite direction (usual propagation direction of jams). But this can be controlled by model parameter Δx. By choosing $\alpha\Delta x > 0.5$ jams can propagate only in usual direction. Unfortunately we are currently unable to calculate long-time solutions in reasonable time when long-time solution is wide jam. So we are unable to provide further comparison to empirical data and to microscopic model.

To show complete work done during writing this thesis also copy of accepted publication "Power laws and skew distributions" by R. Mahnke, J. Kaupužs, and M. Brics is appended as Chap. B in Appendix.

Acknowledgment

I would like to express gratitude to my supervisor Reinhard Mahnke who gave me many useful suggestions and consulted how to improve writing style. Also I am thankful to Peter Wagner and Reinhart Kühne who came with many valuable comments. Finally I appreciate Oskars Rubenis who helped me with grammar and vocabulary issues.

Erklärung

Ich versichere hiermit an Eides statt, dass ich die vorliegende Arbeit selbstständig angefertigt und ohne fremde Hilfe verfasst habe, keine außer den von mir angegebenen Hilfsmitteln und Quellen dazu verwendet habe und die den benutzten Werken inhaltlich und wörtlich entnommenen Stellen als solche kenntlich gemacht habe.

Rostock, den 12.09.2011

Mārtiņš Brics

Bibliography

[1] http://ngsim-community.org/. Accessed: 30/07/2010.

[2] http://www.fhwa.dot.gov/publications/research/operations/06137/index.cfm. Accessed: 28/02/2011.

[3] M. Bando, K. Hasebe, A. Nakayama, A. Shibata, and Y. Sugiyama. Structure stability of congestion in traffic dynamics. Japan Journal of Industrial and Applied Mathematics, 11(2):203–223, 1994.

[4] M. Bando, K. Hasebe, A. Nakayama, A. Shibata, and Y. Sugiyama. Dynamical model of traffic congestion and numerical simulation. Physical Review E, 51:1035–1042, 1995.

[5] O. Biham, A.A. Middleton, and D. Levine. Self-organization and a dynamical transition in traffic-flow models. Physical Review A, 46(10):6124–6127, 1992.

[6] D.C. Gazis, R. Herman, and R.B. Potts. Car-following theory of steady-state traffic flow. Operations Research, pages 499–505, 1959.

[7] D.C. Gazis, R. Herman, and R.W. Rothery. Nonlinear follow-the-leader models of traffic flow. Operations Research, pages 545–567, 1961.

[8] P.G. Gipps. A behavioural car-following model for computer simulation. Transportation Research Part B: Methodological, 15(2):105–111, 1981.

[9] B.D. Greenshields. A study in highway capacity. In Highway Research Board Proceedings, volume 14, pages 448–477, 1935.

[10] D. Helbing. Verkehrsdynamik: Neue physikalische Modellierungskonzepte. Springer, 1997.

[11] D. Helbing. Traffic and related self-driven many-particle systems. Reviews of modern physics, 73(4):1067–1141, 2001.

[12] D. Helbing and B. Tilch. Generalized force model of traffic dynamics. Physical Review E, 58(1):133, 1998.

[13] P. Hidas. Modelling lane changing and merging in microscopic traffic simulation. Transportation Research Part C: Emerging Technologies, 10(5-6):351–371, 2002.

[14] M. Hilliges and W. Weidlich. A phenomenological model for dynamic traffic flow in networks. Transportation Research Part B: Methodological, 29(6):407–431, 1995.

[15] R. Jiang, Q. Wu, and Z. Zhu. Full velocity difference model for a car-following theory. Physical Review E, 64(1):017101, 2001.

[16] B.S. Kerner. The physics of traffic: Empirical freeway pattern features, engineering applications, and theory. Springer Verlag, 2004.

[17] B.S. Kerner and P. Konhäuser. Cluster effect in initially homogeneous traffic flow. Physical Review E, 48(4):2335–2338, 1993.

[18] Christof Liebe. Physics of traffic flow: Empirical data and dynamical models. PhD thesis, Rostock University, 2010. See `http://rosdok.uni-rostock.de`.

[19] R. Mahnke, J. Kaupužs, and I. Lubashevsky. Probabilistic description of traffic flow. Physics Reports, 408:1–130, 2005.

[20] R. Mahnke and N. Pieret. Stochastic master–equation approach to aggregation in freeway traffic. Physical Review E, 56:2666–2671, 1997.

[21] K. Nagel and M. Schreckenberg. A cellular automaton model for freeway traffic. Journal de Physique I France, 2:2221–2229, 1992.

[22] G.F. Newell. Nonlinear effects in the dynamics of car following. Operations Research, pages 209–229, 1961.

[23] L.A. Pipes. An operational analysis of traffic dynamics. Journal of applied physics, 24(3):274–281, 1953.

[24] A. Reuschel. Fahrzeugbewegungen in der Kolonne. Österreichisches Ingenieurarchiv, 4:193–215, 1950.

[25] A. Savitzky and M. J. E. Golay. Smoothing and differentiation of data by simplified least squares procedures. Analytical Chemistry, 36(8):1627–1639, 1964.

[26] M. Treiber and D. Helbing. Explanation of observed features of self-organization in traffic flow. Arxiv preprint cond-mat/9901239, 1999.

[27] P. Wagner. Fluid-dynamical and microscopic description of traffic flow: a data-driven comparison. Philosophical Transactions of the Royal Society A: Mathematical, Physical and Engineering Sciences, 368(1928):4481–4495, 2010.

[28] XUE Yu, D. Li-yun, Y. Yi-wu, and DAI Shi-Qiang. The effect of the relative velocity on traffic flow. Communications in Theoretical Physics, 38(8):230–234, 2002.

A. Appendix

A.1. Additional sections for Chap. 4

A.1.1. Stationary non-homogeneous solutions for $\Delta\tilde{x} = 0$

By setting $\Delta\tilde{x} = 0$ in Eq. (4.35) we have

$$\tilde{\rho}\tilde{v} = C\,, \tag{A.1}$$

$$\frac{\partial\tilde{v}}{\partial\tilde{x}} = \alpha\left(\frac{\tilde{v}}{C^2+\tilde{v}^2} - 1\right)\,. \tag{A.2}$$

Eq. (A.2) can be straight forward integrated and we get that

$$\alpha\tilde{x} = -\tilde{v} + \frac{\ln|\frac{(2\tilde{v}-1)+\sqrt{1-4c^2}}{(2\tilde{v}-1)-\sqrt{1-4c^2}}|}{2\sqrt{1-4C^2}} - \frac{1}{2}\ln|\tilde{v}^2-\tilde{v}+C^2| + C_1\,. \tag{A.3}$$

The non-homogeneous stationary solutions for $C = 0.4$ which has homogeneous solutions $\{\tilde{\rho} = 2, \tilde{v} = 0.2\}$ and $\{\tilde{\rho} = 0.5, \tilde{v} = 0.8\}$ you can see in Figs. A.1 and A.2. Figs. A.1 and A.2 shows that we have 3 different non-homogeneous solutions and that stationary homogeneous solution with larger density ($\{\tilde{\rho} = 2, \tilde{v} = 0.2\}$) is unstable and with smaller density ($\{\tilde{\rho} = 0.5, \tilde{v} = 0.8\}$) is stable. We also see that none of these solution and also combination of solutions satisfies periodic boundary conditions.

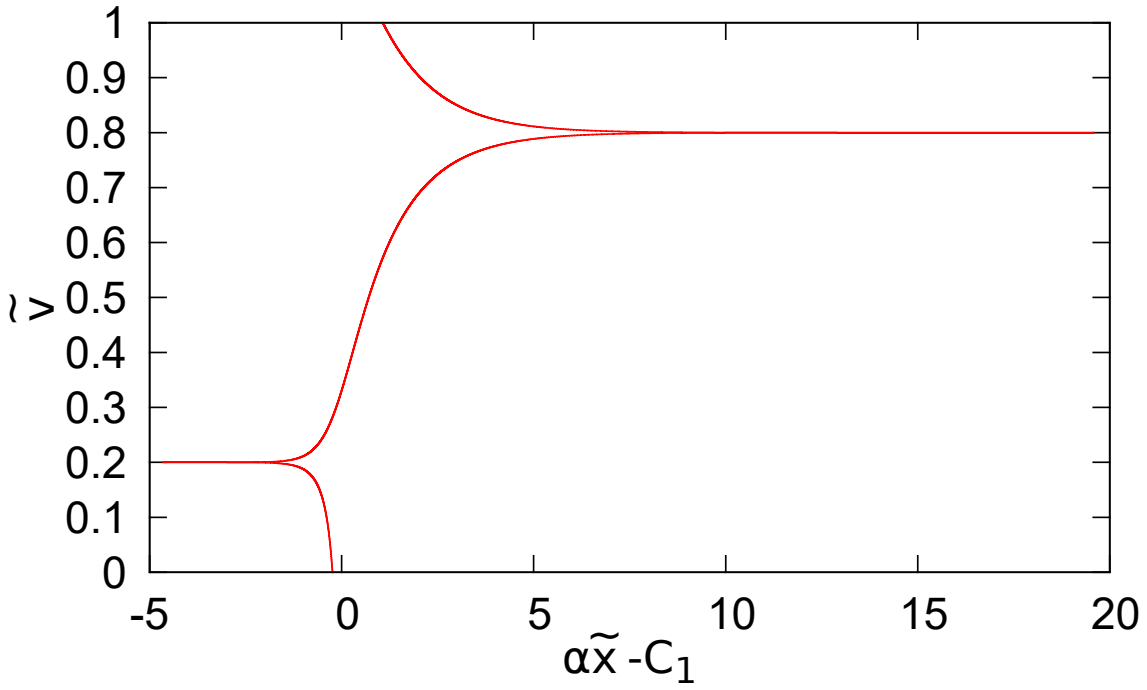

Figure A.1.: Non-homogeneous solutions for stationary velocity profiles for $C = 0.4$ if $\Delta\tilde{x} = 0$

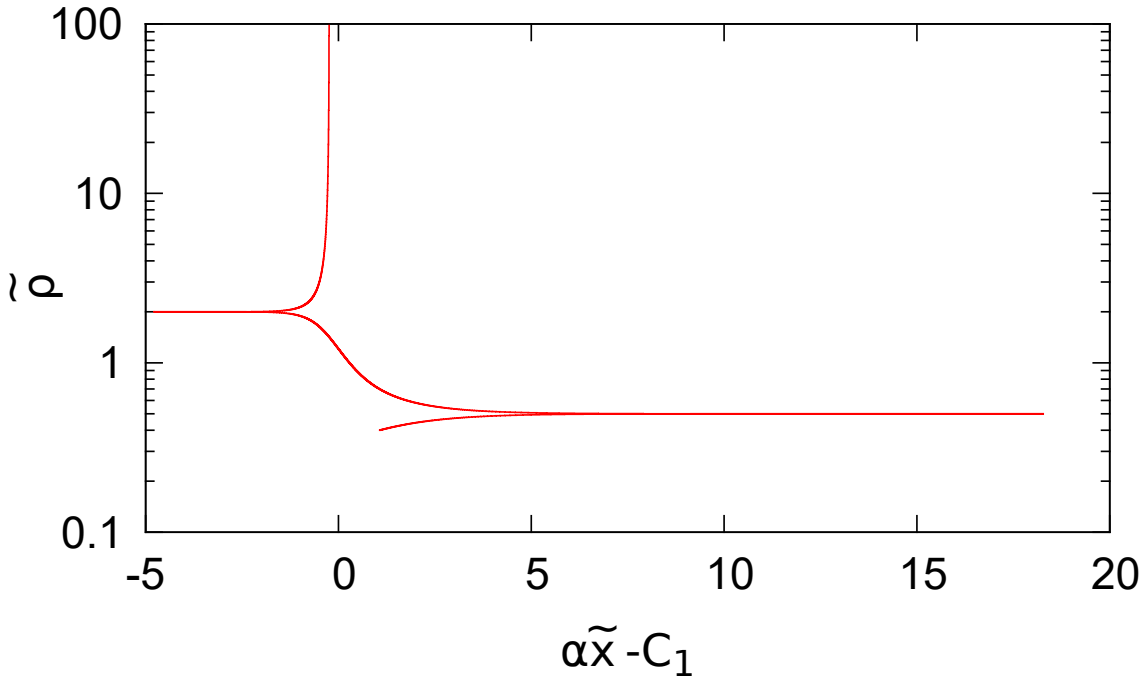

Figure A.2.: Non-homogeneous solutions for stationary density profiles for $C = 0.4$ if $\Delta\tilde{x} = 0$

A.1.2. Stationary moving profile for $\Delta\tilde{x} = 0$

By inserting $\Delta\tilde{x} = 0$ into Eq. (4.40) we have

$$\begin{aligned} C_g &= \tilde{\rho}\,(\tilde{v} - \tilde{v}_g) \\ \frac{\partial \tilde{v}}{\partial \tilde{\xi}} &= \frac{\alpha}{\tilde{v} - \tilde{v}_g}\left(\frac{1}{\tilde{\rho}^2 + 1} - \tilde{v}\right) . \end{aligned} \tag{A.4}$$

The Eq. (A.4) can be straight forward integrated

$$\tilde{\xi} + C_2 = \int \mathrm{d}\tilde{v}\, \left(\frac{(\tilde{v} - \tilde{v}_g)^2}{C_g^2 + (\tilde{v} - \tilde{v}_g)^2} - \tilde{v}\right)^{-1} , \tag{A.5}$$

but integral is too complicated to write it analytically, and has only physical meaning for $\tilde{v} > \tilde{v}_g$.

The non-homogeneous stationary moving profiles for $C \approx 0.473$ which has homogeneous solutions $\{\tilde{\rho} = 1.4, \tilde{v} \approx 0.338\}$ and $\{\tilde{\rho} \approx 0.714, \tilde{v} \approx 0.662\}$ for positive and negative value of $\tilde{v}_g$ you can see in Fig. A.3.

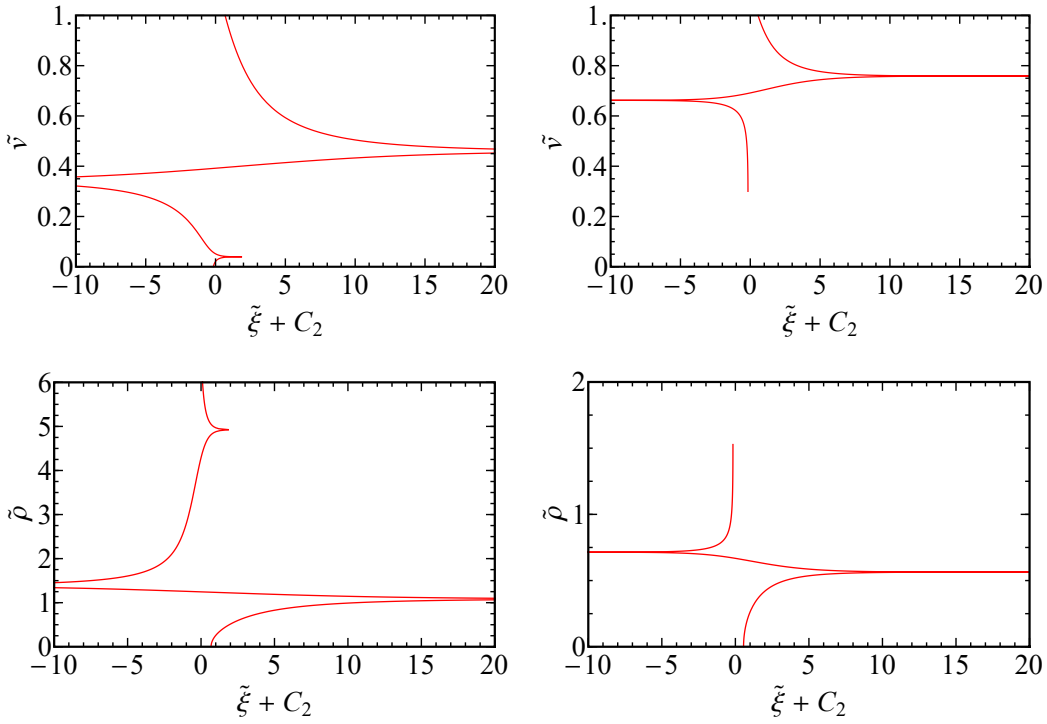

Figure A.3.: Non-homogeneous solutions for stationary moving velocity and density profiles for $C \approx 0.473$ if $\Delta\tilde{x} = 0$. Left figures are for $\tilde{v}_g = -0.079$ and right for $\tilde{v}_g = 0.3$.

As expected from Fig. A.3 we see that for negative value of $\tilde{v}_g$ we have 3 homogeneous solutions and that only stationary homogeneous solution is unstable. For positive value of $\tilde{v}_g$

we have 2 homogeneous solutions and also only stationary homogeneous solution is unstable.

Also for this case we see that none of these solution and also combination of solutions satisfies periodic boundary conditions.

A.1.3. Newton's method for stationary moving profiles

One way how we can solve Eq. (4.40) is to use finite difference approach with Newton's method. For derivatives central differences again will be used:

$$\frac{\partial\tilde{\rho}_i}{\partial\tilde{\xi}} = \frac{\tilde{\rho}_{i+1} - \tilde{\rho}_{i-1}}{2\tilde{h}} \quad ; \quad \frac{\partial\tilde{v}_i}{\partial\tilde{\xi}} = \frac{\tilde{v}_{i+1} - \tilde{v}_{i-1}}{2\tilde{h}} \tag{A.6}$$

which inserting into (4.40) gives

$$\begin{aligned} &\frac{\tilde{\rho}_{i+1} - \tilde{\rho}_{i-1}}{2\tilde{h}} - \frac{2}{\Delta\tilde{x}}\left(\tilde{\rho}_i\left(1 - \frac{\tilde{v}_g}{\tilde{v}_i}\right) - \frac{C_g}{\tilde{v}_i}\right) - \frac{\alpha\tilde{\rho}_i}{\tilde{v}_i(\tilde{v}_i - \tilde{v}_g)}\left(\frac{1}{\tilde{\rho}_i^2 + 1} - \tilde{v}_i\right) = 0 \\ &\frac{\tilde{v}_{i+1} - \tilde{v}_{i-1}}{2\tilde{h}} - \frac{\alpha}{\tilde{v}_i - \tilde{v}_g}\left(\frac{1}{\tilde{\rho}_i^2 + 1} - \tilde{v}_i\right) = 0\,. \end{aligned} \tag{A.7}$$

As derivation of Martin Hilliges and Wolfgang Weidlich model assumes that $\tilde{\rho}$ and $\tilde{v}$ is constant in the cell it is only reasonable again to choose $\tilde{h} = \Delta\tilde{x}$. So $i \in [0; N]$ where N was number of cells.

As we want to solve Eq. (4.40) with periodic boundary conditions $\tilde{\rho}\big|_{\tilde{\xi}=0} = \tilde{\rho}\big|_{\tilde{\xi}=L}$ and $\tilde{v}\big|_{\tilde{\xi}=0} = \tilde{v}\big|_{\tilde{\xi}=L}$, then formally in Eq. (A.7) we need to replace $\tilde{\rho}_N = \tilde{\rho}_0$, $\tilde{\rho}_{-1} = \tilde{\rho}_{N-1}$, $\tilde{v}_N = \tilde{v}_0$, $\tilde{\rho}_{-1} = \tilde{\rho}_{N-1}$. However we have now $2N$ equations and $2N+2$ ($\tilde{v}_0 \dots \tilde{v}_{N-1}, \tilde{\rho}_0 \dots \tilde{\rho}_{N-1}, \tilde{v}_g, C_g$) unknowns. So we need to find 2 more equations.

As number of cars N_{cars} on circular road have to be conserved then

$$N_{cars} = \int_0^{\tilde{L}} d\tilde{\xi}\,\tilde{\rho}(\tilde{\xi}) = \tilde{\rho}_h\tilde{L} \tag{A.8}$$

and from mean value theorem we find out that at least in one point $\tilde{\xi}_0 \in [0; \tilde{L}]$, the density $\tilde{\rho}(\tilde{\xi}_0) = \tilde{\rho}_h = \frac{N_{cars}}{\tilde{L}}$. As on circular road we can choose $\tilde{\xi} = 0$ where we want, we can choose $\tilde{\xi}$ so that $\tilde{\rho}_0 = \tilde{\rho}_h$. We already also know that $C_g = C - \tilde{v}_g\tilde{\rho}_h$, so we now have equal number of

equations and unknown.

$$
\begin{aligned}
&\frac{\tilde{\rho}_1 - \tilde{\rho}_{N-1}}{2\Delta\tilde{x}} - \frac{2}{\Delta\tilde{x}\tilde{v}_0}\left(\tilde{\rho}_h\tilde{v}_0 - C\right) - \frac{\alpha\tilde{\rho}_h}{\tilde{v}_0(\tilde{v}_0 - \tilde{v}_g)}\left(\frac{1}{\tilde{\rho}_h^2+1} - \tilde{v}_0\right) = 0\\
&\frac{\tilde{\rho}_2 - \tilde{\rho}_h}{2\Delta\tilde{x}} - \frac{2}{\Delta\tilde{x}\tilde{v}_1}\left(\tilde{\rho}_1\tilde{v}_1 - C + \tilde{v}_g\left(\tilde{\rho}_h - \tilde{\rho}_1\right)\right) - \frac{\alpha\tilde{\rho}_1}{\tilde{v}_1(\tilde{v}_1 - \tilde{v}_g)}\left(\frac{1}{\tilde{\rho}_1^2+1} - \tilde{v}_1\right) = 0\\
&\frac{\tilde{\rho}_{i+1} - \tilde{\rho}_{i-1}}{2\Delta\tilde{x}} - \frac{2}{\Delta\tilde{x}\tilde{v}_i}\left(\tilde{\rho}_i\tilde{v}_i - C + \tilde{v}_g\left(\tilde{\rho}_h - \tilde{\rho}_i\right)\right) - \frac{\alpha\tilde{\rho}_i}{\tilde{v}_i(\tilde{v}_i - \tilde{v}_g)}\left(\frac{1}{\tilde{\rho}_i^2+1} - \tilde{v}_i\right) = 0\\
&\frac{\tilde{\rho}_h - \tilde{\rho}_{N-2}}{2\Delta\tilde{x}} - \frac{2}{\Delta\tilde{x}}\left(\tilde{\rho}_{N-1} - \frac{C}{\tilde{v}_{N-1}} + \frac{\tilde{v}_g\left(\tilde{\rho}_h - \tilde{\rho}_{N-1}\right)}{\tilde{v}_{N-1}}\right) - \frac{\alpha\tilde{\rho}_{N-1}}{\tilde{v}_{N-1}(\tilde{v}_{N-1} - \tilde{v}_g)}\left(\frac{1}{\tilde{\rho}_{N-1}^2+1} - \tilde{v}_{N-1}\right) = 0\\
&\frac{\tilde{v}_1 - \tilde{v}_{N-1}}{2\Delta\tilde{x}} - \frac{\alpha}{\tilde{v_0} - \tilde{v}_g}\left(\frac{1}{\tilde{\rho}_h^2+1} - \tilde{v}_0\right) = 0\\
&\frac{\tilde{v}_2 - \tilde{v}_0}{2\Delta\tilde{x}} - \frac{\alpha}{\tilde{v_1} - \tilde{v}_g}\left(\frac{1}{\tilde{\rho}_1^2+1} - \tilde{v}_1\right) = 0\\
&\frac{\tilde{v}_{i+1} - \tilde{v}_{i-1}}{2\Delta\tilde{x}} - \frac{\alpha}{\tilde{v_i} - \tilde{v}_g}\left(\frac{1}{\tilde{\rho}_i^2+1} - \tilde{v}_i\right) = 0\\
&\frac{\tilde{v}_0 - \tilde{v}_{N-2}}{2\Delta\tilde{x}} - \frac{\alpha}{\tilde{v_{N-1}} - \tilde{v}_g}\left(\frac{1}{\tilde{\rho}_{N-1}^2+1} - \tilde{v}_{N-1}\right) = 0\\
&i = 2, 3, \ldots, N-2\,.
\end{aligned}
\tag{A.9}
$$

Now lets introduce vector $\boldsymbol{X} = \{\tilde{v}_g, \tilde{\rho}_1, \tilde{\rho}_2, \ldots, \tilde{\rho}_{N_1}, \tilde{v}_0, \tilde{v}_1, \ldots, \tilde{v}_{N-1}\}^T$ of length $2N$ and vector function $\boldsymbol{F}(\boldsymbol{X}) = \{F_0(\boldsymbol{X}), F_1(\boldsymbol{X}), \ldots, F_{N-1}(\boldsymbol{X})\}^T$ such that $F_j(\boldsymbol{X})$ is the left side of j-th equation of Eq. (A.9). Now we can write Eq. (A.9) in concise form $\boldsymbol{F}(\boldsymbol{X}) = 0$. Eq. (A.9) is going to be solved with Newton method. In order to do so, first we need to introduce Jacobian matrix $\boldsymbol{J}(\boldsymbol{X})$ with elements $J_{ij}(\boldsymbol{X}) = \frac{\partial f_i(\boldsymbol{X})}{\partial X_j}$ and some vector $\boldsymbol{h}^m = \{h_0, h_1, \ldots, h_{N-1}\}^T$. Then from good initial guess $\boldsymbol{X}^0$, we after some number m of iterations (A.10) we should reach solution up to machine precision.

$$
\begin{cases}
\boldsymbol{J}(\mathbf{X}^m)\boldsymbol{h}^m = -\mathbf{F}(\mathbf{X}^m)\\
\mathbf{X}^{m+1} = \mathbf{X}^m + \mathbf{h}^m
\end{cases}
\tag{A.10}
$$

But to do this we need to calculate Jacobian matrix elements. All possible non-zero elements of J can be seen in Eqs (A.11) - (A.25) .

$$
J_{i,i-1} = -\frac{1}{2\Delta\tilde{x}} \quad \text{for all } i \notin \{0, 1, N\} \tag{A.11}
$$

$$
J_{0,N-1} = -\frac{1}{2\Delta\tilde{x}} \tag{A.12}
$$

$$J_{N,2N-1} = -\frac{1}{2\Delta\tilde{x}} \tag{A.13}$$

$$J_{i,i+1} = \frac{1}{2\Delta\tilde{x}} \quad \text{for all } i \notin \{N-1, 2N-1\} \tag{A.14}$$

$$J_{2N-1,N} = \frac{1}{2\Delta\tilde{x}} \tag{A.15}$$

$$J_{i,i} = \frac{-2X_{N+i} + 2X_0}{dxX_{N+i}} + \frac{\tilde{\alpha}\left(X_i^2 - 1 + X_{N+i}X_i^4 + 2X_{N+i}X_i^2 + X_{N+i}\right)}{X_{N+i}\left(X_{N+i} - X_0\right)\left(X_i^2+1\right)^2} \quad \text{for } i \in [1, N-1] \tag{A.16}$$

$$J_{i,N+i} = 2\frac{X_0\left(\tilde{\rho}_h - X_i\right) - C}{dxX_{N+i}^2} - \frac{X_i\tilde{\alpha}\left(\left(X_i^2+1\right)X_{N+i}^2 - 2X_{N+i} + X_0\right)}{X_{N+i}^2\left(X_{N+i} - X_0\right)^2\left(X_i^2+1\right)} \quad \text{for } i \in [1, N-1] \tag{A.17}$$

$$J_{0,N} = -2\frac{C}{dxX_N^2} - \frac{X_i\tilde{\alpha}\left(\left(X_h^2+1\right)X_N^2 - 2X_N + X_0\right)}{X_N^2\left(X_N - X_0\right)^2\left(X_h^2+1\right)} \tag{A.18}$$

$$J_{N+i,i} = \frac{2\tilde{\alpha}}{X_{N+i} - X_0}\frac{X_i}{\left(X_i^2+1\right)^2} \quad \text{for } i \in [1, N-1] \tag{A.19}$$

$$J_{i,i} = \frac{\alpha}{\left(X_i - X_0\right)^2}\left(\frac{1}{X_{i-N}^2+1} - X_i\right) + \frac{\alpha}{X_i - X_0}\frac{1}{X_{i-N}^2+1} \quad \text{for } i \in [N+1, 2N-1] \tag{A.20}$$

$$J_{N,N} = \frac{\alpha}{\left(X_N - X_0\right)^2}\left(\frac{1}{\tilde{\rho}_h^2+1} - X_N\right) + \frac{\alpha}{X_N - X_0}\frac{1}{\tilde{\rho}_h^2+1} \tag{A.21}$$

$$J_{i,0} = 2\frac{X_i - \tilde{\rho}_h}{dxX_{N+i}} - \frac{\tilde{\alpha}X_i}{X_{N+i}\left(X_{N+i} - X_0\right)^2}\left(\frac{1}{X_i^2+1} - X_{N+i}\right) \quad \text{for } i \in [1, N-1] \tag{A.22}$$

$$J_{0,0} = -\frac{\tilde{\alpha}\tilde{\rho}_h}{X_N\left(X_N - X_0\right)^2}\left(\frac{1}{\tilde{\rho}_h^2+1} - X_N\right) \tag{A.23}$$

$$J_{i,0} = -\frac{\alpha}{(X_i - X_0)^2}\left(\frac{1}{X_{i-N}^2 + 1} - X_i\right) \quad \text{for } i \in [N+1, 2N-1] \tag{A.24}$$

$$J_{N,0} = -\frac{\alpha}{(X_N - X_0)^2}\left(\frac{1}{\tilde{\rho}_h + 1} - X_N\right) \tag{A.25}$$

A.2. Additional figures for Sec. 2.3

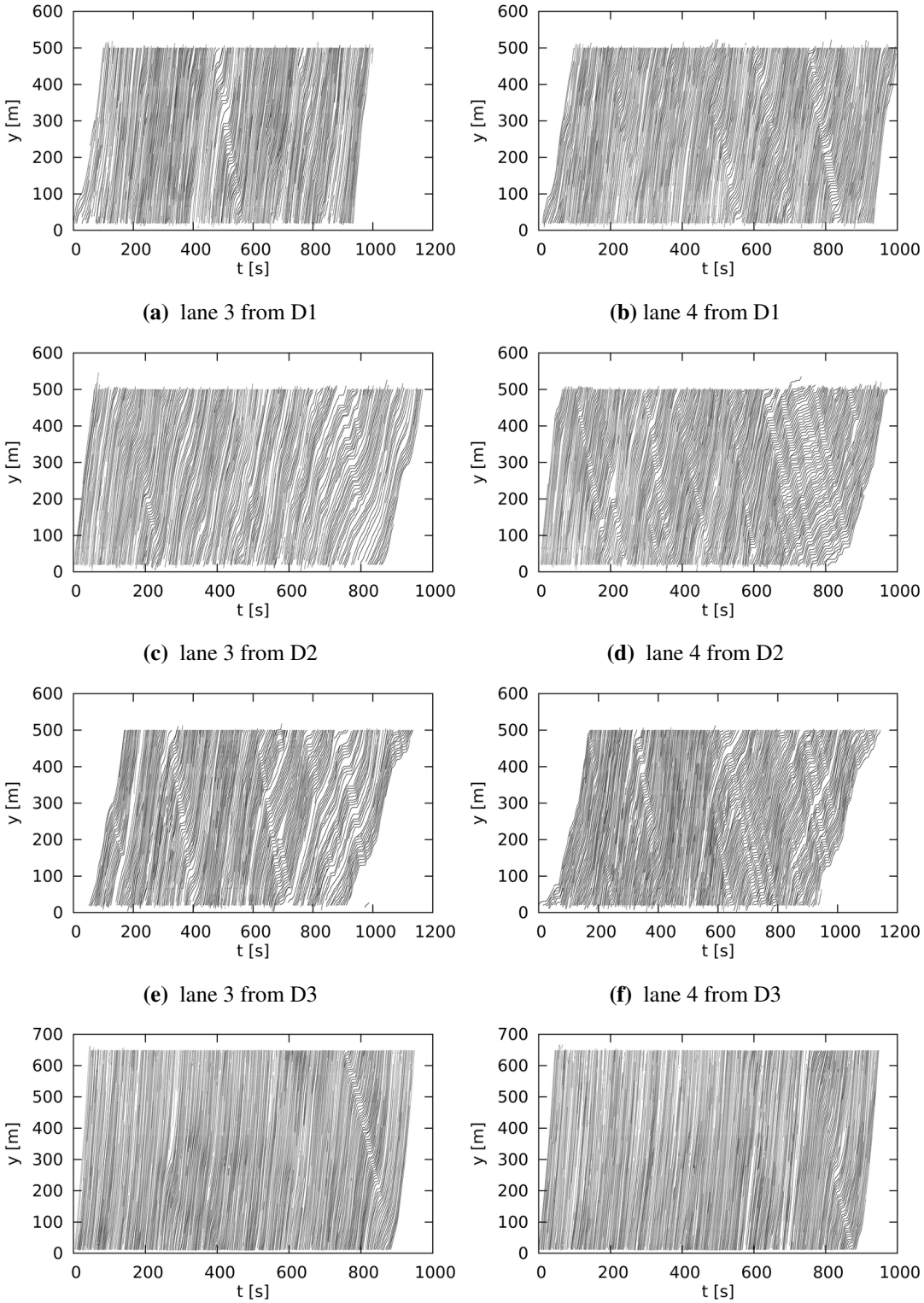

(a) lane 3 from D1

(b) lane 4 from D1

(c) lane 3 from D2

(d) lane 4 from D2

(e) lane 3 from D3

(f) lane 4 from D3

(g) lane 3 from US 101

(h) lane 4 from US 101

Figure A.4.: Space-time plots for lanes 3 and 4 from subsets D1, D2, D3 of data set I-80 and data set US 101.

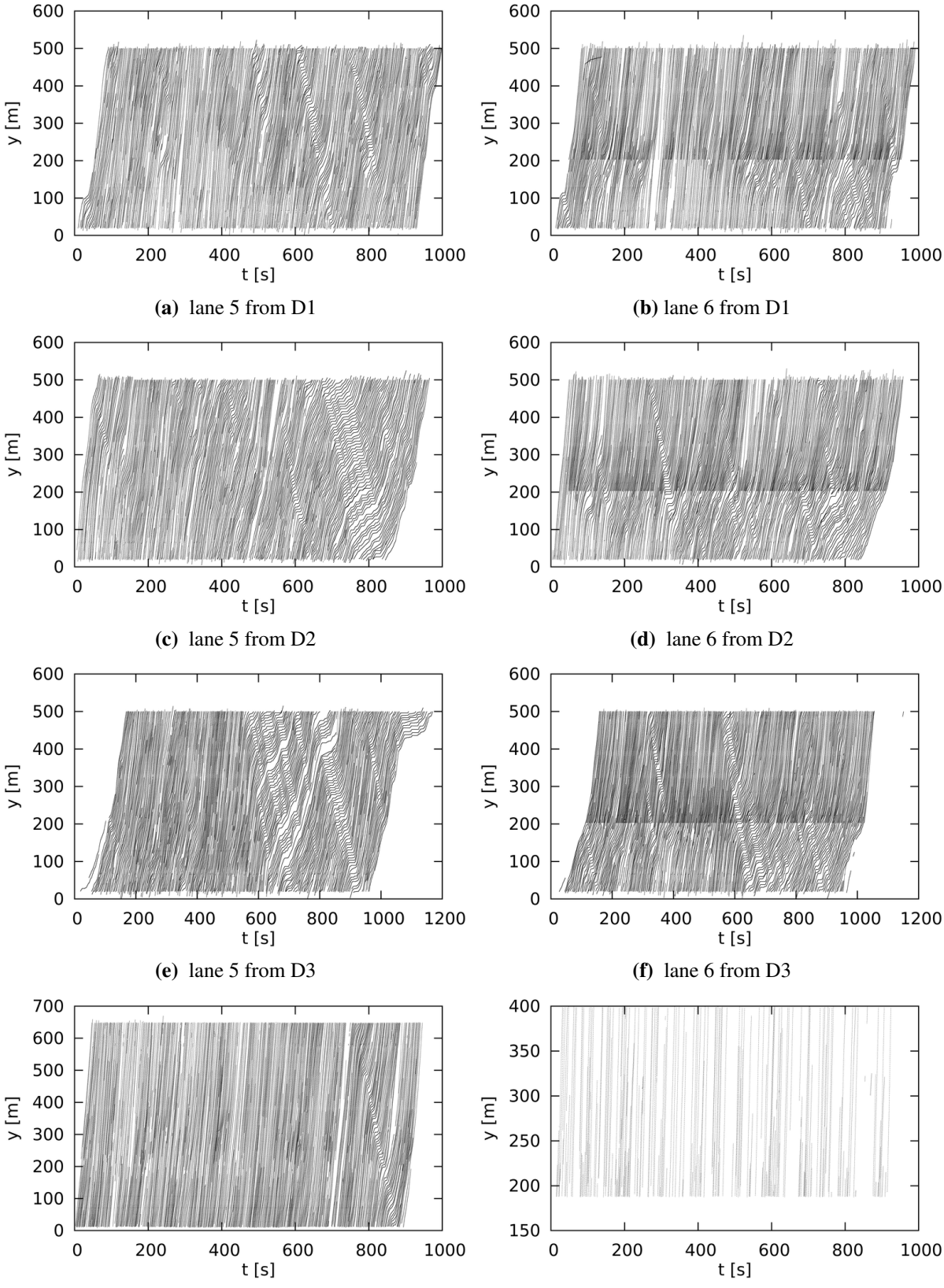

(a) lane 5 from D1

(b) lane 6 from D1

(c) lane 5 from D2

(d) lane 6 from D2

(e) lane 5 from D3

(f) lane 6 from D3

(g) lane 5 from US 101

(h) auxiliary lane from US 101

Figure A.5.: Space-time plots for lanes 5 and 6 from subsets D1, D2, D3 of data set I-80 and data set US 101.

B. Publication "Power laws and skew distributions" by R. Mahnke, J. Kaupužs, and M. Brics

B.1. Introduction

Power laws are observed in many systems. Particularly, one has to note the critical phenomena in interacting many–particle systems, which are associated with cooperative fluctuations of a large number of microscopic degrees of freedom. The singularities of various quantities in vicinity of the phase transition point are described by the critical exponents. It has been rigorously shown for a class of exactly solved models [1–3], which are mainly the two–dimensional lattice models. For three–dimensional systems, exact results are difficult to obtain, and approximate methods are usually used. A review of numerical results, as well as of the applied here standard perturbative renormalization group (RG) methods can be found, e. g., in [4]. An alternative approach has been proposed in [5]. There are also many textbooks devoted to this topic, e. g., [6–9]. A general review of critical phenomena in various systems can be found, e. g., in [10]. Recently, the role of quantum fluctuations in critical phenomena has been reviewed and discussed in [11].

Goldstone mode power–law singularities are observed also below the critical temperature in some systems, where the order parameter is an n–component vector with $n > 1$ (see, e. g., [12–17]). These systems are spin models having $O(n)$ rotational symmetry in zero external field. This is an interesting example of power law behavior, exhibited by the transverse and longitudinal correlation functions in the ordered phase. Moreover, according to the recent Monte Carlo (MC) simulation results [18–20], it is very plausible that this behavior is described by nontrivial exponents, as predicted in [17].

For a general review, one has to mention that phase transitions described by power laws and critical exponents are observed in variety of systems, such as social, economical, biological systems, as well as vehicular traffic flow, which are often referred in literature as non–physical systems. In particular, traffic flow is a driven one–dimensional system in which, unlike to one–dimensional equilibrium systems, phase transitions are observed. Formation of a car cluster on the road is analogous to aggregation phenomena in many physical systems [21]. The widely used approach in description of the vehicular traffic, as well as the traffic in biological systems such as ants, is the simulation by cellular automata models. One can mention here the famous Nagel–Schreckenberg model [22], which has numerous extensions, e. g., [23–29]. A good review about this topic can be found in [30]. Stochastic fluctuations play an important role here. A new approach to this problem, emphasizing the role of the stochasticity, has been introduced in [31]. The master equation is used here to describe the jam formation on a road as a stochastic one–step process, in which the size of a car cluster is a stochastic variable. The results of this approach have been summarized in the review paper [32], as well as in the recent textbook [33]. The critical behavior, found in a simple traffic flow model considered in [32], is described by the mean–field exponent $\beta = 1/2$ for the order parameter (see p. 75 in [32]).

The power laws in critical phenomena have been discussed in [34] in a general context of many other examples, where the power–law distributions emerge. A distinguishing feature of the critical phenomena is the existence of certain length scale, which diverges at specially chosen parameters, i. e., at the critical point. It results in a scale–free or power–law distribution. In some cases, however, no fine tuning of parameters is necessary to observe the critical phenomena. It refers to systems exhibiting the self–organized criticality. Any such system adjusts itself to the critical point due to some dynamical process. The percolation on square lattice have been discussed in [34] as an example of critical phenomena, and the forest fire model – as an example of the self–organized criticality. Spin systems with global rotational symmetry could be added here as a different example of the power–law behavior at a divergent length scale. Namely, the correlation length in such systems is divergent at vanishing external field not only at the critical temperature, but also below it. It results in the already mentioned here power–law Goldstone mode singularities.

Apart from the appearance of the divergent length scale, there are also other mechanisms how the power laws emerge. Many examples have been reviewed and discussed in [10, 34–37] pointing out the ubiquitous observation of power law distributions in nature. A tool for

analyzing power law distributed empirical data in presented in [36]. A set of mechanisms for power laws can be found in [10] based on self-organized criticality like damage and fracture of materials as well as multiplicative recurrence with stochastic variables. Power laws are common patterns in nature [37] and economics (known as Pareto distributions [34, 35]). The underlying cause seems to be stochasticity. We have addressed this question in Sec. B.2 by considering in detail certain model of evolving system.

B.2. Emergence of power–law distribution and other skew distributions in evolving systems

Power–law distribution can be considered as a particular case of the so called skew distributions. Examples of skew distributions are considered in various papers in literature, e. g., Zipf's law (power law) in rank–size distribution of cities [38] and log–normal distribution as a long–tailed duration distribution for disability in aged people [39]. A class of non–Gaussian distributions with power–law tails has been considered in [40]. In Chapt. 6 of [10], the stretched exponential function family and its generation is reviewed as intermediate between thin (like Gaussian) and fat tail (like power law) distributions. Certain extreme deviation mechanism has been discussed in [41], which can explain the appearance of stretched–exponential distribution in a number of physical and other systems, exhibiting anomalous probability distribution functions and relaxation behaviors. Examples are anomalous relaxations in glasses and velocity distribution in turbulent flow.

A generalized family of distributions, including the Pareto power law distribution as well as the Weibull distribution, has been considered in [42, 43]. It has been shown here that the power law family is nested into the Weibull family as certain limit case (see Eqs. (1) to (8) in [43]).

In [44] (see also comment on this paper [45]) some interesting ideas are developed how skew distributions such as power law, log–normal, and Weibull distributions emerge in general evolving systems and what makes the difference between them. According to [45], however, no correct answers to these fundamental questions have been found in [44]. Therefore, we have reconsidered this problem and have found an example, where the Weibull distribution really emerges.

We consider certain evolving system consisting of N elements, introduced already in [45]. Therefore, we will repeat some basic definitions and relations of [45], which are necessary for

the actual extended study. Each element of the evolving system has certain size, which is a discrete stochastic variable taking one of the values x_n, where $n = 1, 2, 3$, etc. The size of each element can increase from x_n to x_{n+1} with the transition rate $w(n)$. The number of elements $N = N(t)$ also increases with time, i. e., a new element of the minimal size x_1 is generated with certain rate $\mathcal{W}(N)$. Assuming $\mathcal{W}(N) = rN$, the probability $P(N, t)$ of having N elements at time t is given by the master equation

$$\frac{\partial P(N,t)}{\partial t} = r(N-1)P(N-1,t) - rNP(N,t) \; . \tag{B.1}$$

We consider a system having $N(t = 0) = N(0)$ elements at the beginning. Thus, the initial condition reads

$$P(N, t = 0) = \delta_{N,N(0)} \; . \tag{B.2}$$

The equation for the mean number of elements $\langle N \rangle(t) = \sum_N NP(N, t)$ is obtained via multiplying both sides of ((B.1)) by N and summing up from $N(0)$ to infinity. It yields

$$\frac{d\langle N \rangle}{dt} = r\langle N \rangle \; , \tag{B.3}$$

which gives the solution

$$\langle N \rangle(t) = N(0)\, e^{rt} \; . \tag{B.4}$$

Let $\mathcal{P}(N_1, N_2, \ldots; t)$ be the probability of having N_1 elements of size x_1, N_2 elements of size x_2, and so on, at time t. The time evolution of our system can be described by the master equation for $\mathcal{P}(N_1, N_2, \ldots; t)$ in an infinitely–dimensional space of stochastic variables N_n. A quantity of interest is the probability $p(n, t)$ that a randomly chosen element has size x_n at time t.

In the thermodynamic limit $N(0) \to \infty$, considered further on, the relative fluctuations of N_n around their mean values $\langle N_n \rangle$ are vanishingly small, and we have

$$p(n,t) = \frac{\langle N_n \rangle(t)}{\langle N \rangle(t)} \; . \tag{B.5}$$

In this case, the mean numbers of elements obey simple balance equations

$$\frac{d\langle N_n\rangle}{dt} = w(n-1)\langle N_{n-1}\rangle - w(n)\langle N_n\rangle \ : \ n \geq 2 \tag{B.6}$$

$$\frac{d\langle N_1\rangle}{dt} = r\langle N\rangle - w(1)\langle N_1\rangle \ . \tag{B.7}$$

From ((B.3)) and ((B.5))–((B.7)) we obtain

$$\frac{\partial p(n,t)}{dt} = w(n-1)p(n-1,t) - [w(n)+r]\, p(n,t) \ : \ n \geq 2 \tag{B.8}$$

$$\frac{\partial p(1,t)}{dt} = r - [w(1)+r]\, p(1,t) \ . \tag{B.9}$$

These are the basic relations, introduced already in [45].

In the following, we will consider two particular examples. For $w(n) = \lambda$, the stationary solution of ((B.8))–((B.9)) is an exponential function

$$p^{st}(n) = \frac{r}{\lambda}\left(1+\frac{r}{\lambda}\right)^{-n} = \frac{r}{\lambda}e^{-\gamma n} \quad \text{with} \quad \gamma = \ln\left(1+\frac{r}{\lambda}\right) \ . \tag{B.10}$$

If $x_n = (1+b)^{n-1}$ and $w(n) = \lambda$, then Eq. ((B.8)) for $p(n,t) \equiv p(x_n,t)$ becomes

$$\frac{\partial p(x_n,t)}{\partial t} = -(r+\lambda)\, p(x_n,t) + \lambda\, p(x_n-\delta_n,t) \tag{B.11}$$

with $\delta_n = x_n b/(1+b)$. This equation is similar to that one obtained in [44] (cf. Eq. (7) in [44]) and discussed also in [45]. The stationary solution $p^{st}(x_n)$ is a power–law

$$p^{st}(x_n) \propto x_n^{-\alpha} \tag{B.12}$$

with $\alpha = \ln(1+r/\lambda)/\ln(1+b)$.

Another example is $x_n = n$ and $w(n) = \lambda n$. One should note the similarity of this growth mechanism with the auto–catalysis in chemical reactions in presence of birth of new entrants [46–48] as well as with the mechanism of fault growth considered in [49]. In this case we obtain

$$\frac{\partial p(x_n,t)}{\partial t} = -(r+\lambda x_n)\, p(x_n,t) + \lambda(x_n-1)\, p(x_n-1,t) \ . \tag{B.13}$$

At large n or large x_n, it is expected that the probability $p(x_n,t)$ changes almost continuously with x_n, so that $p(x_n,t)$ can be approximated by a continuous function $p(x,t)$, which has the

meaning of the probability density. For large x_n, the stationary solution of ((B.13)) is a power–law

$$p^{st}(x_n) \propto x_n^{-\alpha} \qquad \text{at} \quad x_n \to \infty \tag{B.14}$$

with $\alpha = 1 + r/\lambda$.

Similarly as in models of aggregation with injection [50, 51], the size distribution is cut-off at $x_n \sim \Lambda(t)$, where the upper cut–off parameter $\Lambda(t)$ diverges at $t \to \infty$. The non–stationary solution converges to the stationary (power–law) one at $r > 0$ and $t \to \infty$ in the sense that the probability distribution becomes time–independent for $x \ll \Lambda(t)$, whereas $r = 0$ is a special case where $\lim_{t\to\infty} p(x_n, t) = 0$ holds for any fixed n. Indeed, the size of each element can only increase with time and no new elements appear if $r = 0$.

The total number of elements N is conserved at $r = 0$, and these elements evolve independently of each other. Hence, $p(n, t)$ in this case can be interpreted as the probability to have certain size x_n at time t for a system consisting of one element.

Assuming the initial condition $p(n, t = 0) = \delta_{n,1}$, the exact solution of ((B.8))–((B.9)) at $r = 0$ is

$$p(n, t) = \frac{(\lambda t)^{n-1}}{(n-1)!}\, e^{-\lambda t} \tag{B.15}$$

for $w(n) = \lambda$, and

$$p(n, t) = e^{-\lambda t} \left(1 - e^{-\lambda t}\right)^{n-1} \tag{B.16}$$

for $w(n) = \lambda n$, as it can be easily verified by a direct substitution. Inserting $n - 1 = \ln x_n / \ln(1 + b)$ in ((B.15)), we obtain the solution for the case $x_n = (1 + b)^{n-1}$ in terms of the element sizes x_n

$$p(x_n, t) = \frac{(\lambda t)^{\ln x_n / \ln(1+b)}}{\Gamma(1 + \ln x_n / \ln(1 + b))}\, e^{-\lambda t}\ . \tag{B.17}$$

Continuum description $x_n \to x$ is valid here for $b \to 0$ and large n around the distribution maximum, i. e., for $n \approx \lambda t \to \infty$. Besides, the probability density is $\propto p(x, t)/x$ in this case, since the density of points is varied as $1/x$.

The probability distribution can be obtained numerically by simulating stochastic trajectories, corresponding to the master equations ((B.8))–((B.9)). The results for $w(n) = \lambda = 1$ at four different values of r are shown and compared with the stationary distribution ((B.10)) in Fig. B.1. At $r = 0$ (top left), the probability distribution is represented by a moving maximum

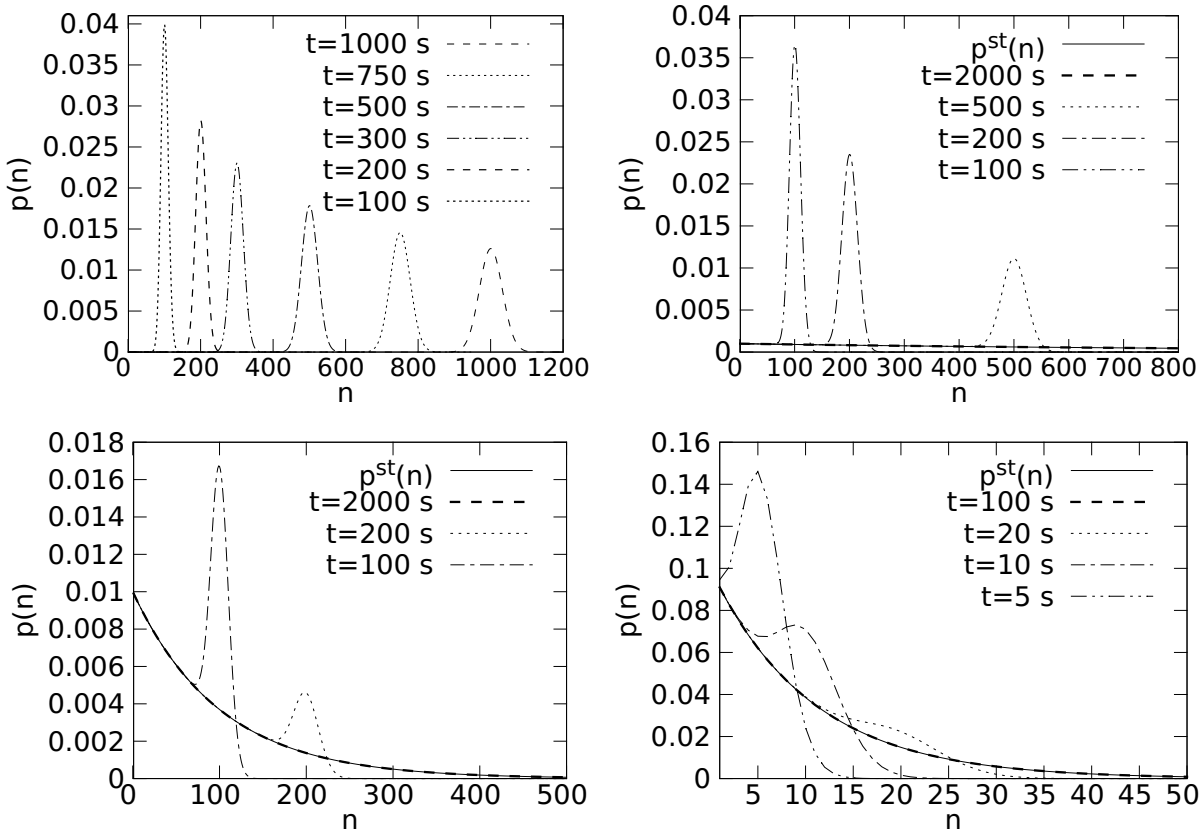

Figure B.1.: Probability distributions for $w(n) = \lambda = 1\ \mathrm{s}^{-1}$ at four different values of r (in s^{-1}): $r = 0$, $r = 0.001$, $r = 0.01$, $r = 0.1$ (r value increases form left to right and top to bottom). Dashed lines represent calculated results by solving Eqs. ((B.8))–((B.9)) numerically at different time moments t. Solid line shows stationary solution given by Eq. ((B.10)).

at $n \approx \lambda t$, as consistent with ((B.15)). This maximum is also well seen at small positive values of r ($r = 0.001; 0.01$). However, it becomes less distinct with increasing of r. Generally, the distribution is cut-off at n values, which are somewhat larger than λt. At long times, remarkably smaller than λt values of n and positive r, the time–dependent distribution is well consistent with the exponential stationary distribution ((B.10)), which is power–law distribution ((B.12)) depending on size x_n.

In the other example, where $x_n = n$ and $w(n) = \lambda n$, Eq. ((B.16)) yields the asymptotic solution at $r = 0$

$$p(x_n, t) = e^{-\lambda t} e^{-x_n/e^{\lambda t}} = \frac{1}{x_n} \frac{x_n}{e^{\lambda t}} e^{-x_n/e^{\lambda t}} \tag{B.18}$$

valid for $x_n \sim e^{\lambda t} \to \infty$. It is obtained using the identity $\lim_{z\to\infty}(1 + a/z)^z = e^a$. According to the last equality in ((B.18)), this exponential distribution is a special case of the Weibull distribution

$$p_{\text{Weibull}}(x, t) \equiv f(x; \eta, \gamma) = \frac{\gamma}{x} \left(\frac{x}{\eta}\right)^{\gamma} e^{-(x/\eta)^{\gamma}} \tag{B.19}$$

with the scale parameter $\eta = e^{\lambda t}$ and the shape parameter $\gamma = 1$. The simulation results for four positive values of r are shown in Fig. B.2. The simulation results confirm the expected

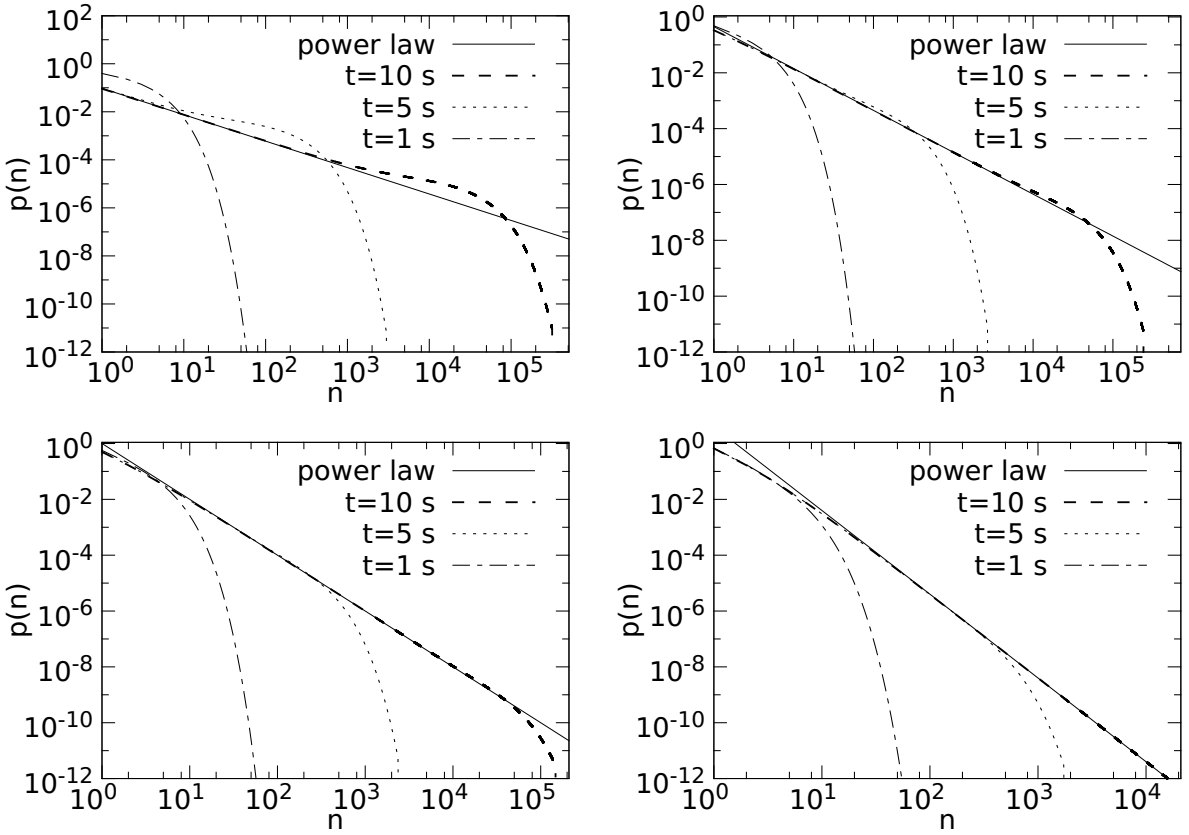

Figure B.2.: Probability distributions for $w(n) = n\,\lambda$ with $\lambda = 1$ s^{-1} at four different values of r (in s^{-1}): $r = 0.1$, $r = 0.5$, $r = 1$, $r = 2$ (r value increases form left to right, top to bottom). Dashed lines represent calculated results by solving Eq. ((B.13)) numerically at different time moments t. Solid line represents power law solution from Eq. ((B.14)), and proportionality constant was determined by fitting numerical results of Eq. ((B.13)) at large n for maximal calculated time, because power law solution should be valid at large value of n and long time t.

convergence to the stationary power–law distribution ((B.14)) for large $x_n = n$ and long times t.

The last term in ((B.13)) can be evaluated approximately by using the Taylor expansion of $y\,p(y,t)$ around $y = x$. In the linear approximation at $r = 0$, it leads to a continuous equation

$$\frac{\partial p(x,t)}{\partial t} = -\lambda\,p(x,t) - \lambda x \frac{\partial p(x,t)}{\partial x}\ , \tag{B.20}$$

with $p(x,t)$ being the probability density. This equation is valid for large x in certain cases, where the higher order expansion terms are small. It satisfies the conservation law of total probability, as it can be easily verified performing the integration over x by parts. It has a

solution

$$p(x,t) = \frac{1}{x}\,\mathcal{F}\left(\frac{x}{\eta(t)}\right) \tag{B.21}$$

with the shape function $\mathcal{F}(z)$ and the scale parameter $\eta(t) = \eta_0 e^{\lambda t}$. Here $\mathcal{F}(z)$ is an arbitrary function, which has continuous first derivative. The Weibull distribution ((B.19)) is a particular case of ((B.21)). Hence, if we choose the initial condition corresponding to ((B.21)) at $t = 0$, then this equation represents the solution also at $t > 0$. This solution has a simple interpretation: it corresponds to the growth of the size x of each element according to the deterministic approximation $dx/dt = \lambda x$. The second–order derivative neglected in ((B.20)) is responsible for the diffusion effect, which can change the shape of the distribution. Eq. ((B.20)) is a good approximation within a finite time interval for the initial distribution in the form of ((B.21)) with large η_0. In this case, the second– and higher–order derivatives, neglected in ((B.20)) are small for any $x \sim \eta_0$, i. e., the diffusion effect is small within not too long time interval. Consequently, any skew distribution of the general form ((B.21)) can be observed as a transient behavior at appropriate initial distribution of element sizes, provided that no new elements are generated, i. e., $r = 0$.

B.3. Conclusions

1. The emergence of stationary power–law distributions of element sizes, as well as of non–stationary skew distributions, such as the Weibull distribution, has been considered in certain evolving systems, where the mean total number of elements $\langle N \rangle$ grows exponentially with time t as $\langle N \rangle(t) = N(0)e^{rt}$, and the size of each element also grows with time (Sec. B.2).

2. Our exact results for the model with no particle injection ($r = 0$) show that in this special case, where the total number of elements is fixed, the non–stationary long–time solutions can be different skew distributions given by Eqs. ((B.17)) and ((B.18)). The solution ((B.18)) is a particular case of the Weibull distribution. Our analysis shows that transient distributions of a general approximate form ((B.21)) can be also observed. The analytical solutions have been compared with the results of numerical simulations of the corresponding master equations, providing also the probability distributions for the general case of $r \geq 0$. A convergence of a time–dependent solution to the stationary (power–law) one is observed for large element sizes at $r > 0$ and time $t \to \infty$.

Bibliography

[1] L. Onsager, Crystal statistics. I. A two-dimensional model with an order-disorder transition, Phys. Rev., 65 (1944), 117–149.

[2] B. McCoy and T.T. Wu, The Two–Dimensional Ising Model, Harvard University Press, 1973.

[3] R.J. Baxter, Exactly Solved Models in Statistical Mechanics, Academic Press, London, 1989.

[4] A. Pelissetto and E. Vicari, Critical phenomena and renormalization-group theory, Phys. Rep., 368 (2002), 549–727.

[5] J. Kaupužs, Critical exponents predicted by grouping of Feynman diagrams in φ^4 model, Ann. Phys. (Leipzig), 10 (2001), 299–331.

[6] D.J. Amit, Field Theory, the Renormalization Group, and Critical Phenomena, World Scientific, Singapore, 1984.

[7] S.K. Ma, Modern Theory of Critical Phenomena, W. A. Benjamin, Inc., New York, 1976.

[8] J. Zinn-Justin, Quantum Field Theory and Critical Phenomena, Clarendon Press, Oxford, 1996.

[9] H. Kleinert and V. Schulte-Frohlinde, Critical Properties of ϕ^4 Theories, World Scientific, Singapore, 2001.

[10] D. Sornette, Critical Phenomena in Natural Sciences, Springer, Berlin, 2000.

[11] R.R.P. Singh, Does quantum mechanics play role in critical phenomena?, Physics., 3 (2010), 35.

[12] I.D. Lawrie, Goldstone mode singularities in specific heats and non-ordering susceptibilities of isotropic systems, J. Phys. A: Math. Gen., 18 (1985), 1141–1152.

[13] P. Hasenfratz and H. Leutwyler, Goldstone boson related finite size effects in field theory and critical phenomena with O(N) symmetry, Nucl. Phys. B, 343 (1990), 241–284.

[14] U.C. Tuber and F. Schwabl, Critical dynamics of the O(n)-symmetric relaxational models below the transition temperature, Phys. Rev. B, 46 (1992), 3337–3361.

[15] L. Schäfer and H. Horner, Goldstone mode singularities and equation of state of an isotropic magnet, Z. Phys. B, 29 (1978), 251–263.

[16] R. Anishetty, R. Basu, N.D.H. Dass, and H.S. Sharatchandra, Infrared behaviour of systems with Goldstone bosons, Int. J. Mod. Phys. A, 14 (1999), 3467–3495.

[17] J. Kaupužs, Longitudinal and transverse correlation functions in the ϕ^4 model below and near the critical point, Progress of Theoretical Physics, 124 (2010), 613–643.

[18] J. Kaupužs, R.V.N. Melnik, and J. Rimšāns, Monte Carlo test of Goldstone mode singularity in 3D XY model, Eur. Phys. J. B, 55 (2007), 363–370.

[19] J. Kaupužs, R.V.N. Melnik, and J. Rimšāns, Advanced Monte Carlo study of the Goldstone mode singularity in the 3D XY model, Communications in Computational Physics, 4 (2008), 124–134.

[20] J. Kaupužs, R.V.N. Melnik, and J. Rimšāns, Monte Carlo estimation of transverse and longitudinal correlation functions in the $O(4)$ model, Phys. Lett. A, 374 (2010), 1943–1950.

[21] J. Schmelzer, G. Röpke, and R. Mahnke, Aggregation Phenomena in Complex Systems, Wiley–VCH, Weinheim, 1999.

[22] K. Nagel and M. Schreckenberg, A cellular automaton model for freeway traffic, J. Phys. I France, 2 (1992), 2221–2229.

[23] H. Emmerich and E. Rank, An improved cellular automaton model for traffic flow simulation, Physica A, 234 (1997), 676–686.

[24] D. Helbing and M. Schreckenberg, Cellular automata simulating experimental properties of traffic flow, Phys. Rev. E, 59 (1999), R2505–R2508.

[25] M. Fukui and Y. Ishibashi, Traffic flow in 1D cellular automaton model including cars moving with high speed, J. Phys. Soc. Japan, 65 (1996), 1868–1870.

[26] D.E. Wolf, Cellular automata for traffic simulations, Physica A, 263 (1999), 438–451.

[27] P. Simon and H.A. Gutowitz, Cellular automaton model for bidirectional traffic, Phys. Rev. E, 57 (1998), 2441–2444.

[28] T. Tokihiro, D. Takahashi, J. Matsukidaira, and J. Satsuma, From soliton equations to integrable cellular automata through a limiting procedure, Phys. Rev. Lett., 76 (1996), 3247–3250.

[29] A. Schadschneider, The Nagel–Schreckenberg model revisited, Eur. Phys. J. B, 10 (1999), 573–582.

[30] D. Chowdhury, L. Santen, and A. Schadschneider, Statistical physics of vehicular traffic and some related systems, Phys. Rep., 329 (2000), 199–329.

[31] R. Mahnke and N. Pieret, Stochastic master–equation approach to aggregation in freeway traffic, Phys. Rev. E, 56 (1997), 2666–2671.

[32] R. Mahnke, J. Kaupužs, and I. Lubashevsky, Probabilistic description of traffic flow, Phys. Rep., 408 (2005), 1–130.

[33] R. Mahnke, J. Kaupužs, and I. Lubashevsky, Physics of Stochastic Processes: How Randomness Acts in Time, Wiley–VCH, Weinheim, 2009.

[34] M.E.J. Newman, Power laws, Pareto distributions and Zipf's law, Contemp. Phys., 46 (2005), 323–351.

[35] A. Saichev, Y. Malevergne, and D. Sornette, Theory of Zipf's Law and Beyond, Springer, Berlin, 2009.

[36] A. Clauset, C.R. Shalizi, and M.E.J. Newman, Power-law distributions in empirical data, SIAM Review, 51 (2009), 661–703.

[37] S. Frank, The common patterns of nature, Journal of Evolutionary Biology, 22 (2009), 1563–1585.

[38] H. Kuninaka and M. Matsushita, Why does Zipf's law break down in rank–size distribution of cities?, J. Phys. Soc. Japan, 77 (2008), 114801.

[39] O. Moriyama, H. Itoh, S. Matsushita, and M. Matsushita, Long–tailed duration distributions for disability in aged people, J. Phys. Soc. Japan, 72 (2003), 2409–2412.

[40] T. Wada, A nonlinear drift which leads to κ–generalized distributions, Eur. Phys. J. B, 73 (2010), 287–291.

[41] U. Frisch and D. Sornette, Extreme deviations and applications, J. Phys. I France, 7 (1997), 1155–1171.

[42] Y. Malevergne and D. Sornette, Extreme Financial Risks: From Dependence to Risk Management, Springer, Berlin, 2006.

[43] Y. Malevergne, V. Pisarenko, and D. Sornette, Empirical distributions of log-returns: between the stretched exponential and the power law?, Quant. Financ., 5 (2005), 379–401.

[44] M.Y. Choi, H. Choi, J.-Y. Fortin, and J. Choi, How skew distributions emerge in evolving systems, Europhys. Lett. (EPL), 85 (2009), 30006.

[45] J. Kaupužs, R. Mahnke, and H. Weber, Comment on 'How skew distributions emerge in evolving systems' by Choi M. Y. et al., Europhys. Lett. (EPL), 46 (2010), 30004.

[46] M. Levy and S. Solomon, Power laws are logarithmic Boltzmann laws, Int. J. Mod. Phys. C, 7 (1996), 595–601.

[47] O. Malcai, O. Biham, and S. Solomon, Power-law distributions and Lévy-stable intermittent fluctuations in stochastic systems of many autocatalytic elements, Phys. Rev. E, 60 (1999), 1299–1303.

[48] A. Blank and S. Solomon, Power laws in cities population, financial markets and internet sites (scaling in systems with a variable number of components), Physica A, 287 (2000), 279–288.

[49] D. Sornette and P. Davy, Fault growth model and the universal fault length distribution, Geophys. Res. Lett., 18 (1991), 1079–1081.

[50] H. Takayasu, M. Takayasu, A. Provata, and G. Huber, Statistical properties of aggregation with injection, J. Stat. Phys., 65 (1991), 725–745.

[51] S.N. Majumdar and C. Sire, Exact dynamics of a class of aggregation models, Phys. Rev. Lett., 71 (1993), 3729–3732.